

# **Semiconductor Ring Lasers for all-optical signal processing**

Gábor Mezősi

August 2010

A thesis submitted to the University of Glasgow in accordance with the requirements for the degree of Doctor of Philosophy in the Faculty of Engineering, Department of Electronics and Electrical Engineering.

© Gábor Mezősi

## Abstract

Since the late 1980s there has been a strong interest in exploiting optical bistability for all-optical signal processing. In this scenario, a novel and promising building block is the semiconductor ring laser (SRL) that exhibits bistability between the counter-propagating cavity modes. This thesis reports on the design, fabrication and characterisation of 1550 nm lasing wavelength SRLs that are intended for applications as all-optical flip-flops and logic elements. Substantial optimisation of SRL design and processing technology is carried out in order to promote unidirectional bistable operation and allow high yield. Fabricated, large size, 150  $\mu\text{m}$ -200  $\mu\text{m}$  radius SRLs, show robust unidirectional bistable operation with 30-35 dB directional extinction ratio (DER) between the counter-propagating modes, from near threshold up to 5-6 times threshold current bias. A significant advantage of the optimised technology is that 98% of the devices per chip show continuous wave (*cw*) and room temperature lasing with an average 2-3 mA threshold current dispersion. Switch-on and switch-off times as short as 60 ps and 30 ps were measured, respectively, and reliable 10 Gbit/s flip-flop (FF) operation with external triggering optical pulses was achieved with these devices. Temporal measurements and calculations show that the switching speed of the free running SRL is limited by the carrier lifetime. A monostable device consisting of a SRL and an integrated distributed feedback laser (DFB) source is also presented, and this holding beam (HB) configuration is used to demonstrate all-optical NOT operation with data rates up to 2.5 Gbit/s. Dry etch chemistries for realizing 3.2-4.5  $\mu\text{m}$  deep waveguides, which show minimal bending losses, are developed and evaluated in order to enable dense integration of SRL devices. In addition, compact, milliwatt output power racetrack shaped cavity designs with radii as small as 10  $\mu\text{m}$  are presented. These devices exhibit minimal intra-cavity back-reflections by employing bi-level etching couplers and adiabatic straight to curved waveguide convertors. Finally, these developments provide a more than 150 times footprint reduction compared to large radius devices, whilst also preserving the robust unidirectional operation of their relatives with slightly lower, 20-30 dB DER.

# Declaration and Copyright

## Declaration

Unless otherwise acknowledged, the content of this thesis is the original and sole work of the author. No portion of this work has been submitted by the author in support of an application for any other degree or qualification, at this or any other university or institute of learning. The views expressed in this thesis are those of the author, and not necessarily those of the University of Glasgow.

Gábor Mezősi

## Copyright

Attention is drawn to the fact that the copyright of this thesis rests with the author. This copy of the thesis has been supplied on condition that anyone who consults it is understood to recognize that its copyright rests with the author and that no quotation from the thesis and no information derived from it may be published without the prior written consent of the author.

# Contents

<b>1</b>	<b>Introduction</b>	<b>1</b>
1.1	Motivation . . . . .	1
1.2	Current state of the art of all-optical bistables . . . . .	1
1.3	Basic operating principles of semiconductor ring lasers . . . . .	3
1.4	Review of the major contributions to SRL research . . . . .	6
1.5	Objectives of this thesis and organisation of the chapters . . . . .	8
<b>2</b>	<b>Fabrication</b>	<b>11</b>
2.1	Overview of the process flow . . . . .	11
2.2	Sample preparation . . . . .	13
2.3	Lithography . . . . .	13
2.3.1	HSQ resist . . . . .	14
2.3.2	PMMA resist . . . . .	17
2.3.3	Proximity correction . . . . .	17
2.4	Dry etching . . . . .	22
2.4.1	Shallow etch . . . . .	23
2.4.2	Deep etch . . . . .	26
2.5	Dielectric quasi-planarisation and metallisation . . . . .	30
2.6	Chapter summary . . . . .	33
<b>3</b>	<b>Material properties</b>	<b>35</b>
3.1	Material design . . . . .	35
3.2	Threshold current analysis . . . . .	39
3.3	Chapter summary . . . . .	42

<b>4</b>	<b>Shallow etched device design</b>	<b>43</b>
4.1	Waveguide design . . . . .	43
4.2	“Semi-shallow” waveguides . . . . .	46
4.3	Coupler design . . . . .	48
4.4	Facet back-reflection . . . . .	54
4.5	Overview of shallow etched ring laser characteristics . . . . .	58
4.6	Chapter summary . . . . .	63
<b>5</b>	<b>Deep etched design</b>	<b>65</b>
5.1	Waveguide design . . . . .	65
5.2	Non-radiative losses . . . . .	67
5.3	Bending losses . . . . .	71
5.4	Micro-ring and micro-disk lasers . . . . .	76
5.4.1	Junction heating in small SRL devices . . . . .	78
5.4.2	RIE-lag effects in small SRL devices . . . . .	81
5.5	Coupler design . . . . .	82
5.6	Adiabatic, low reflection transitions . . . . .	88
5.7	Racetrack shape micro ring lasers . . . . .	92
5.8	Chapter summary . . . . .	95
<b>6</b>	<b>Dynamic device characterization</b>	<b>98</b>
6.1	SRL bistable characteristics – memory . . . . .	98
6.2	SRL monostable charactersitics – logic gates . . . . .	106
6.3	Chapter summary . . . . .	112
<b>7</b>	<b>Conclusions and future work</b>	<b>114</b>
7.1	Conclusions . . . . .	114
7.2	Future Work . . . . .	117

# List of Figures

1.1	Schematic illustration of a bistable SRL. . . . .	4
1.2	Schematic illustration of all-optical logic gates that are based on a SRL monostable. . . . .	5
(a)	Schematic of a NOT gate and its principle of operation. . . . .	5
(b)	Schematic of an all-optical thresholder and its principle of operation. . . . .	5
2.1	Simplified process flow of the fabrication steps. . . . .	12
2.2	Schematic of the resist exposure. . . . .	14
(a)	Negative tone resist. . . . .	14
(b)	Positive tone resist. . . . .	14
2.3	SEM images of exposed and developed HSQ patterns. . . . .	15
(a)	Close up of the resist sidewall. . . . .	15
(b)	Gear like test pattern. . . . .	15
2.4	Measured contrast curves of the HSQ resist. . . . .	16
2.6	Simulated trajectories of 100 keV electrons through InP. . . . .	19
2.7	Simulated electron distribution functions. . . . .	19
(a)	Distribution of the energy deposited by electrons as a function of the radius. . . . .	19
(b)	Plot of $\int r * f(r)$ as a function of the radial distance from the incidence point. . . . .	19
2.8	Iso-dose maps of fractured and proximity corrected patterns . . . . .	21
(a)	40 $\mu\text{m}$ square. . . . .	21
(b)	16 $\mu\text{m}$ radius and 3 $\mu\text{m}$ wide ring resonator. . . . .	21
2.9	Schematic of waveguide cross section types. . . . .	22
(a)	Shallow etched waveguide. . . . .	22

(b)	Deep etched waveguide. . . . .	22
2.10	SEM photograph of a shallow etched evanescent point coupler. . . . .	24
2.11	Measured etch data of the $\text{CH}_4/\text{H}_2/\text{O}_2$ chemistry. . . . .	25
(a)	Etch rate as a function of the etched area size. . . . .	25
(b)	Etch rate in gaps versus the gap width. . . . .	25
2.13	SEM image of an evanescent point coupler that was etched with the $\text{Cl}_2/\text{CH}_4/\text{H}_2$ chemistry. . . . .	27
2.14	SEM image of a double micro ring structure that was etched with the $\text{Cl}_2/\text{Ar}/\text{N}_2$ chemistry. . . . .	28
2.15	Measured RIE lag data of deep etched waveguides. . . . .	30
(a)	$\text{Cl}_2/\text{Ar}/\text{N}_2$ chemistry . . . . .	30
(b)	$\text{Cl}_2/\text{Ar}/\text{BCl}_3$ chemistry . . . . .	30
2.16	SEM image of a $5\ \mu\text{m}$ radius micro disk. . . . .	31
2.17	SEM image of a $2\ \mu\text{m}$ deep etched waveguide's facet. . . . .	32
(a)	Without quasi-planarisation. . . . .	32
(b)	With quasi-planarisation. . . . .	32
3.1	Layout design of different length half ring lasers. . . . .	38
3.2	Calculated modal gain characteristics of the IEGENS-13-17 material. . . . .	39
(a)	Modal gain versus current density. . . . .	39
(b)	Current density over modal gain versus the modal gain. . . . .	39
3.3	Schematic of a racetrack shape semiconductor ring laser. . . . .	40
3.4	Calculated threshold current as a function of the ring radius. . . . .	41
4.1	Simulated shallow etched waveguide properties. . . . .	44
(a)	Contour map of the $\text{TE}_{00}$ mode. . . . .	44
(b)	Simulated modal effective index versus the waveguide width. . . . .	44
4.2	Simulated bending losses as a function of the bend radius. . . . .	45
4.3	Calculated and measured properties of the "semi-shallow" waveguides. . . . .	47
(a)	Simulated bending losses as a function of the etch depth. . . . .	47
(b)	$J_{th}$ and $r_a$ as a function of the radius of half ring lasers. . . . .	47
(c)	Schematic of the core cross section. . . . .	47
4.4	Schematic of the Y-junction, MMI and directional coupler . . . . .	48
4.6	Simulated beating length of a directional coupler as a function of the distance from the core top with the gap separation as a parameter. . . . .	52

4.7	Measured splitting ratio as a function of the propagation distance of a 800 nm gap evanescent field coupler. . . . .	53
4.8	Layout of a one side tilted FP lasers. . . . .	55
4.9	Measured slope efficiency of the tilted output (blue dots) and facet reflectivity (black squares) as a function of the mirror angle of a 2 $\mu\text{m}$ wide waveguide FP laser. . . . .	56
4.10	Layout of the tilted and tapered FP lasers. . . . .	56
4.11	Measured relative reflectivity change of tilted waveguides as a function of their tapering width. . . . .	57
4.12	Optical micrograph of a a 150 $\mu\text{m}$ radius racetrack SRL. . . . .	59
4.13	Measured P–I characteristic of a 150 $\mu\text{m}$ radius and 50% coupler SRL. . . . .	60
4.14	Device performance statistics. . . . .	60
	(a) Threshold current density statistics. . . . .	60
	(b) Histogram of the series resistance distribution. . . . .	60
4.15	Measured optical spectra of a 150 $\mu\text{m}$ radius and 50% coupler SRL for the $I_{SRL}$ of 200 mA. . . . .	61
	(a) CW direction. . . . .	61
	(b) CCW direction. . . . .	61
4.16	Measured CCW direction spectral map of the device whose P–I curve is reported in Fig 4.13. . . . .	62
5.1	Simulated deeply etched waveguide properties. . . . .	66
	(a) Contour map of the $\text{TE}_{00}$ mode. . . . .	66
	(b) Simulated modal effective index versus the waveguide width. . . . .	66
5.2	Measured threshold current density of FP lasers as a function of the waveguide width. . . . .	67
5.3	Non-radiative recombination processes. . . . .	68
	(a) Defect and impurity recombination. . . . .	68
	(b) Auger recombination. . . . .	68
	(c) Surface recombination. . . . .	68
5.4	Schematic of the transmission loss measurement setup. . . . .	69
5.5	Measured transmission loss and calculated relative efficiency as a function of the waveguide width. . . . .	70

5.6	Simulated bending losses of a deeply etched waveguide as a function the bend radius, with the etch depth as a parameter. . . . .	71
5.7	Measured threshold current density and area specific resistance of half ring lasers as function of the radius. . . . .	72
5.8	Simulated bending losses as a function of the width of a deep etched waveguide, with the radius as a parameter. . . . .	74
5.9	Measured threshold current density and area specific resistance of 20 $\mu\text{m}$ radius half ring lasers as function of the waveguide width. . .	75
5.10	Schematic of fabricated ring and disk shape ring laser devices. . . .	77
5.11	SEM photograph of a 7 $\mu\text{m}$ radius SDL. The inset shows a close up of a 6 $\mu\text{m}$ diameter micro-disk. . . . .	77
5.12	Measured threshold current density of micro-SRLs and SDLs as a function of the device radius. . . . .	78
5.13	Measured and calculated series resistance of micro-SRLs and SDLs as a function of the device radius. . . . .	79
5.14	Measured and simulated thermal SRL properties. . . . .	80
	(a) P–I curve of a 10 $\mu\text{m}$ radius SRL recorded at 20° and 0°. . . .	80
	(b) Isothermal map of a 10 $\mu\text{m}$ radius SRL. . . . .	80
5.15	Deep etched MMI coupler. . . . .	83
	(a) 3 dB coupling length as a function of the width of the MMI. . .	83
	(b) Schematic of a general-interference MMI coupler. . . . .	83
5.16	Schematic of a parabolically tapered MMI coupler. . . . .	84
5.17	Cross section of a deep etched directional coupler. . . . .	84
	(a) Idealistic structure. . . . .	84
	(b) Realistic structure. . . . .	84
5.18	Simulated beating length of an “ideal” deep etched evanescent coupler as a function of the separation distance with the waveguide width as a parameter. . . . .	85
5.19	Power distribution as a function of the propagation distance for various gap etch depths. The waveguide parameters $g$ and $d$ were set to 400 nm and to 3.26 $\mu$ , respectively. . . . .	86
	(a) Gap depth of 1.02 $\mu\text{m}$ . . . . .	86
	(b) Gap depth of 1.62 $\mu\text{m}$ . . . . .	86
	(c) Gap depth of 1.82 $\mu\text{m}$ . . . . .	86

(d)	Gap depth of $1.92\ \mu\text{m}$ . . . . .	86
(e)	Gap depth of $2.02\ \mu\text{m}$ . . . . .	86
(f)	Gap depth of $2.27\ \mu\text{m}$ . . . . .	86
5.20	Calculated differential efficiency as a function of the out-coupled power. . . . .	88
5.21	Offset straight to curved transitions. . . . .	89
(a)	Schematic of the transition. . . . .	89
(b)	Calculated offset values, where the power transfer is maximal, as a function of the waveguide radius. . . . .	89
5.22	Adiabatic straight to curved transition. . . . .	90
(a)	Calculated curvature of an adiabatic transition segment as a function of the angular length. . . . .	90
(b)	Schematic of a $10\ \mu\text{m}$ radius adiabatic and conventional bend. . . . .	90
5.23	Schematic of a cosine shape S-bend and that of a conventional S-bend. . . . .	91
5.24	Schematic of racetrack shape SRL devices. . . . .	92
5.25	SEM photograph of racetrack-shape $10\ \mu\text{m}$ radius SRLs. . . . .	93
5.26	Recorded P–I characteristics of a $10\ \mu\text{m}$ radius racetrack SRLs with coupling lengths of 5 and $10\ \mu\text{m}$ . . . . .	94
5.27	Recorded CW and CCW optical spectra of a $10\ \mu\text{m}$ radius racetrack SRL with an $L_c$ of $10\ \mu\text{m}$ . . . . .	95
6.1	General experimental setup for measuring the dynamic properties of SRL. . . . .	99
6.2	Experimental SRL time traces. . . . .	100
(a)	Response to two subsequent set and reset pulses. . . . .	100
(b)	Typical switch on transition. . . . .	100
(c)	Typical switch off transition. . . . .	100
(a)	Measured optical spectrum of the OPO pulses. . . . .	101
(b)	Measured optical spectrum of the SRL device under injection of 5 ps pulses. . . . .	101
6.4	Measured switch-on time delay as a function of the SRL bias current. . . . .	102
6.6	Time trace of the response of a SRL device to 50 ps switching pulses. . . . .	105
6.7	Alternative SRL design for eliminating asymmetric mark to space ratios, caused by the switching pulses. . . . .	106

6.8	Optical micrograph of a fabricated SRL with integrated DFB laser.	107
6.9	Measured output characteristics of the integrated DFB SRL device.	109
	(a) P–I characteristics for an $I_{DFB}$ of 0 mA and 55 mA. . . . .	109
	(b) Measured CCW direction spectral map for $I_{DFB}=0$ mA. . . . .	109
	(c) Measured CCW direction spectral map for $I_{DFB}=55$ mA. . . . .	109
6.11	Measured time traces of the injected 2 Gbit/s 101100111000 bit sequence (top) and the SRL response (bottom). . . . .	111
6.12	Measured $2^7-1$ PRBS eye diagram of the integrated NOT gate for a data rate of 2 Gbit/s. . . . .	112
7.1	Wavelength tunable coupled double SRL. . . . .	119
	(a) Optical micrograph of the device. . . . .	119
	(b) Example tuning characteristics. . . . .	119

# List of Tables

1.1	Comparison of the state of the art of competing all-optical signal processing technologies. . . . .	3
2.1	Summary of deep etch process parameters. . . . .	27
3.1	Epitaxial layer structure of the IEGENS-13-17 material. . . . .	36
3.2	Measured material parameters of the IEGENS-13-17 wafer. . . . .	39
3.3	Values substituted into Eq. 3.6 to calculate the threshold current as a function of ring radius with out-coupling as a parameter. . . . .	40
4.1	Summary of the properties of the three different coupler types. . . . .	49
4.2	Measured power coupling of point couplers. . . . .	53

# Main publications

1. G. Mezosi, M. Strain, S. Furst, Z. Wang, S. Yu, and M. Sorel, “Unidirectional bistability in AlGaInAs microring and microdisk semiconductor lasers,” *Photonics Technology Letters, IEEE* **21**, pp. 88 –90, jan.15, 2009.
2. M. J. Strain, G. Mezósi, J. Javaloyes, M. Sorel, A. Pérez-Serrano, A. Scirè, S. Balle, J. Danckaert, and G. Verschaffelt, “Semiconductor snail lasers,” *Applied Physics Letters* **96**(12), p. 121105, 2010.
3. G. Mezosi, S. Furst, and M. Sorel, “Active Q-switching in semiconductor ring lasers,” in *Lasers and Electro-Optics, 2008 and 2008 Conference on Quantum Electronics and Laser Science. CLEO/QELS 2008. Conference on*, 2008.
4. G. Mezosi, S. Furst, M. Strain, Z. Wang, S. Yu, and M. Sorel, “Directional bi-stability in micro-ring and micro-disk lasers,” in *Semiconductor Laser Conference, 2008. ISLC 2008. IEEE 21st International*, 2008.
5. M. Sorel, G. Mezósi, and M. J. Strain, “Semiconductor micro-ring and micro-disk lasers for all-optical switching,” *Novel In-Plane Semiconductor Lasers VIII* **7230**(1), p. 72300I, SPIE, 2009.

## Other journal publications

1. Z. Wang, G. Verschaffelt, Y. Shu, G. Mezosi, M. Sorel, J. Danckaert, and S. Yu, “Integrated small-sized semiconductor ring laser with novel retro-reflector cavity,” *Photonics Technology Letters, IEEE* **20**, pp. 99 –101, jan.15, 2008.
2. B. Li, M. Memon, G. Mezosi, G. Yuan, Z. Wang, M. Sorel, and S. Yu, “All-optical response of semiconductor ring laser to dual-optical injections,” *Photonics Technology Letters, IEEE* **20**, pp. 770 –772, may15, 2008.
3. S. Beri, L. Gelens, M. Mestre, G. Van der Sande, G. Verschaffelt, A. Scirè, G. Mezosi, M. Sorel, and J. Danckaert, “Topological insight into the non-arrhenius mode hopping of semiconductor ring lasers,” *Phys. Rev. Lett.* **101**, p. 093903, Aug 2008.
4. D. Lu, G. Mezosi, B. Li, M. Memon, Z. Wang, M. Sorel, S. Jian, and S. Yu, “Configurable all-optical multicast using cavity-enhanced four wave mixing in semiconductor ring laser,” *Electronics Letters* **44**, pp. 1374 –1376, november 2008.
5. K. Thakulsukanant, B. Li, I. Memon, G. Mezosi, Z. Wang, M. Sorel, and S. Yu, “All-optical label swapping using bistable semiconductor ring laser in an optical switching node,” *Lightwave Technology, Journal of* **27**, pp. 631 –638, march15, 2009.
6. L. Gelens, S. Beri, G. Van der Sande, G. Mezosi, M. Sorel, J. Danckaert, and G. Verschaffelt, “Exploring multistability in semiconductor ring lasers: Theory and experiment,” *Phys. Rev. Lett.* **102**, p. 193904, May 2009.

7. M. Memon, G. Mezosi, B. Li, D. Lu, Z. Wang, M. Sorel, and S. Yu, "Generation and modulation of tunable mm-wave optical signals using semiconductor ring laser," *Photonics Technology Letters, IEEE* **21**, pp. 733 –735, june1, 2009.
8. B. Li, D. Lu, M. Memon, G. Mezosi, Z. Wang, M. Sorel, and S. Yu, "All-optical digital logic AND and XOR gates using four-wave-mixing in monolithically integrated semiconductor ring lasers," *Electronics Letters* **45**, pp. 698 –700, june 2009.
9. B. Li, M. Memon, G. Mezosi, Z. Wang, M. Sorel, and S. Yu, "Characterization of all-optical regeneration potentials of a bistable semiconductor ring laser," *Lightwave Technology, Journal of* **27**, pp. 4233 –4240, oct.1, 2009.
10. M. Memon, B. Li, G. Mezosi, Z. Wang, M. Sorel, and S. Yu, "Modulation bandwidth enhancement in optical injection-locked semiconductor ring laser," *Photonics Technology Letters, IEEE* **21**, pp. 1792 –1794, dec.15, 2009.

## Other conference publications

1. Z. Wang, G. Verschaffelt, G. Mezosi, M. Sorel, J. Danckaert, and S. Yu, “A novel semiconductor ring laser device aimed for all-optical signal processing,” in *Optical Fiber communication/National Fiber Optic Engineers Conference, 2008. OFC/NFOEC 2008. Conference on*, 2008.
2. G. Verschaffelt, Z. Wang, Y. Shu, G. Mezosi, J. Danckaert, M. Sorel, and S. Yu, “High-speed integrated semiconductor micro-ring lasers with efficient off-axis parabolic reflectors,” *Semiconductor Lasers and Laser Dynamics III* **6997**(1), p. 699716, SPIE, 2008.
3. M. J. L. Vidal, S. Furst, G. Mezosi, M. Zanola, M. Sorel, A. Perez, A. Scirè, S. Balle, and G. Giuliani, “Experimental analysis of the optical spectra of directionally bistable semiconductor ring lasers,” *Semiconductor Lasers and Laser Dynamics III* **6997**(1), p. 699725, SPIE, 2008.
4. A. Trita, S. Furst, G. Mezosi, M. Sorel, M. J. L. Vidal, J. Yu, F. Bragheri, I. Cristiani, and G. Giuliani, “Time-domain response to ps optical pulse trigger of an all-optical flip-flop based on semiconductor ring laser,” *Semiconductor Lasers and Laser Dynamics III* **6997**(1), p. 699724, SPIE, 2008.
5. B. Li, M. Irfan Memon, G. Yuan, Z. Wang, S. Yu, G. Mezosi, and M. Sorel, “All-optical response of semiconductor ring laser bistable to duo optical injections,” in *Lasers and Electro-Optics, 2008 and 2008 Conference on Quantum Electronics and Laser Science. CLEO/QELS 2008. Conference on*, 2008.
6. S. Furst, G. Mezosi, S. Yu, and M. Sorel, “Monolithic integration of semiconductor ring lasers with distributed bragg gratings,” in *Lasers and Electro-*

*Optics, 2008 and 2008 Conference on Quantum Electronics and Laser Science. CLEO/QELS 2008. Conference on, 2008.*

7. A. Trita, G. Mezosi, F. Bragheri, J. Yu, S. Furst, I. Cristiani, W. Elsasser, M. Sorel, and G. Giuliani, "Switching time and response to ps optical trigger pulse of all-optical flip-flop based on a monolithic semiconductor ring laser," in *Semiconductor Laser Conference, 2008. ISLC 2008. IEEE 21st International, 2008.*
8. M. Zanola, G. Mezosi, S. Furst, M. Sorel, and G. Giuliani, "Dynamic characterization of semiconductor ring lasers: Frequency response and linewidth enhancement factor," in *Semiconductor Laser Conference, 2008. ISLC 2008. IEEE 21st International, 2008.*
9. A. Trita, G. Mezosi, F. Bragheri, J. Yu, S. Furst, W. Elsasser, I. Cristiani, M. Sorel, and G. Giuliani, "Dynamic operation of all-optical flip-flop based on a monolithic semiconductor ring laser," in *Optical Communication, 2008. ECOC 2008. 34th European Conference on, 2008.*
10. B. Li, G. Mezosi, M. I. Memon, Z. Wang, M. Sorel, and S. Yu, "All-optical nrz to rz format conversion using bistable semiconductor ring laser," *Optical Transmission, Switching, and Subsystems VI* **7136**(1), p. 71362X, SPIE, 2008.
11. D. Lu, G. Mezosi, B. Li, M. Memon, Z. Wang, M. Sorel, S. Jian, and S. Yu, "All-optical multicast based on cavity-enhanced four-wave-mixing in semiconductor ring laser," in *Optical Fiber Communication - includes post deadline papers, 2009. OFC 2009. Conference on, 2009.*
12. M. Zanola, G. Mezosi, M. Vidal, A. Trita, M. Sorel, and G. Giuliani, "Error-free operation of monolithic all-optical set-reset flip-flop based on semiconductor ring laser," in *Lasers and Electro-Optics, 2009 and 2009 Conference on Quantum electronics and Laser Science Conference. CLEO/QELS 2009. Conference on, 2009.*
13. M. Strain, A. Perez-Serrano, G. Mezosi, G. Verschaffelt, A. Scire, J. Danckaert, M. Sorel, and S. Balle, "Semiconductor snail laser," in *Lasers and Electro-Optics 2009 and the European Quantum Electronics Conference. CLEO Europe - EQEC 2009. European Conference on, 2009.*

14. B. Li, M. Memon, G. Mezosi, Z. Wang, M. Sorel, and S. Yu, "All-optical digital logic XOR gate using bistable semiconductor ring lasers," in *Lasers and Electro-Optics 2009 and the European Quantum Electronics Conference. CLEO Europe - EQEC 2009. European Conference on*, 2009.
15. S. Beri, L. Gelens, G. Van der Sande, G. Verschaffelt, G. Mezosi, M. Sorel, and J. Danckaert, "Directional mode hopping in semiconductor ring lasers," in *Lasers and Electro-Optics 2009 and the European Quantum Electronics Conference. CLEO Europe - EQEC 2009. European Conference on*, 2009.
16. J. Javaloyes, A. Trita, G. Mezosi, F. Bragheri, I. Cristiani, G. Giuliani, M. Sorel, A. Scire, and S. Balle, "Ultrafast all-optical switching of bistable semiconductor ring lasers," in *Lasers and Electro-Optics 2009 and the European Quantum Electronics Conference. CLEO Europe - EQEC 2009. European Conference on*, 2009.
17. M. Vidal, M. Zanola, G. Mezosi, A. Trita, M. Sorel, and G. Giuliani, "Bit-error-rate measurement for an all-optical set-reset flip-flop based on semiconductor ring laser," in *Lasers and Electro-Optics 2009 and the European Quantum Electronics Conference. CLEO Europe - EQEC 2009. European Conference on*, 2009.
18. M. Memon, B. Li, G. Mezosi, Z. Wang, M. Sorel, and S. Yu, "Bandwidth enhancement using master laser modulation and optical injection locking in the semiconductor ring laser," in *Lasers and Electro-Optics 2009 and the European Quantum Electronics Conference. CLEO Europe - EQEC 2009. European Conference on*, 2009.
19. M. Memon, B. Li, G. Mezosi, Z. Wang, M. Sorel, and S. Yu, "Converting 4 Gb/s IM data onto tunable 60 GHz RF optical carrier using four wave-mixing in semiconductor ring laser," in *Lasers and Electro-Optics 2009 and the European Quantum Electronics Conference. CLEO Europe - EQEC 2009. European Conference on*, 2009.
20. B. Li, M. Memon, G. Mezosi, Z. Wang, M. Sorel, and S. Yu, "All-optical signal regeneration using a bistable semiconductor ring laser," in *Lasers and Electro-*

*Optics 2009 and the European Quantum Electronics Conference. CLEO Europe - EQEC 2009. European Conference on, 2009.*

21. J. Javaloyes, G. Mezosi, M. Sorel, and S. Balle, "Emission directionality of semiconductor ring lasers," in *Lasers and Electro-Optics 2009 and the European Quantum Electronics Conference. CLEO Europe - EQEC 2009. European Conference on, 2009.*
22. B. Li, M. I. Memon, Z. Wang, S. Yu, G. Mezosi, and M. Sorel, "Optical static random access memory cell using an integrated semiconductor ring laser," in *Communications and Photonics Conference and Exhibition (ACP), 2009 Asia, 2009.*
23. B. Li, M. Memon, D. Lu, G. Mezosi, Z. Wang, M. Sorel, and S. Yu, "Cavity-enhanced four-wave-mixing in an integrated semiconductor ring laser for all-optical digital logic operations," in *Photonics in Switching, 2009. PS '09. International Conference on, 2009.*
24. B. Li, M. Memon, G. Mezosi, Z. Wang, M. Sorel, and S. Yu, "Optical static random access memory cell using an integrated semiconductor ring laser," in *Photonics in Switching, 2009. PS '09. International Conference on, 2009.*
25. A. Trita, M. Latorre Vidal, M. Zanola, G. Mezosi, J. Javaloyes, M. Sorel, F. Bragheri, I. Cristiani, A. Scire, S. Balle, and G. Giuliani, "All-optical set-reset flip-flop based on semiconductor ring laser: Ultrafast response and error-free bit-error-rate operation," in *Photonics in Switching, 2009. PS '09. International Conference on, 2009.*
26. M. Memon, B. Li, G. Mezosi, Z. Wang, M. Sorel, and S. Yu, "Frequency response enhancement in optical injection locked semiconductor ring laser using master laser modulation," in *Optical Communication, 2009. ECOC '09. 35th European Conference on, 2009.*
27. B. Li, M. I. Memon, D. Lu, G. Mezosi, Z. Wang, M. Sorel, and S. Yu, "Cavity-enhanced four-wave-mixing in an integrated semiconductor ring laser for all-optical logic operations," in *Communications and Photonics Conference and Exhibition (ACP), 2009 Asia, 2009.*

28. A. Trita, G. Mezosi, M. J. L. Vidal, M. Zanola, I. Cristiani, M. Sorel, P. Ghelfi, A. Bogoni, and G. Giuliani, “10 Gb/s operation of monolithic all-optical set-reset flip-flop based on semiconductor ring laser,” in *Lasers and Electro-Optics (CLEO) and Quantum Electronics and Laser Science Conference (QELS), 2010 Conference on*, 2010.
29. L. Mashal, S. Beri, L. Gelens, G. V. der Sande, G. Mezosi, M. Sorel, J. Danckaert, and G. Verschaffelt, “Study of excitability in semiconductor ring lasers: theory and experiment,” *Semiconductor Lasers and Laser Dynamics IV* **7720**(1), p. 772028, SPIE, 2010.
30. S. Beri, L. Gelens, M. Mestre, G. V. der Sande, G. Mezosi, M. Sorel, G. Verschaffelt, and J. Danckaert, “Theoretical and experimental investigation of mode-hopping in semiconductor ring lasers,” *Semiconductor Lasers and Laser Dynamics IV* **7720**(1), p. 772000, SPIE, 2010.

*To my family.*

# List of acronyms

<b>AR</b> antireflection	<b>FF</b> flip-flop
<b>AWG</b> arrayed waveguide grating	<b>FP</b> Fabry-Pérot
<b>BAL</b> broad area laser	<b>FDTD</b> finite difference time domain
<b>BLD</b> bistable laser diode	<b>FSR</b> free spectral range
<b>BPM</b> beam propagation method	<b>FWHM</b> full width half maximum
<b>BSS</b> beam step size	<b>FWM</b> four-wave mixing
<b>CW</b> clockwise	<b>HB</b> holding beam
<b>CCW</b> counter clockwise	<b>HSQ</b> hydrogen silsesquioxane
<b>cw</b> continuous wave	<b>ICP</b> inductively coupled plasma
<b>DC</b> direct current	<b>IPA</b> isopropyl alcohol
<b>DER</b> directional extinction ratio	<b>JWNC</b> James Watt Nanofabrication Centre
<b>DFB</b> distributed feedback laser	<b>MMI</b> multimode interference
<b>EDFA</b> erbium doped fiber amplifier	<b>MQW</b> multiple quantum well
<b>e-beam</b> electron-beam	<b>MZ</b> Mach-Zehnder
<b>eV</b> electron volt	<b>OPO</b> optical parametric oscillator
<b>FEM</b> finite element method	

<b>PECVD</b> plasma enhanced chemical vapor deposition	<b>SDL</b> semiconductor disk laser
<b>PIC</b> photonic integrated circuit	<b>SMSR</b> side mode suppression ratio
<b>PM</b> polarisation maintaining	<b>SOI</b> silicon on insulator
<b>PMMA</b> polymethyl methacrylate	<b>TE</b> transverse electric
<b>PRBS</b> pseudo random bit sequence	<b>TEC</b> thermoelectric cooler
<b>QW</b> quantum well	<b>TIR</b> total internal reflection
<b>RIE</b> reactive ion etching	<b>TLM</b> transfer length method
<b>RO-water</b> reverse osmosis water	<b>TM</b> transverse magnetic
<b>SEM</b> scanning electron microscope	<b>XGM</b> cross gain modulation
<b>SOA</b> semiconductor optical amplifier	<b>XPM</b> cross phase modulation
<b>SRFF</b> Set Reset flip-flop	<b>VCSEL</b> vertical cavity surface emitting laser
<b>SRL</b> semiconductor ring laser	

# Chapter 1

## Introduction

### 1.1 Motivation

In the past two decades there has been a continually increasing interest in all-optical digital signal processing technology and all-optical logic functions, application concepts, and demonstrations utilizing various nonlinear optical devices. The main driving force behind this research is the desire to replace optical-electronic-optical conversion stages and to utilize more efficiently the extremely large capacity of optical fibers. With the maturation of the III-V processing technology, the complexity and density of the all-optical photonic integrated circuits (PICs) increases and monolithic integrated elements counting as many as 200-300 per chip can be achieved today [1,2]. However, there is still a strong demand for all-optical processing elements and approaches that could allow higher operation speeds or more dense integration. In particular, fast and compact all-optical flip-flops (FFs) that could perform optical binary logic or form the basis for optical memories are still required.

### 1.2 Current state of the art of all-optical bistables

Semiconductor optical amplifiers SOA are very promising candidates for all-optical gating and signal processing [3]. Thanks to the ultra fast gain recovery of a com-

binned semiconductor optical amplifier (SOA) and a optical band pass filter [4, 5] the switching speed of the SOA based signal processing is superior to other approaches. So far several ultra high speed all-optical functionalities have been demonstrated with these devices, such as: 640 Gbit/s to 40 Gbit/s demultiplexing [6], 40 GHz clock recovery from 640 Gbit/s optical time division multiplexed signal [7], 320 Gbit/s wavelength conversion [8]. Also all-optical flip-flops and logic has been demonstrated in the form of several various configurations that combine SOAs with a Mach-Zehnder (MZ) interferometer [9], double fiber loops [10, 11] or polarization splitters [12] with SOAs. Compact monolithic integration and cascading of these demonstrators is very hard or impossible to realize as most of them require the implementation of integrated band pass filters, polarization splitters and optical isolators<sup>1</sup>.

Since the late 1980s there has been an increased interest in exploiting optical bistability for building all-optical flip-flops or memory cells. The first reported device showing two stable optical states was the bistable laser diode (BLD) [13], with a switching time as fast as 19 ps and an injected switching energy of 30 fJ in a three section BLD [14]. Although the device was turned off with electrical impulses, this paper demonstrated the high speed operation capability of all-optical bistable devices. More recently, multimode interference (MMI) and MZ interferometer integrated BLDs were demonstrated with 338 ps and 68 ps switching time, respectively [15, 16]. These devices show promising switching time but they lack the potential for size reduction and due to carrier recovery their switch-on time is considerably slower than the switch-off. A second configuration for realizing bistable lasers is to employ the bistability between the polarization states of a rectangular shape vertical cavity surface emitting lasers (VCSELs) [17]. 10 Gbit/s flip-flop operation has been demonstrated this way with switching pulse energies as low as 2 fJ. Also logical functionalities have been demonstrated with polarization bistable VCSELs, such as RZ-NRZ conversion [18] and 4 bit buffers [19]. Despite their very compact size ( $\sim 5 \times 5 \mu\text{m}$ ), which would allow dense integration, it is problematic to cascade these devices as their direction of emission is vertical.

More recently, semiconductor ring laser (SRL) emerged as very promising candidates for the demonstration of optical bistables [20, 21]. In fact, in these devices bistability occurs between two counter-propagating cavity modes that can be

---

<sup>1</sup>The holy grail of integrated optics.

**Table 1.1:** Comparison of the state of the art of competing all-optical signal processing technologies.

	SOA [6]	VCSEL <sup>a</sup> [17]	BLD [14, 15]	SRL [22]
Maximum bit rate	640 Gbit/s	10 Gbit/s	–	10 Gbit/s
Best switching time	< 1 ps	~ 10 ps	19 ps	50 - 60 ps
Device area	> 1000 $\mu\text{m}^2$	~ 36 $\mu\text{m}^2$	> 1000 $\mu\text{m}^2$	~ 56 $\mu\text{m}^2$
Switching pulse E	~ 9 fJ	2 fJ	30 fJ	1.8 fJ
Avg. sw. pulse power	6.3 mW	40 $\mu\text{W}$	–	18 $\mu\text{W}$
DC power consumption	0.5 - 1 W	5 - 10 mW	60 - 70 mW	~ 6 mW

<sup>a</sup>Bistable in polarisation.

switched by external optical trigger pulses.

Table 1.1 compares properties, such as maximum bit rate, cost, power consumption etc., of the all-optical signal processing devices. This table highlights clearly that in terms of speed SOAs are superior to other technologies. Despite their (currently) lower speed monolithic integrated devices, such as VCSELs or SRLs, pose a good alternative to SOAs as they offer greatly reduced power consumption and footprint.

### 1.3 Basic operating principles of semiconductor ring lasers

Unlike conventional Fabry-Pérot (FP) and distributed feedback laser (DFB) lasers, where the lasing cavity supports standing-wave longitudinal modes, in an SRL cavity there are two counter-propagating, travelling wave longitudinal modes. Depending on the geometry and the bias current of the device only one of these modes is above lasing threshold, while the other one is suppressed due to gain competition, i.e. the device lases unidirectionally, only in one direction. A device with such two stable states forms an optical bistable and it becomes natural to associate the “high” and “low” or “0” and “1” states of a binary logic to these two lasing directions, as illustrated in Figure 1.1. On the right side a sketch of a typical P–I

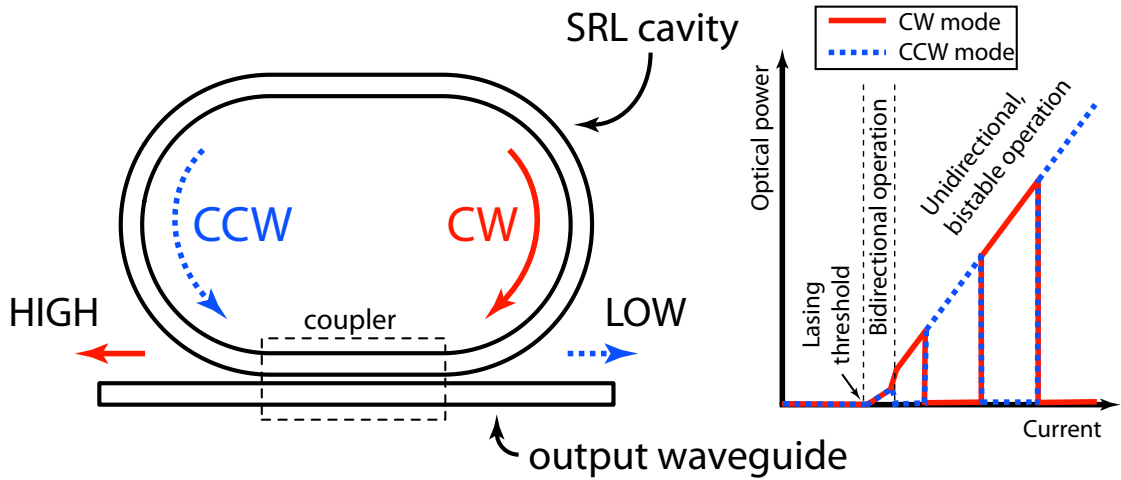


**Figure 1.1:** Schematic illustration of a bistable SRL. On the right side a typical SRL P–I curve is shown. On the P–I curve the solid line (red) denotes the CW propagating longitudinal mode of the SRL while the dashed line (blue) corresponds to the CCW propagating longitudinal mode.

curve illustrates the operation regions of a SRL.

Such an SRL bistable shows great potential as an all-optical single bit memory element, since its actual state can be read purely optically via the output waveguides, and can be written by switching the lasing direction with external optical pulses that are counter-directional to the current lasing direction.

A gain or loss asymmetry induced in an SRL cavity by geometrical design or external optical injection forces the SRL to operate in a unidirectional regime. In this configuration, the SRL becomes an optical monostable that finds numerous applications in all-optical signal processing. For example, if an external HB is injected in one direction, the lasing direction of the SRL can only be switched with a counter-directional optical pulse or *cw* beam that has a stronger power than the HB. After removing the counter-directional excitation the SRL restores to the optical state defined by the HB. This kind of operation can be exploited to create various all-optical logic gates, such as the NOT, the NOR or the NAND gates, as illustrated in Figure 1.2.

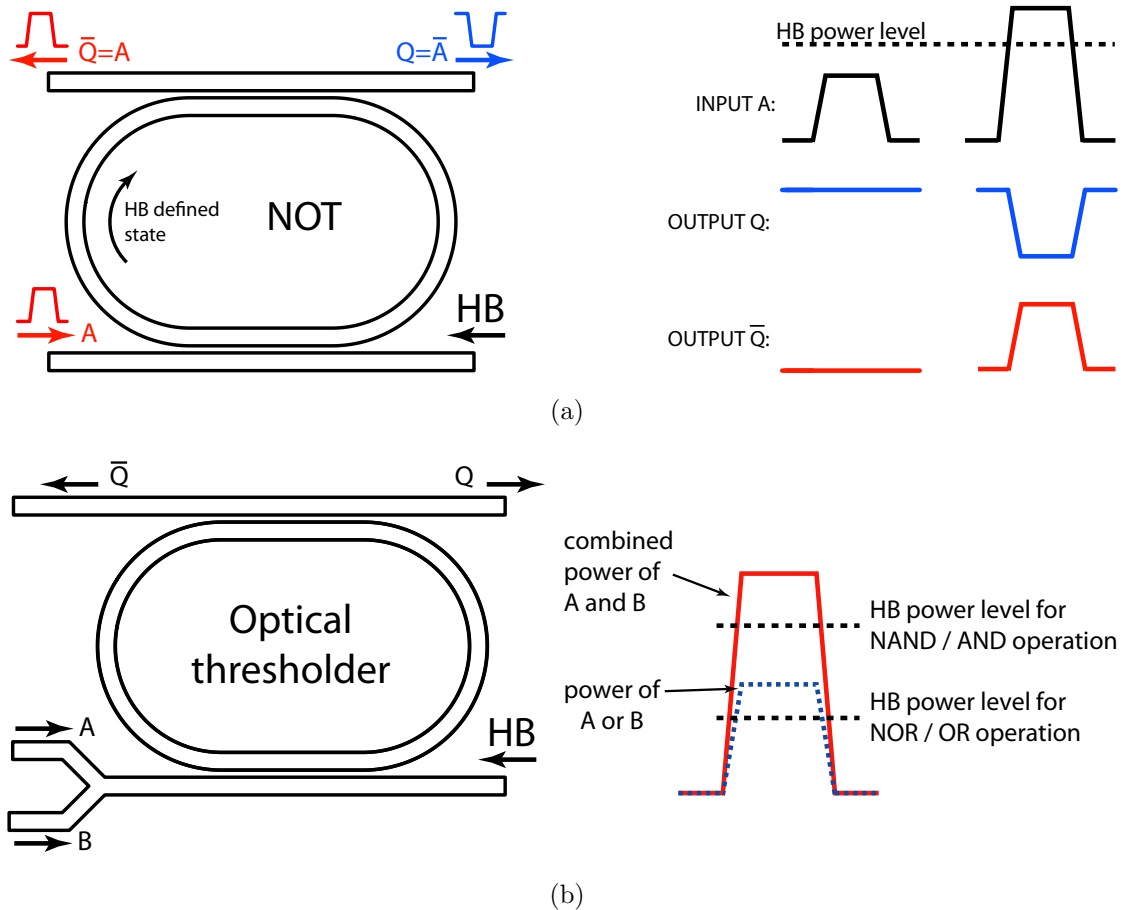


**Figure 1.2:** Schematic illustration of all-optical logic gates that are based on a SRL monostable. (a) Schematic of an all-optical NOT gate and its principle of operation. (b) Schematic of an all-optical thresholder. The diagram on the right shows its operation in a NAND and a NOR configuration.

## 1.4 Review of the major contributions to SRL research

The first reported semiconductor ring laser with four cleaved facets forming the closed loop cavity dates back to 1976 and was reported by D. Scifres et al. [23]. In the following two decades various cavity geometries were proposed and demonstrated, such as circular [24,25], racetrack [26,27] and triangular [28]. These designs employed various light guiding mechanisms such as the “whispering gallery” effect of the pillbox structure [25], deeply etched or rib-waveguides [26,27] shallow etched ridge-waveguides [20] and buried heterostructures [29].

J. Hohimer and colleagues carried out an extensive research in the field of SRL in the 1990s at the Sandia National Laboratories, Albuquerque, New Mexico. The efforts of the group concentrated on the design of cavities for single mode and high side mode suppression ratio (SMSR) operation [30, 31, 32], as well as on rings with a cross-over waveguide (a *yin-yang* like cavity geometry) to force unidirectional operation [26]. They also reported on the effect of the feedback from the cleaved output mirrors on the operation and the output power level of a SRL [33]. Furthermore, they were first to demonstrate a passively mode-locked ring laser and to highlight its potential for accurately defining the repetition rate (i.e. cavity length) by lithography [34]. The monolithic integration of this mode-locked ring with a millimeter-wave waveguide and a fast detector yielded one of the first millimeter-wave generating PIC [35].

In the same period, forced unidirectional operation was investigated by the photonics group at Cornell University, New York. The approach of J. Ballantyne and co-workers was to create a loss asymmetry by introducing a waveguide tapering section that widens the waveguide gradually followed by an abrupt section that connects to the original width [36]. All the devices fabricated by the group employed a triangular shape cavity design with two etched total internal reflection (TIR) mirrors and one cleaved mirror [37, 38]. Such a geometry makes planar integration cumbersome but it provides an easy and straightforward solution for power extraction. Recently, based on the TIR technology, a rhombus-shaped SRL [39] was introduced in the product portfolio of Binoptics<sup>2</sup>, a spin-off company related

---

<sup>2</sup><http://www.binoptics.com/>

to the group.

In 1994 researchers at Philips demonstrated efficient light out-coupling from SRL using MMI couplers and MMI combiners. Later, in collaboration with COBRA<sup>3</sup>, their attention focused on the investigation of an SRL with arrayed waveguide gratings (AWGs) for creating digitally tunable lasers [40,41]. Later, they presented a passively mode-locked, active - passive integrated extended cavity SRL [42] and a passively mode-locked quantum dot SRL [43]. In parallel, Martin Hill and co-workers at the same group demonstrated the pulsed operation of 16  $\mu\text{m}$  diameter coupled rings that could be operated as an optical bistable with a rise time of  $\sim 20$  ps for 13 ps full width half maximum (FWHM) pulses [21]. Recently, in the frame of the EU project HISTORIC<sup>4</sup>, a III-V/silicon on insulator (SOI) integration platform was developed. This year, based on this platform, COBRA demonstrated 7.5  $\mu\text{m}$  diameter *cw* room temperature lasing SRLs with 60 ps switching time [22].

The research on SRLs at University of Glasgow was initiated in the late '80s by Peter Laybourn, who pioneered most of the SRL research worldwide. One of his students - Thomas Krauss - demonstrated the first *cw* and room temperature lasing, low threshold, circular ring lasers using deep etching waveguide technology and a pillbox geometry [25,44]. Later, using weakly guiding shallow etched waveguides and MMI couplers they presented highly efficient racetrack shape SRLs [45,46,47]. Another student of Peter Laybourn - Siyuan Yu - investigated large size, passively mode-locked SRLs [48,49]. Finally, Marc Sorel, in the late '90s was the first to realize that SRLs operate naturally in a unidirectional lasing regime when the feedback from the output facets is low [50,51]. He also predicted and experimentally confirmed the operating regimes of SRL as a function of the bias current: bidirectional, alternate oscillations and unidirectional [20]. Recently, his student Sándor Fürst investigated the modal behaviour of SRLs [52] and demonstrated the monolithic integration of SRLs with distributed Bragg reflectors [53].

---

<sup>3</sup>Inter-University Research School on Communication Technologies Basic Research and Application

<sup>4</sup><http://www.ict-historic.eu/>

## 1.5 Objectives of this thesis and organisation of the chapters

This thesis investigates the design issues and the fabrication technology of 1550 nm lasing wavelength SRL that are intended for all-optical signal processing applications. More specifically, this work developed around the following objectives:

- Development of a reliable and high yield SRL design and technology for producing pilot devices with robust and repeatable unidirectional bistable operation, which can be used for the systematic investigation of SRL temporal dynamics and directional bistability.
- Establishment of the necessary technology and design platforms to allow the geometrical size down-scaling of SRLs in order to allow a more dense monolithic integration of these devices.

The first objective is realized using the very mature and robust technology previously developed at Glasgow for the fabrication of FP lasers. A detailed analysis of the cavity building block design is performed with particular attention on the low bending losses of the weakly guided shallow etched waveguide geometry and on the minimal intra-cavity and extra-cavity back-reflections. The latter is especially important since the coupling of the counter-propagating modes, caused by reflections, deteriorates the robustness and the quality of the unidirectional bistable operation. The second objective requires the design and fabrication of tight bends (sub-10  $\mu\text{m}$  radius) with strong optical mode confinement and minimal bending losses. Various etch chemistries are investigated and optimised in order to define the deeply etched waveguide geometry required for strong mode confinement and the low sidewall roughness, which is crucial for low sidewall scattering and hence low intra-cavity back-reflections. Several design issues for deeply etched ring cavity designs are investigated, including efficient output couplers and adiabatic straight to curved transitions for minimal coupling of the counter-propagating modes. The acquired fabrication and design know-how is utilized to fabricate shallow and deeply etched SRLs and to assess their switching performance. In the last part of the work these devices are used to demonstrate SRL based high speed all-optical flip-flops and logical gate functionalities.

The majority of the work dealt with the fabrication, design and characterization of large size and small size SRL devices that lase *cw* and show robust unidirectional bistable operation. Although fabrication and device design issues are highly interwoven, they are discussed separately as such an arrangement is more clear. The chapters are organized as follow:

**Chapter 2** provides an overview on the fabrication technologies for both the shallow etched and the deeply etched SRLs. The developed and optimised lithographic, dry etching and planarization techniques are thoroughly detailed and analyzed.

**Chapter 3** introduces the epitaxial material used for this work. Based on the measured laser characteristics, basic material parameters are extracted, such as:  $g_0$ ,  $J_0$ ,  $\alpha_i$ ,  $\eta_i$  etc..

**Chapter 4** presents the design considerations for shallow etched SRL devices. Waveguide losses, bending losses and coupling configurations of the ring cavity are investigated. Furthermore, the back-reflection from the output waveguide facets are evaluated in order to improve the robustness of the unidirectional SRL operation. Finally, the steady-state characteristics of the fabricated shallow etched SRL are measured and discussed.

**Chapter 5** reports on the design considerations for deeply etched SRL devices. The optimum waveguide geometry for low bending losses and single transverse mode operation is investigated theoretically and experimentally. Non-radiative loss mechanisms of deeply etched waveguides are reviewed and assessed with the objective of achieving low threshold current operation. The various options for extracting optical power from the lasers are analysed. Adiabatic straight to bend transitions are also evaluated in order to keep the intra-cavity back-reflections as low as possible. Finally, small footprint SRLs with robust unidirectional operation are fabricated and characterised.

**Chapter 6** demonstrates high speed all-optical flip-flop operation based on SRL devices and investigates the SRL switching speed. SRLs integrated with DFB devices are used to demonstrate monostable operation and to characterise the switching

speed of an SRL based all-optical NOT gate.

# Chapter 2

## Fabrication

In the following sections the assessment and development of the fabrication steps of SRLs are described. First a coarse overview of the process flow is given. Then a more detailed analysis is presented on the key processes for which major development and optimisation was carried out in the framework of this work.

### 2.1 Overview of the process flow

The main processing steps for fabricating a semiconductor laser are summarised in the block diagram of Figure 2.1. This process flow applies to the majority of semiconductor lasers fabricated in our cleanroom, regardless of the material or cavity geometry. However, details such as layer thickness, etching recipes or electron-beam (e-beam) doses are specific to the type of device or geometry to be fabricated. Critical steps in the process flow are marked with red boxes. The inspections and/or measurements taken at these points may require reiteration of a step (e.g. if a slightly longer etch is needed) or repetition of one or more steps (e.g. if the thickness of the resist mask is insufficient to etch the contact window). The red arrows indicate from where to resume processing if fabrication was halted due to a problem. A more detailed description of the fabrication flow is available in [52] and in [54].

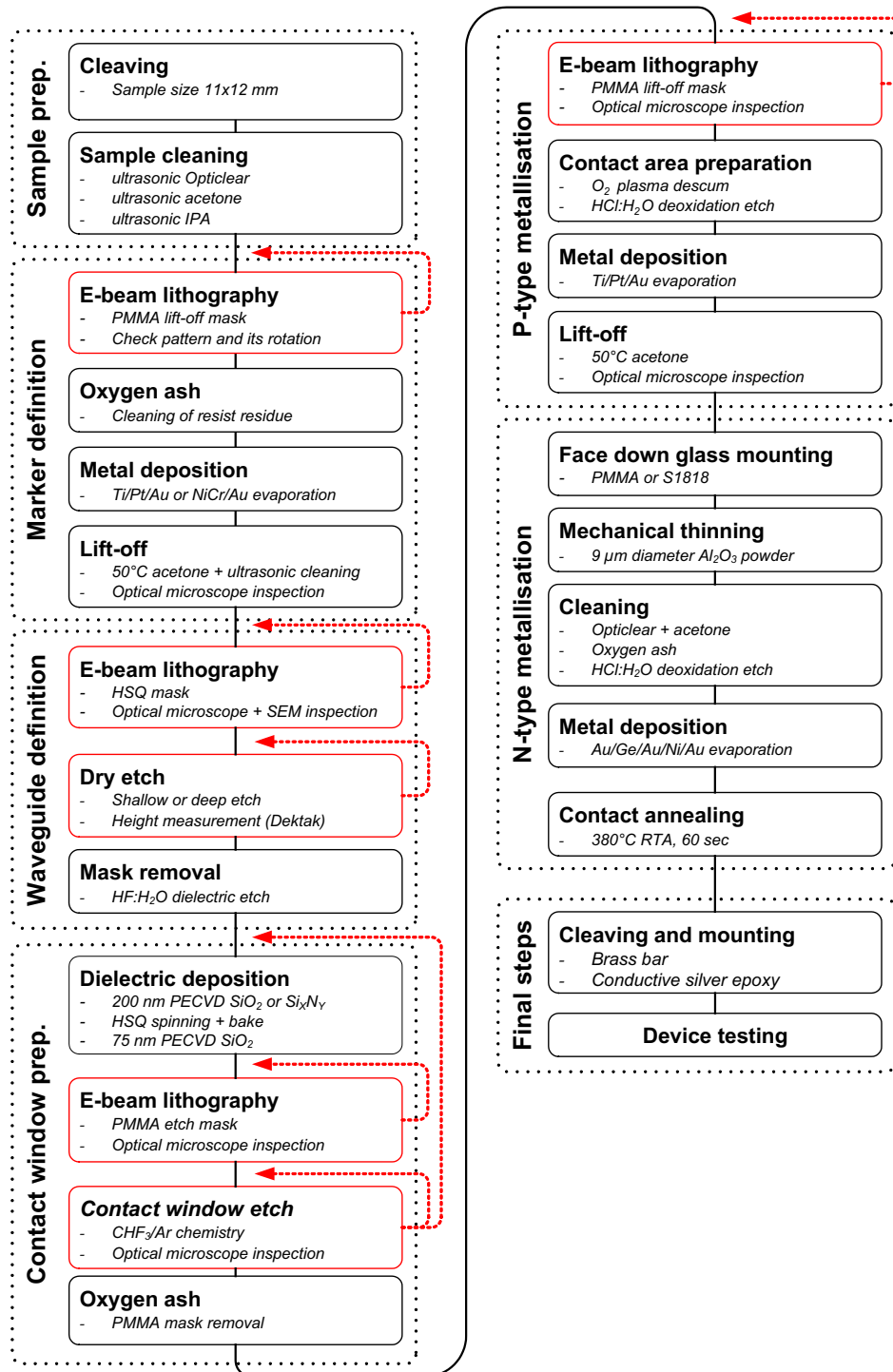


Figure 2.1: Simplified process flow of the fabrication steps of semiconductor lasers.

## 2.2 Sample preparation

The processing starts with the cleaving of a two inch epitaxial wafer. An  $11 \times 12$  mm sized chip reduces material waste and provides a big enough useful area to accommodate a large number of devices. As cleaving is carried out in a non- or semi-clean environment it is necessary to have a thorough cleaning of the chip before further processing. Samples are immersed into an ultrasonic bath in plastic beakers for 5 minute each in opticlear, acetone and isopropyl alcohol (IPA). After the last soak, the remaining layer of IPA is blown from the sample surface with a nitrogen gun. This is followed by a 3 minute ash in oxygen plasma to remove any possible residue of the solvents. Before drying, an extra 5 minute ultrasonic cleaning in reverse osmosis water (RO-water) can be used. The adsorbed water on the surface may decrease resist adhesion, which is especially problematic in case of narrow features. Therefore a few minutes bake on a hot plate is recommended at  $90^\circ\text{C}$  if the RO-water step is used.

## 2.3 Lithography

Crucial steps in the process flow are the patterning of the etch or lift-off masks and the accurate alignment of these masks relative to the previous pattern. Photolithography, the workhorse of the CMOS industry, has the capability to produce the patterns required for micro- or nano-sized lasers, but the large cost of such equipment, makes its operation only profitable when used for mass-production. The small throughput requirement of research and development makes other lithographic tools like direct e-beam writing a good alternative. E-beam lithography provides a very flexible and high-resolution tool for device and process development, and as design changes from chip to chip it is highly suitable for prototyping.

During this work a Leica Vector Beam 6 electron lithography tool was used to pattern both positive and negative tone resists. Figure 2.2 shows the exposure mechanism of both resist types. A positive tone resist is insoluble in the developer (see Fig. 2.2(a)), where it was not exposed by electrons, while a negative tone will be remain where exposed (see Fig. 2.2(b)). Hydrogen silsesquioxane (HSQ) - a negative tone type, electron sensitive dielectric - served as a waveguide etch mask. The lift-off and dielectric etch masks of the subsequent layers were defined with

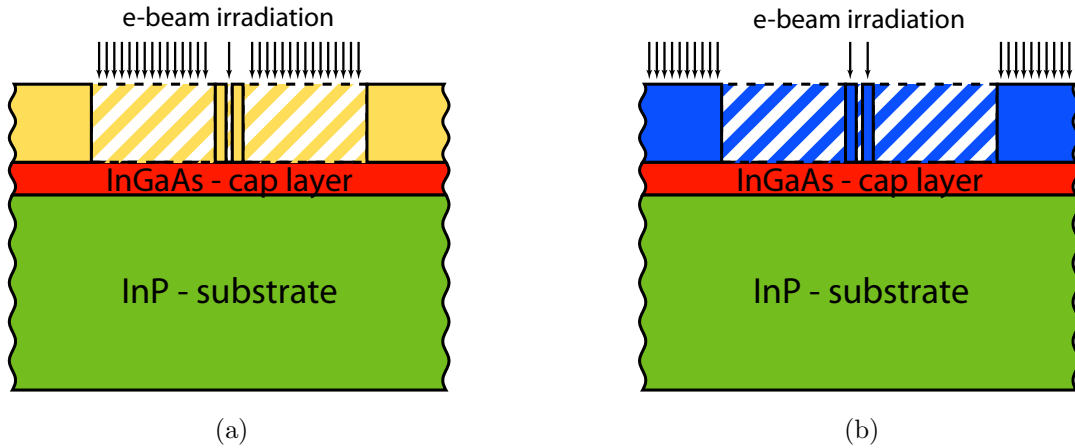


**Figure 2.2:** Schematic of exposure of (a) positive and (b) negative tone type resists.

polymethyl methacrylate (PMMA), a positive tone type, high resolution polymer.

### 2.3.1 HSQ resist

Minimisation of waveguide losses and back reflections due to sidewall scattering requires the patterning of a mask with very low edge roughness. The standard waveguide fabrication process consists of the lithographic step for the waveguide mask (using PMMA, for example) and the subsequent definition of a separate hard mask by dry etching. Each of these steps enhances the mask roughness which directly transfers to the waveguide sidewalls during the subsequent etching. These two mask preparation steps and their contribution to sidewall roughness can be avoided by using an e-beam sensitive spin on dielectric, like HSQ, as the etch mask. This way, very smooth sidewalls can be achieved where the mask roughness is truly in the order of a few nanometers, as illustrated in Figure 2.3(a). The loss reduction capability of this technique was already demonstrated with SOI waveguides [55]. The usual etch depth of SOI waveguides is few hundred nanometers, while in the case of compound semiconductor lasers, where upper claddings are 1-2  $\mu\text{m}$  thick, etches as deep as 3-5  $\mu\text{m}$  are necessary. A further requirement of the resist is to be able to clear out at least 100 nm wide gaps between two waveguides, e.g. to fabricate narrow point or evanescent field couplers. These above two requirements contrast each other, since deep etches require thick masks, while for small features thin resist

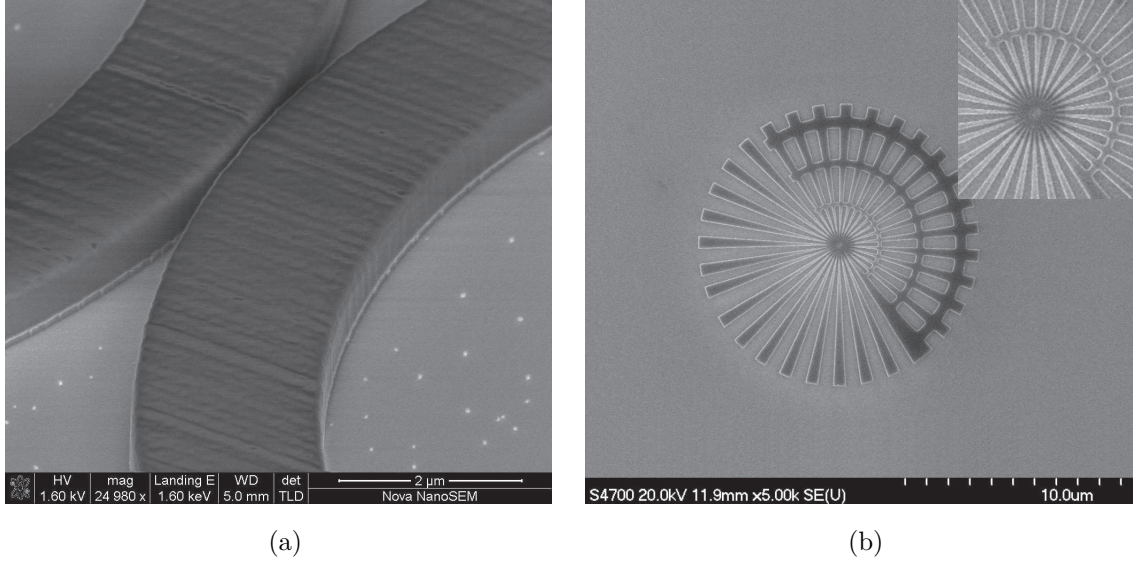


**Figure 2.3:** SEM images of exposed and developed 580 nm thick HSQ patterns. (a) A 100 nm wide point coupler between two circular tracks. The low roughness of the resist sidewall as well as the undulation on top of the HSQ - a result of the scanning e-beam writing - can be observed. (b) A test pattern of which radial lines and gaps are linearly narrowing when approaching the origin. The concentric tori with external radius of 600 nm, 400 nm and 200 nm help the quick evaluation of the smallest open gap width. The inset in the top right corner shows a two times magnification of the image central section.

layers are advised. To evaluate if the HSQ conforms with these two specifications its imaging aspect ratio needs to be checked first. Figure 2.3(b) shows a gear-shaped test pattern which was used to identify the size of the smallest reproducible gap of a 580 nm thick resist layer, measured to be as small as 50-60 nm wide. Accordingly, a  $\sim 600$  nm thick HSQ layer has a worst case imaging aspect ratio of at least 10. Based on this evaluation and on the specified gap width (100 nm), the maximum resist thickness that can be used is as thick as  $1 \mu\text{m}$ . In order to keep fabrication simple and to have a safe margin on the fabrication tolerance, an HSQ thickness of 600 nm was chosen to be used for the lithography of the devices. The maximum achievable thickness with a single spin of the FOX-16 HSQ, without losing on quality, was measured to be 650 nm.

Because the mask dry etch selectivity for most III-V materials ranges from 6

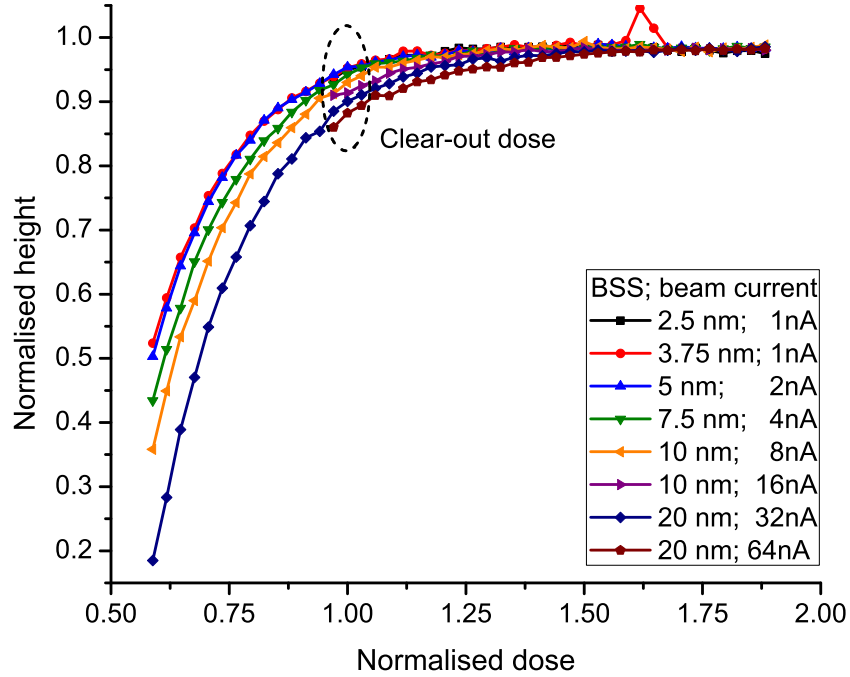


**Figure 2.4:** Measured contrast curves of a 600 nm thick HSQ layer. The corresponding resolution and beam current of each data series is indicated on the plot. Doses were normalised to  $340 \mu\text{C}/\text{cm}^2$ , which is the clearing dose for this height.

to 12, one can achieve waveguide depths of  $2.4 \mu\text{m}$ - $5.4 \mu\text{m}$  with a 600 nm HSQ thickness. These figures are calculated based on the assumption that mask edge erosion starts to effect the sidewall smoothness after 400 - 450 nm of a 600 nm thick mask is removed during the etch. These estimated etch depths are sufficient for the deep etched structures that will be discussed in Section 2.4.2.

Before utilising the resist to pattern “real” devices a test needs to be prepared to identify the optimum electron dose. The easiest procedure is to expose small patterns with a stepwise incremented dose. After development the resist height for each dose can be measured and plotted to yield the so-called contrast curve. Figure 2.4 shows eight contrast curves prepared with a pattern consisting of a 500 nm and a  $1 \mu\text{m}$  gap evanescent field couplers. The data set of each curve was measured from patterns on the same chip, which were exposed with different beam step size (BSS) and beam current settings (see legend for values). The dose corresponding to the “knee” of the curve is the clear-out dose of the resist. An unexpected result on the graph is that with decreasing BSS (increasing beam

current) the sloped part of the contrast curves is shifted towards higher doses, i.e. their clear-out dose increases. This shift is most likely a result of the imperfect compensation of the forward scattered electrons. As a consequence, each time a dose test is prepared, attention must be paid in using a BSS identical to the BSS of the real pattern. A more advanced proximity correction software should take into account the change of the spot size as function of the beam current and therefore make the dose independent from the BSS.

### 2.3.2 PMMA resist

PMMA is a very high resolution positive tone resist. When used as a thin film of few hundred nanometers it has similar or even better resolution than HSQ. The usual etch selectivity of the resist versus  $\text{SiO}_2$  or  $\text{Si}_3\text{N}_4$  in fluorine based plasma, such as  $\text{CHF}_3$ , is around 1:2 (i.e. the resist is etched two times faster than the dielectric). As a consequence, a robust fabrication requires  $1\ \mu\text{m}$  thick resist in order to etch a  $300\ \text{nm}$  dielectric layer. After etching, the dielectric can be used as a highly selective semiconductor etch mask or it can serve as a contact window when used as an insulating layer between the semiconductor and the metallisation.

Uniformity of the layer thickness over the sample is maintained by spinning double resist layers. First, a thicker  $1.2\ \mu\text{m}$  resist layer is spun, which is followed by a  $110\ \text{nm}$  thick layer. Undercut resist profiles can be formed by choosing a lower sensitivity (higher molecular weight) PMMA as the top layer. These ledges prevent the sidewall of the resist to be coated during metal evaporation and thereby allow reliable metal lift-off (see Figure 2.5).

### 2.3.3 Proximity correction

Electrons propagating in a material collide inelastically with the atoms of the lattice. As a result of the collisions, energy is transferred to the material and the path and energy of the incident particles, the primary electrons, change and the well focused, few nm spot electron beam spreads out. Figure 2.6 shows the simulated trajectory of a one hundred element,  $100\ \text{keV}$  energy electrons in InP with a  $1\ \mu\text{m}$  thick HSQ layer on the top. Electrons, which do not return to the resist after passing through the resist-substrate interface are called forward scattered electrons and they are plotted with a blue line. These particles transfer energy to the resist only

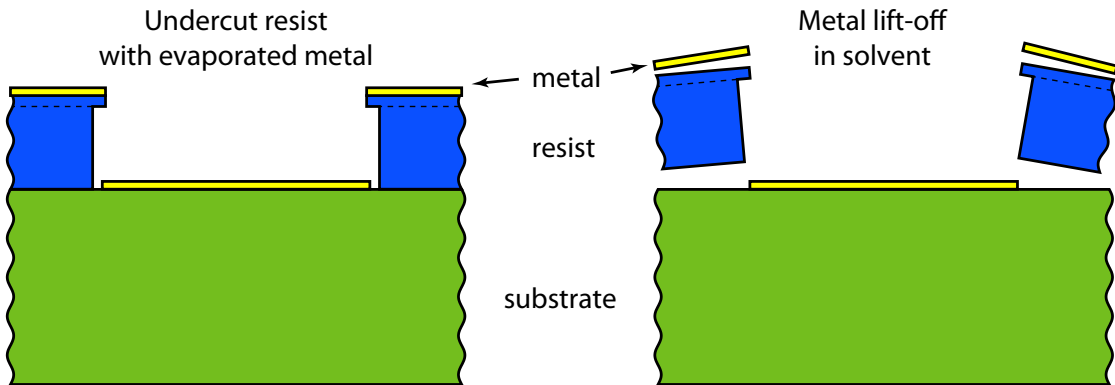


**Figure 2.5:** Schematic illustrating metal lift-off with undercut profile resist.

once, as they pass through. Trajectories, which lead back to and sometimes even out of the resist, belong to backscattered electrons and are coloured in red. Such electrons not only contribute to the exposure at their point of incidence but also at places where they propagate back to the resist. As a consequence, they contribute to its exposure over a large area and so e-beam irradiation in one location affects surrounding areas. Therefore the exposure dose in a point needs to be calculated as the sum of primary electrons and the backscattered part of the e-beam irradiation from its proximity, herefrom comes the name: *proximity effect*. In order to be able to compute exposure dose corrections for various patterns, the amount of energy deposited by forward and backscattered electrons has to be calculated analytically. One approach is to model the deposited energy to the resist layer with a double Gaussian distribution, the so called proximity function [56]:

$$f(r) = \frac{1}{\pi(1 + \eta)} \left[ \frac{1}{\alpha^2} \exp\left(-\frac{r^2}{\alpha^2}\right) + \frac{\eta}{\beta^2} \exp\left(-\frac{r^2}{\beta^2}\right) \right], \quad (2.1)$$

where  $r$  is the radial distance from the point of incidence,  $\alpha$  is the beam size as a result of forward scattering, the term  $\beta$  is the backscattering range and  $\eta$  is the deposited energy ratio of incident electrons to backscattered electrons. Typically  $\alpha$  is below  $0.1 \mu\text{m}$  and  $\beta$  can range up to a few tens of  $\mu\text{ms}^1$ . The parameters of the proximity function can be measured experimentally [57] or they can be determined from simulations [56].

<sup>1</sup>It is also notable that the wavelength of electrons with energies around 1 keV and higher is below 0.1 nm, therefore diffraction does not limit the resolution of today's e-beam systems.

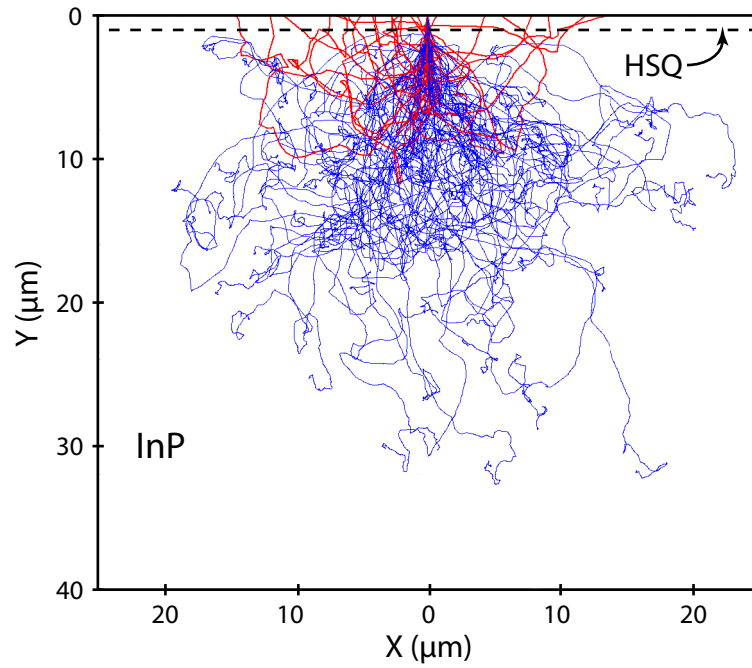


**Figure 2.6:** Simulated trajectories of one hundred 100 keV electrons through 1  $\mu\text{m}$  HSQ and 40  $\mu\text{m}$  InP. Electron paths were computed using CASINO (<http://www.gel.usherb.ca/casino/>).

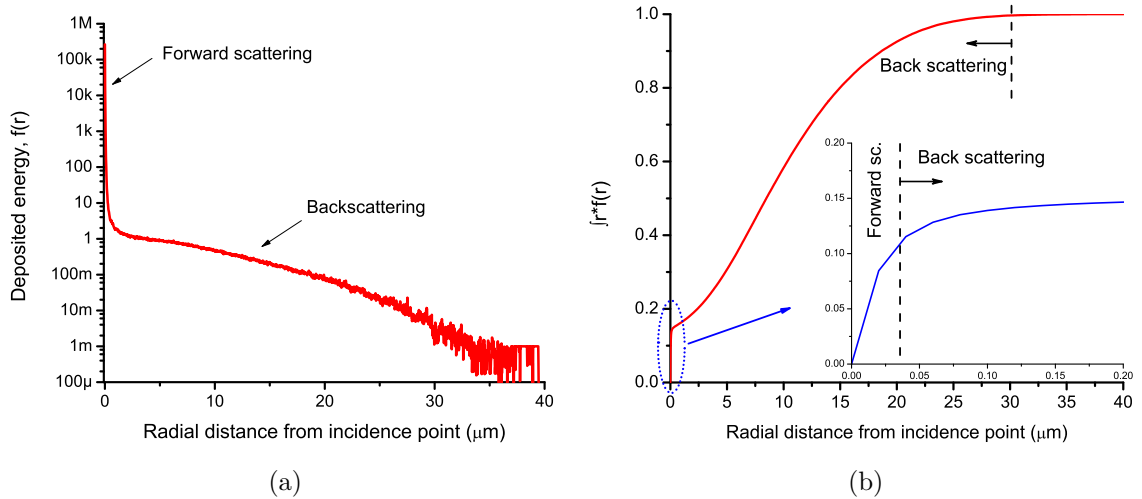


**Figure 2.7:** (a) Simulated distribution of the energy deposited by electrons as a function of the radius. (b) Plot of  $\int r * f(r)$  as a function of the radial distance from the incidence point.

Using a commercially available Monte Carlo tool, *Skeleton*, the trajectories of 1 million, 100 keV electrons were traced along their propagation through a 600 nm HSQ resist and then in the epitaxial material that was used for this work (see Table 3.1, page 36). The distribution of energy deposited in the bottom 25 nm layer of the resist as a function of the radial distance ( $r$ ) from the point of incidence can be seen in Fig. 2.7.a. It is apparent that the main part (98%) of the deposited energy at the resist-substrate interface is in a narrow, 20 nm diameter spot. The forward and back scattering regions can be clearly identified, but their boundaries can not be determined from this graph. In order to find these ranges it is more helpful to plot the integral of the product between the radius and the distribution function ( $\int r * f(r)$ ). Figure 2.7.b shows the integral of  $r * f(r)$  as a function of the radial distance from the incidence point. The range of forward broadening is around 20-30 nm. Above a radius of 30  $\mu\text{m}$  the integral becomes constant<sup>2</sup>, which means there are no electrons reentering the resist. This value is taken as the backscattering range of the material and e-beam irradiation from points outside of this region does not contribute to the dose anymore. Such far lying patterns can be excluded from the proximity correction calculations.

The simulated proximity data was post-processed with PROXECCO, in which fracturing parameters and dose correction strategies were customised to assign proper doses to diverse features such as: dense areas, optical gratings, evanescent field couplers with sub-micrometer gaps, simple waveguides and large blocks. Figure 2.8 shows two fractured patterns requiring different proximity correction strategies. A square with sides of 40  $\mu\text{m}$  (see Figure 2.8.a) has a dose multiplier of 1.24 in the middle and the dose increases gradually to the corners until it reaches 2.82 times the base dose. The increased dose in the corner areas compensates for the lower amount of backscattered radiation in these regions. This dose adjustment not only results in sharp, well defined corners, but also creates a wider and more robust process window for these simple features, i.e. these patterns become less sensitive to the fluctuation of external process parameters. A lithographically more challenging feature is the correct exposure of sub-micron gaps. In order to avoid over exposure of the gaps, the dose of their surrounding areas has to be reduced accordingly. This strategy is well illustrated in Figure. 2.8.b, where a 16  $\mu\text{m}$  radius

---

<sup>2</sup>A continuously increasing integral would mean that the exposure results in an infinite dose and this does not make any physical sense.

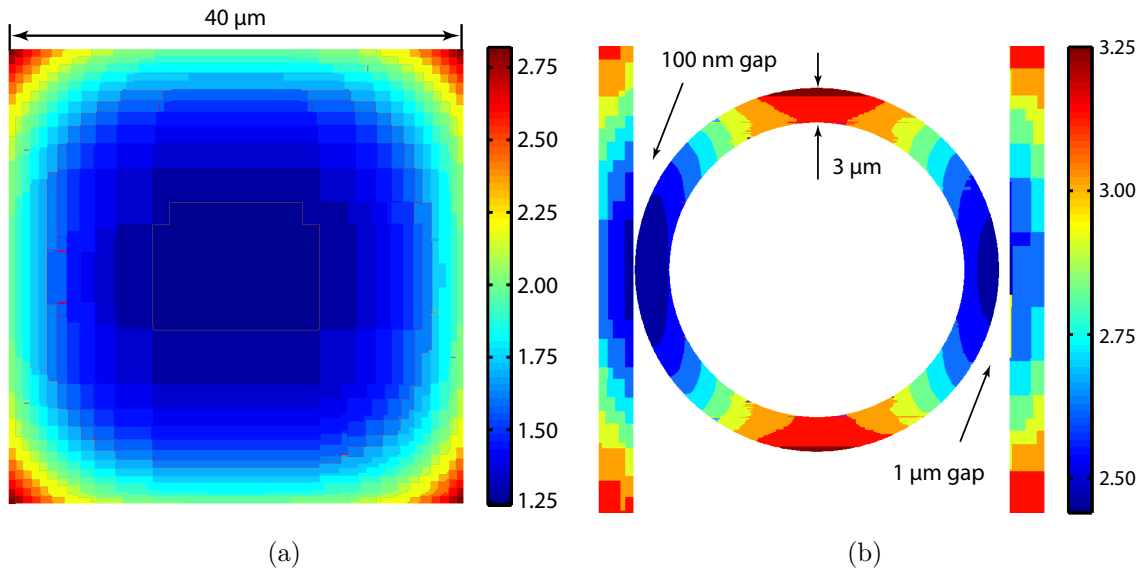


**Figure 2.8:** Iso-dose maps of fractured and proximity corrected patterns. (a) The applied dose distribution of a  $40\ \mu\text{m}$  size alignment mark. (b) The dose map for a  $16\ \mu\text{m}$  radius ring resonator. The bars on the left side link the colours with the corresponding multiplier of the base dose.

ring has a  $100\ \text{nm}$  point coupler on the left side and a  $1\ \mu\text{m}$  one on the right side. To compensate the extra backward scattered electrons exposing the  $100\ \text{nm}$  gap the dose around the gap is lowered in an area that is larger than that of the  $1\ \mu\text{m}$  gap geometry.

The proximity correction can never be ideal, since a proper dose correction would require the application of negative doses. However, even a non-ideal correction still greatly enhances the e-beam pattern quality. Its main advantages are:

- Various patterns such as optical gratings, narrow evanescent couplers and big blocks require a different clear-out dose due to the different amount of backscattered radiation they experience. Setting these doses manually is rather time consuming. Instead, by applying the proximity correction the dose of each pattern is adjusted automatically during fracturing.
- Proximity correction increases the size of the process window for “simple” patterns such as few micron large waveguides or large patterns. This way

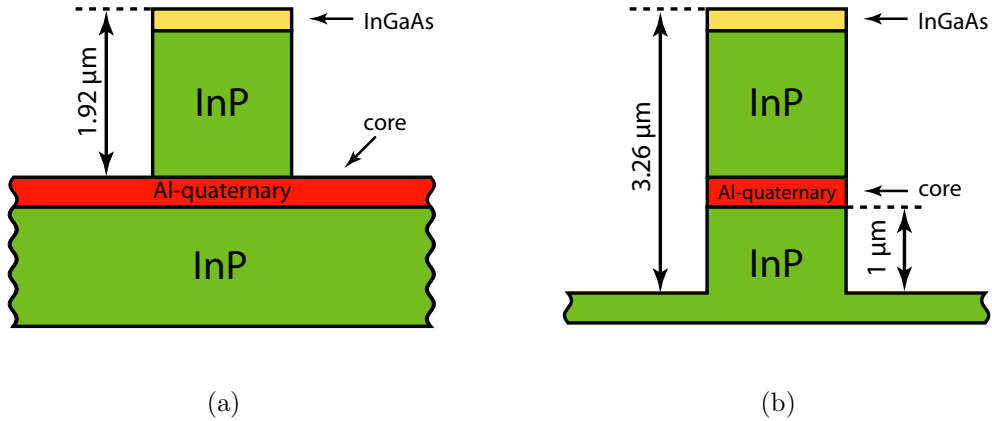


**Figure 2.9:** Schematic of the cross section of (a) a shallow etched waveguide and (b) a deep etched waveguide.

these features are less sensitive to process fluctuations like developer or pre-baking temperature.

## 2.4 Dry etching

The reactive ion etching (RIE) of InP based compound semiconductor devices is a mature research field. Several etch chemistries and technologies exist and each produces good sidewall verticality and reasonable mask selectivity. The majority of these processes are based on  $\text{Cl}_2$  [58, 59, 60, 61] or on  $\text{CH}_4/\text{H}_2$  [62, 63]. Chemistries including chlorine have fast etch rates and good sidewall qualities, but they require elevated temperatures ( $150^\circ\text{C}$  or higher) to remove the non-volatile etch product,  $\text{InCl}_x$ . Such a high platen temperature prevents the use of temperature sensitive resists, like most photoresists, as an etch mask. Methane based chemistries have lower etch rates, but the hydrocarbon by-products of the  $\text{CH}_4$  form a polymer film on the surface, which reduces waveguide undercut and protects the sidewalls from etch damage. On the other hand chamber contamination and slow etch rates are unwanted side effects of polymer formation.

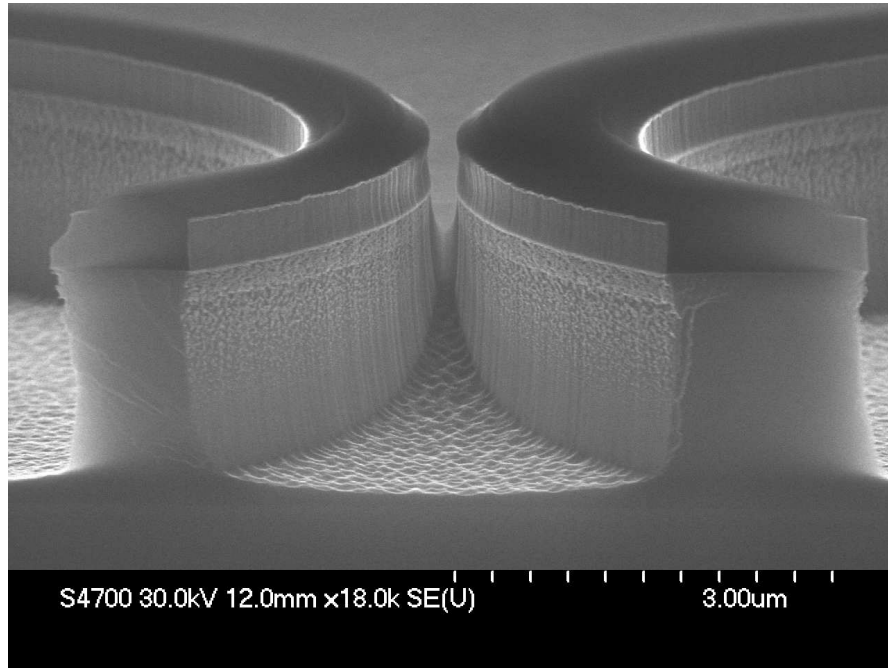
Figure 2.9 shows the cross section of the shallow and the deep etched waveguide geometries that will be extensively discussed in the following chapters. Etching is required to stop on the top of the active core for shallow etched devices (see

Fig. 2.9(a)). Characteristic properties of a waveguide of this type are: weak horizontal optical confinement, low sidewall recombination losses and moderate bending losses (more details can be found in Chapter 4). Also, a shallow etch places more relaxed demands on the dry etch mask. This technology is ideal to fabricate medium to large size SRLs but is unsuitable for micro-rings with very tight bends. A stronger horizontal mode confinement can be achieved with deeply etched waveguides (see Fig. 2.9(b)). Strong horizontal optical confinement, increased sidewall recombination losses and minimal bending losses are the typical features of these waveguides (more details can be found in Chapter 5). In the following part of the section one shallow and three deep etch techniques will be discussed. Existing and well assessed chemistries were investigated and optimised, but also new ones were developed.

### 2.4.1 Shallow etch

Shallow etched devices require accurate control of the etch depth to stop precisely above the core of the material (usually few tens of nanometers). With interferometric techniques the etch depth can be monitored real time and the etch can be stopped at the desired depth [64]. An other approach is to use optical emission spectroscopy to monitor the changes in plasma composition, which occurs at the transition between different epitaxial layers [65]. A third possibility is to use chemistries that have a high selectivity between InP and core layers, namely an etch stop layer. This approach also solves the problem of the reduced etch rate in sub-micrometer gaps – this effect is called RIE lag. In these narrow gaps the etching speed is slower than in large open areas. The presence of an etch stop layer allows for an over-etch that completely clears out the narrow gaps while keeping the depth of the large areas almost unchanged. Highly selective etching of InP over Al-quaternary materials can be achieved with  $\text{CH}_4/\text{H}_2/\text{O}_2$  chemistries [63], in which the added oxygen reacts with the core layers by oxidising the aluminium content. As a result, a thin  $\text{Al}_2\text{O}_3$  film is formed on the surface that protects the core layer and therefore strongly decreases the etch rate.

Based on the parameters reported in [63], a  $\text{CH}_4/\text{H}_2/\text{O}_2$  etch process was developed by Sándor Fűrst at the department [52]. Later, when the dry etch facilities moved to the newly built James Watt Nanofabrication Centre (JWNC) polymer



**Figure 2.10:** SEM photograph of the point coupler region of two  $20\ \mu\text{m}$  radius rings. The test pattern was cleaved  $\sim 10\ \mu\text{m}$  from the point coupler.

formation problems required the re-adjustment of  $\text{O}_2$  flow rates. The parameters used to etch the devices are: 50 W RF power, 30 mT chamber pressure (open valve) and  $\text{CH}_4/\text{H}_2/\text{O}_2$  flow rates of 6/54/0.8 sccm, respectively. Average etch rates<sup>3</sup> of around 40 nm/min and a mask selectivity of better than 10 was observed. The etch rate of the upper core layers (composition: InAlGaAs) was measured to be around 1 nm/min, which corresponds to an etch selectivity of more than 30:1. Figure 2.10 shows the cross section of a double ring pattern, which was etched for 45 mins. Surface smoothness is good, only tiny vertical grooves, formed as the consequence of ions sliding down the sidewall, are observable. An other noticeable feature is the polymer film covering the upper half of the waveguide.

Tests aiming at comparing the performance of HSQ and  $\text{SiO}_2$  masks revealed that etch rates greatly depend on the size of the etched area. Figure 2.11.a shows the change of etch rate as a function of the chip area. Though the measured points are quite scattered, a decreasing trend with increasing area is clearly visible. This

<sup>3</sup>The average etch rate is calculated from a 35 minute long etch of the material.

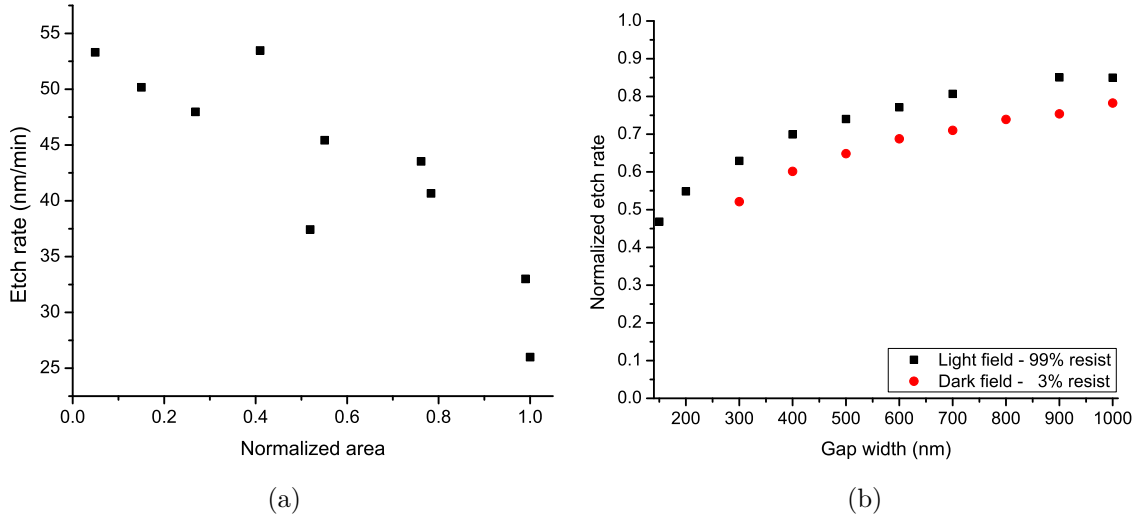


**Figure 2.11:** (a) Measured etch rates as function of the etched area. Normalised area 1 is equal to a size of  $132 \text{ mm}^2$  ( $11 \times 12 \text{ mm}$ ). (b) Measured etch rate as a function of the gap width. Light and dark field points were normalised to the large area etch rates  $55 \text{ nm/min}$  and  $39 \text{ nm/min}$ , respectively.

is explained with the increased local loading of the plasma, which results in reduced chemical etch components and leads to slower etch speeds. This was confirmed by etching two,  $121 \text{ mm}^2$  size, p+ InP samples that were patterned with a resist cover density of 3% and 99%. The light field chip (most surface covered by resist) had an etch rate of  $55 \text{ nm/min}$  while the etch rate of the dark field sample was measured to be  $39 \text{ nm/min}$ , i.e. the increased plasma loading decreased the etch rate of the sample with low pattern density. A further important result of this comparison is that the normalised etch rate of the narrow gaps decreases as the loading of the plasma increases (see Figure 2.11.b). Since chips with different pattern densities and sizes have different plasma loading, it is particularly hard to predict the etch time to clear the sub-micron gap of an evanescent field coupler. This problem can be tackled during the design phase of the chip in which an automatic layer generation is used to create additional mesas around the waveguides<sup>4</sup>, as shown in Figure 2.12. These large blocks cover most of the open areas and prevent the decrease of etch rate due to plasma loading. In order to keep the exposure time

<sup>4</sup>Of course extra exposure of mesas is only required for negative tone type resists

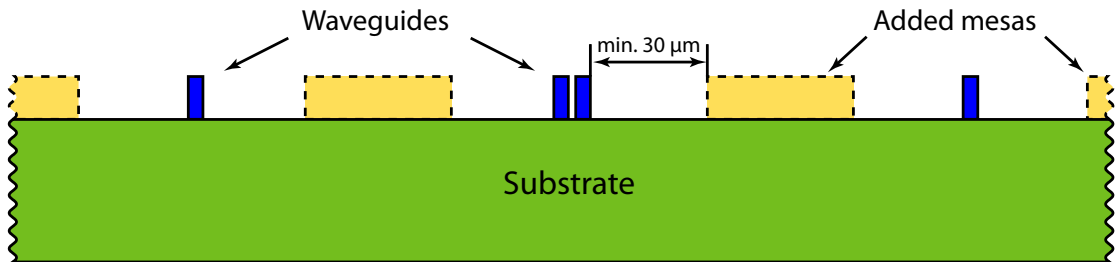


**Figure 2.12:** Schematic of the additional cover mesas for negative tone type resists.

short, a lower resolution and a higher e-beam current must be set for the mesas. As a result of this, the two patterns for the mesas and the waveguides must be fractured separately, which means that the proximity correction of the waveguides does not account for the backscattered electrons of the mesas and vice versa. Overexposure due to proximity problems can be avoided by setting the electron backscattering range ( $\beta=30\ \mu\text{m}$ ) as a design rule for the minimum mesa-waveguide distance. A second advantage of creating mesas is that these provide an additional mechanical support for the stand-alone fragile waveguides.

## 2.4.2 Deep etch

Waveguides with narrow bends support the fundamental guided mode only if the lateral optical confinement is strong. In case of conventional III-V epitaxial laser materials, like the one used in this work, non lossy modes can be guided in curved waveguides with bending radius  $5\ \mu\text{m}$  or above if the etch depth is at least  $1 - 1.5\ \mu\text{m}$  below the active core (details in Section 5.3, p. 71). As the upper cladding thickness is around  $1.5 - 2\ \mu\text{m}$ , a total etch depth larger than  $3 - 3.5\ \mu\text{m}$  is usually required. All the deep etch processes were developed to reach these depths with a  $600\ \text{nm}$  thick HSQ mask in an inductively coupled plasma (ICP) RIE machine. The advantage of ICP systems is that - unlike in conventional RIE machines - plasma density and ion energy are controlled separately. Processes were optimised with the objective of achieving smooth and vertical etching of Al-quaternary materials.

A room temperature,  $\text{Cl}_2/\text{CH}_4/\text{H}_2$  based process was developed with the cooperation of the IOLOS project partners at the University of Bristol. Process parameters are detailed in Table 2.1. The methane added to the chlorine improves the desorption of  $\text{InCl}_x$  by forming by-products with indium, which are volatile at

**Table 2.1:** Summary of deep etch process parameters.

Chemistry	Cl <sub>2</sub> /CH <sub>4</sub> /H <sub>2</sub>	Cl <sub>2</sub> /Ar/N <sub>2</sub>	Cl <sub>2</sub> /Ar/BCl <sub>3</sub>
Gas flow [sccm]	13/10/12	8/6/20	2.6/33/4.4
Pressure [mT]	4	2	2
Coil power [W]	1000	400	750
RF power [W]	160	120	100
Platen temp. [°C]	25	180	180
Etch rate [ $\mu\text{m}/\text{min}$ ]	1.03	0.72	2.33
Mask selectivity <sup>a</sup>	1:9	1:10	1:21
Pro	Room temp.	Verticality	Smoothness
Contra	Mask edge erosion	Sidewall roughness	Undercut

<sup>a</sup>To calculate the selectivity the height of the remaining mask in the center of the waveguide was measured, edge erosion is not interpreted in this ratio.

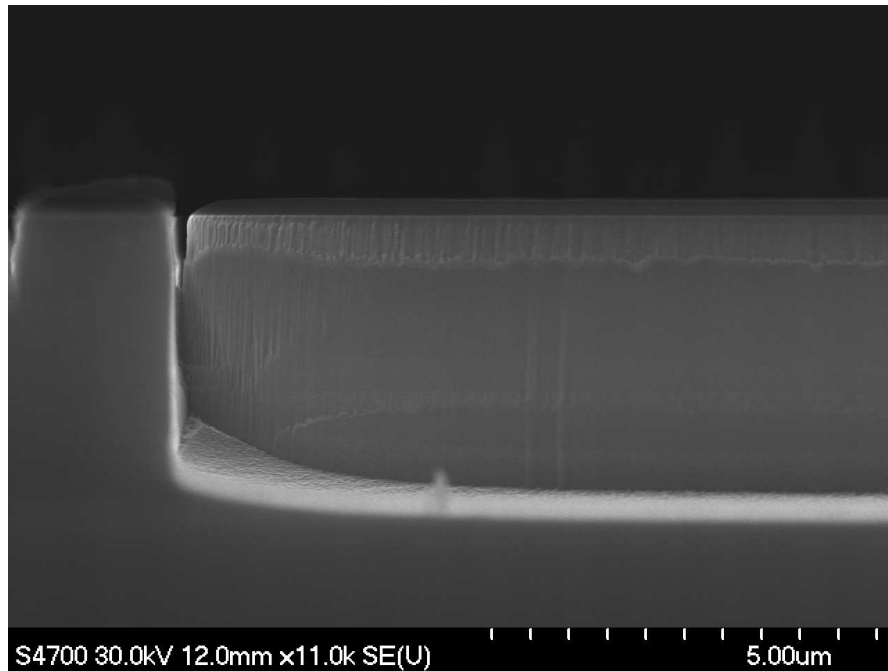


**Figure 2.13:** SEM image of a 200 nm wide evanescent point coupler's cross section. The gap is between a straight and a 20  $\mu\text{m}$  radius circular waveguide.

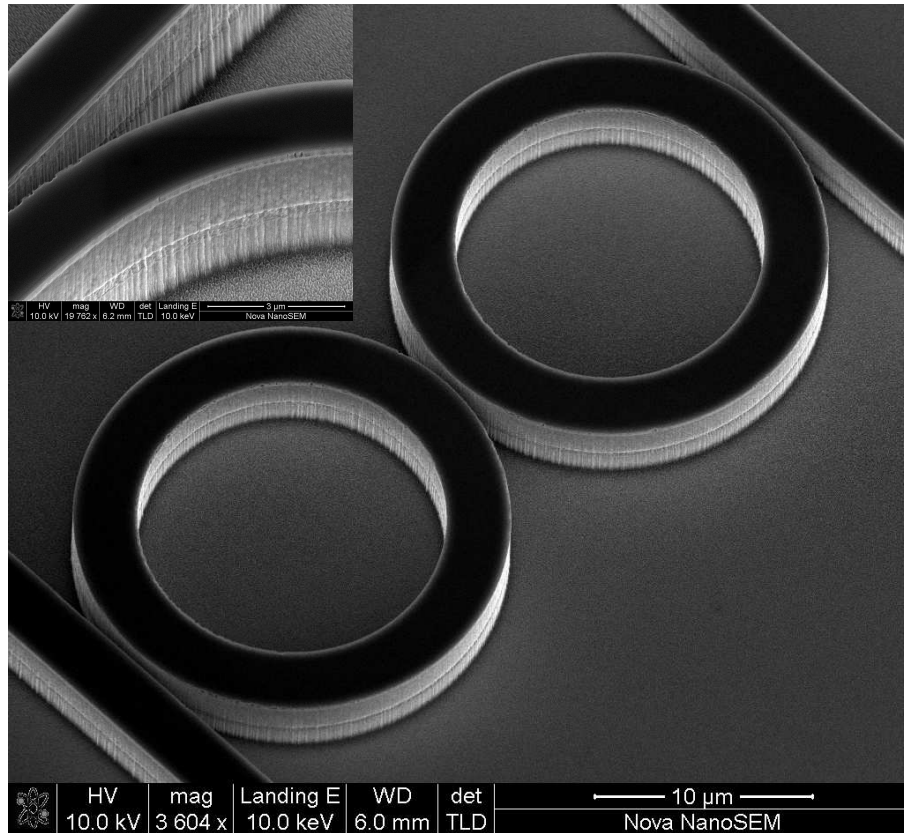


**Figure 2.14:** SEM image of a coupled double micro ring structure. The inset shows a close up of a point coupler. The chips in the mask edge are the first signs of starting mask failure due to edge erosion.

room temperature. Moreover, the hydrocarbons in the chamber form a protecting polymer film that improves the sidewall quality. The excellent smoothness and verticality of the waveguide sides can be observed in Figure 2.13, where only the top part of the waveguide shows an increased roughness due to mask edge erosion (the SEM images reported in [59] show similar features). This problem limits the total etching depth to  $2.7\text{--}2.8\ \mu\text{m}$  with this chemistry. For this reason two, high temperature  $\text{Cl}_2/\text{Ar}$  based processes were investigated to increase the depths to  $3\ \mu\text{m}$  and above [61, 58]. In these approaches  $\text{InCl}_x$  cluster formation is tackled with the use of raised platen/substrate temperature and with the addition of high energy Ar sputtering ions to the plasma.

Verticality of the sidewalls can be controlled by adding nitrogen to the  $\text{Cl}_2/\text{Ar}$

chemistry. The effect of the  $N_2/Cl_2$  ratio on the anisotropy of the process was investigated<sup>5</sup> [66] and it was found that etches with a low  $N_2/Cl_2$  ratio have high etch rates and good selectivity but, because of the high lateral etching, the waveguide profiles are undercut. The passivating/inhibiting effect of the  $N_2$  can be improved by increasing its content with the result that the etch becomes more anisotropic, the etch rate and the selectivity decrease and the sidewalls become less rough. Almost vertical sidewalls can be produced with flow ratios in the range of 2 to 3. Figure 2.14 shows two coupled micro rings etched with a  $N_2/Cl_2$  ratio of 2.5, that guarantees a good trade-off between reasonable smoothness (see inset of Figure 2.14) and good mask selectivity. A remarkable property of this chemistry is that the etch rate of small gaps normalised to that of the large area is independent of the  $N_2$  content (see Figure 2.15.a). Moreover the comparison of RIE lag data from over a year span shows that the change of etch rate in this period was negligible. Thanks to such a process robustness, the depth of sub-micron gaps can be designed and fabricated with a  $\pm 50$  nm accuracy by closely monitoring the etch depth of large areas (it is easy and accurate to measure the depth of large openings with a surface profile meter). Although this dry etch process proved satisfactory in terms of etch rate and mask selectivity, the sidewall roughness is quite substantial. For this reason a second approach for the sidewall passivation was investigated by adding  $BCl_3$  to the  $Cl_2/Ar$  chemistry [58]. Process parameters used for the etching of anisotropic AlInGaP features were used as a baseline recipe [67], and a study on the effect of the pressure (2-10 mT), coil power (500-1000 W) and RF power (75-125 W) was carried out. Highly undercut and rough sidewall profiles can be observed for high pressure values while the reduction of the pressure level to 2 mT results in less chemical etch components and so the sidewalls become more anisotropic and smooth. Medium coil power values of 750 W form a good compromise between the poor selectivity at low values and the strong undercut of the dense plasma. At low RF power levels the physical etch components are weak and the resulting etch is isotropic and sidewalls become sloped. Based on the feedback from the optimisation runs the process parameters shown in Table 2.1 were selected to be used for the final devices. Figure 2.16 shows a  $7 \mu m$  diameter micro disk etched with the  $Cl_2/Ar/BCl_3$  chemistry. The eye catching smoothness of the sidewall is due to the passivating effect of the added  $BCl_3$  (also illustrated in the inset of Figure 2.16).

---

<sup>5</sup>Dry etch test were carried out with the collaboration of Rafal Dylewicz.

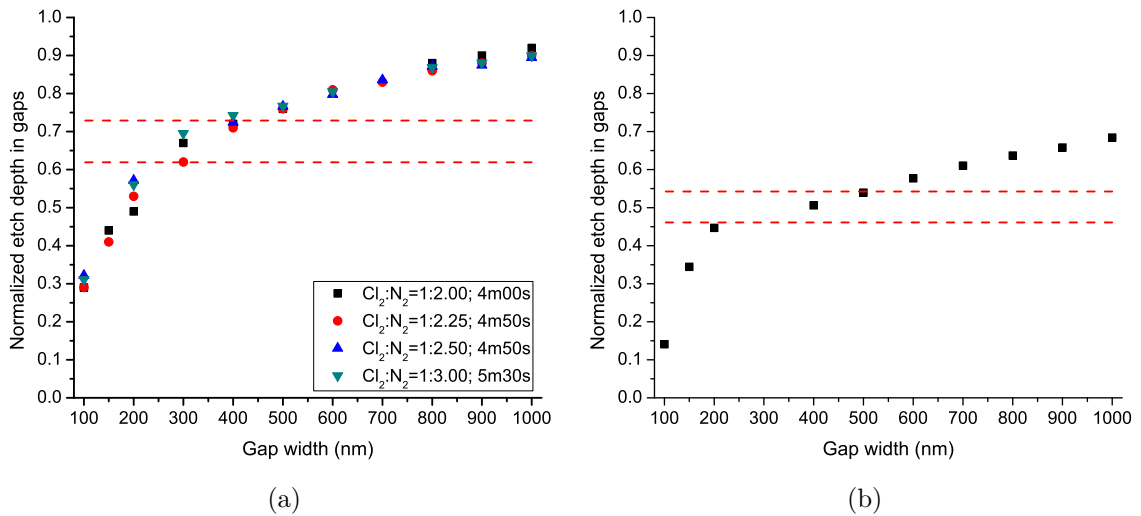


**Figure 2.15:** Measured RIE lag data of the Cl<sub>2</sub>/Ar/N<sub>2</sub> (a) and the Cl<sub>2</sub>/Ar/BCl<sub>3</sub> (b) chemistry. The data sets were normalised to the large area etch depth. Dashed horizontal lines indicate the top and bottom of the material core. In (a) the time and the Cl<sub>2</sub>/N<sub>2</sub> ratio of the etch is given in the legend.

SEM inspections of cleaved waveguide cross sections indicate that the profile has a slight, 200 nm undercut, which makes this process unsuitable to etch first order optical gratings. During the profile inspection the etch depth of gaps of different width was recorded and is plotted in Figure 2.15.b. The really high selectivity of this etch (see Table 2.1) provides an excellent solution to produce 4-5  $\mu\text{m}$  deep features with thin dielectric masks.

It is worth noting that neither of the described processes is superior to the others. Each has its own strengths and weaknesses; however, together, they form an excellent toolkit, which offers the designer a number of alternatives.

## 2.5 Dielectric quasi-planarisation and metallisation

The two common and widely used methods for metal deposition are evaporation and sputtering. Thermal or electron beam evaporation produces a diverging cone of particles diffusing away from the source. Here, a simple technique called “rocking”

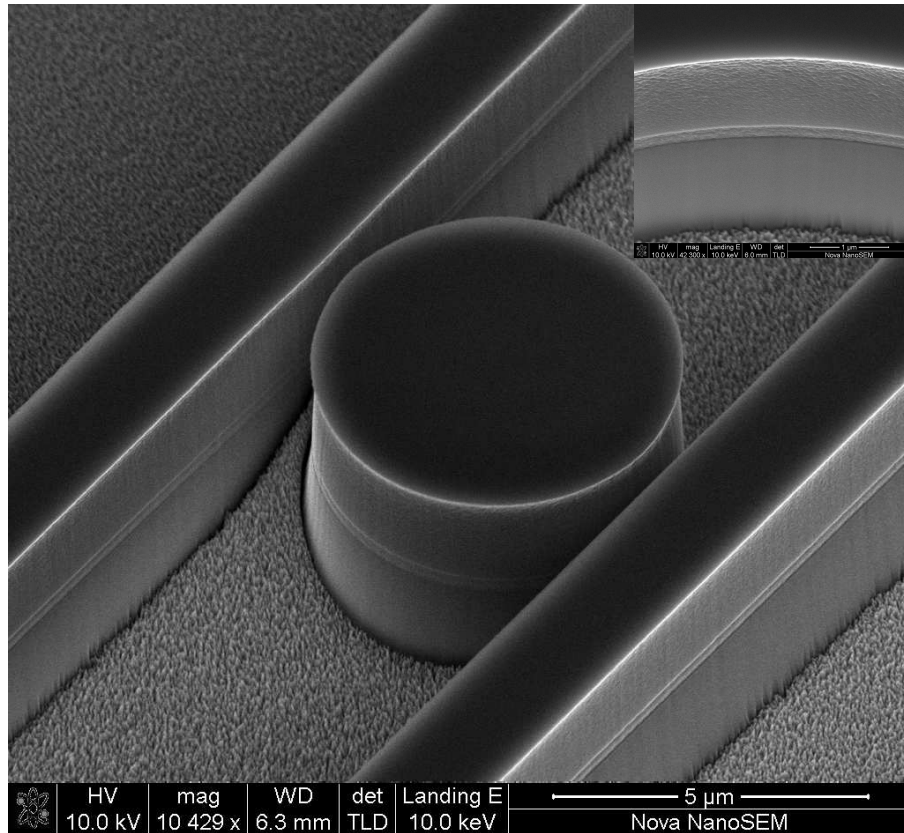


**Figure 2.16:** SEM image of a  $5\ \mu\text{m}$  radius deep etched micro disk. The inset shows a close up of a ring's sidewall.

is used to coat shadowed or vertical sidewalls, where the sample is tilted with respect to the source. Curved waveguides are more problematic to coat with this technique, since at least four tilts are required to ensure a uniform coating. In a sputter deposition chamber, the randomly moving ions of the plasma bombard the target plate. The physically sputtered atoms fly in a straight line to the substrate and are deposited there, forming an isotropic film since shadowed areas and vertical sides are well covered by the ballistic particle flow. This advantage, however, can turn into a disadvantage: also the shadowed sidewalls of a lift-off resist are coated and a continuous metallic film may be deposited over the whole sample, thus preventing the lift-off to form the contact pads.

Figure 2.17(a) shows a shallow etched waveguide, which was first evaporated with 30 nm Ti/60 nm Pt/240 nm Au and then covered by a sputtered 250 nm Au

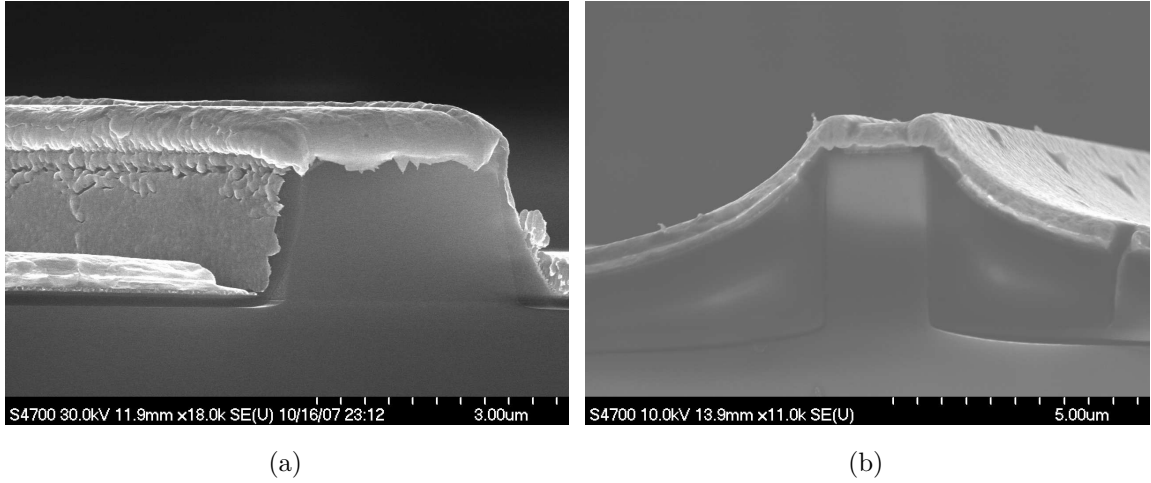


**Figure 2.17:** (a) SEM image of a  $2\ \mu\text{m}$  deep etched waveguide’s facet. Evidence of poor metallisation can be seen on the sidewalls. (b) Planarized and then metal coated output waveguide of a SRL.

layer to coat the vertical surfaces. On the sidewalls the low uniformity of the sputtered Au layer can be observed, which becomes particularly thin at the waveguide “necks”. These weak points of the gold metallisation tend to fuse when high current density is applied during the device testing. Both the nonuniform metal sidewalls and the lift off problems can be tackled indirectly by quasi-planarizing the sample surface. Before metal evaporation the standard 200 nm dielectric isolation layer is supplemented with a 400 - 450 nm layer of spin on dielectric - HSQ - and this is topped with a 75 nm thick plasma enhanced chemical vapor deposition (PECVD) silica layer. The resulting declivity of such a stack is shown on Figure 2.17(b). Good and thick coverage of the evaporated metal can be observed on the top of the waveguides, on the dielectric slopes, in the trenches and on the supporting mesas.

The specific contact resistance ( $r_c$ ) of the Ti/Pt/Au p-type metallisation was evaluated by the transfer length method (TLM) [68]. The metal stack  $r_c$  with a  $\text{Ga}_{0.47}\text{In}_{0.53}\text{As}$  cap layer was measured to be around  $7 \times 10^{-6}\ \Omega\text{cm}^2$ . To assess the quality of the metallisation, the series resistance ( $r_s$ ) of similar sized SRLs was measured throughout an entire chip: 96 % of the fifty devices had a series resistance in the range of 3 to 5 Ohm, which results indicate that the process is robust and it has a good uniformity.

Electrical driving of laser diodes is usually realised in a common cathode configuration, where the p-type contact of each individual laser requires electrical isolation and the n-type contact is the backplane of the chip. Deep etched structures offer the possibility to form the n-type contact at the bottom of the trenches, which can be used for example as the grounding point for coplanar waveguides. Rectangles of the size  $300 \times 500 \mu\text{m}$  were fabricated at the bottom of the deep etched trenches and on the top of the mesas to assess the resistance characteristic of deep etched n-type ohmic contacts. The standard p-type Ti/Pt/Au stack was used for metallisation, because in this way both p- and n-type contacts can be fabricated with one lift-off step. Compared to the Au/Ge/Au/Ni/Au eutectic backplane contacts, the average area specific resistance increases by  $1.65 \times 10^{-3} \Omega\text{cm}^2$  ( $\sim 1 \Omega$  higher). The large increase of the area specific resistance makes this n-type contact impractical to use, even though a single lift-off step would make the fabrication of deep etched devices simple. As high speed contacts are out of the scope of this work this issue was not pursued further.

## 2.6 Chapter summary

In this chapter a brief overview of the fabrication flow of SRLs was given. Thereafter the key processes, which were newly developed or where major improvement was carried out, were detailed. The performance of both positive (PMMA) and negative (HSQ) tone type resists was evaluated. In case of HSQ, the emphasis of the process development was on ensuring smooth resist sidewalls and on the ability of opening 100 nm gaps between two parallel running waveguides. The latter required the careful optimisation of proximity correction for e-beam lithography. A further advantage of the application of this correction technique is that it offers the designer peace of mind as the different clear-out doses of various patterns is automatically corrected during pattern fracturing.

Next, the dry etching techniques utilized in this work were discussed. In case of shallow etched devices the already existing  $\text{CH}_4/\text{H}_2/\text{O}_2$  recipe was evaluated. Dry etch tests revealed that the etch rate of the recipe drops with an increased local loading of the plasma, which means that depending on the masked area of the chip the etch rate varies. A solution proposed for keeping the etch rate stable is to automatically generate separation trenches with the layout CAD tool during

design and so to cover most of the chip area with resist.

The fabrication of small radius waveguides that support the fundamental guided mode, requires 3-3.5  $\mu\text{m}$  deep etched waveguides. In order to reach such etch depths different inductively coupled plasma–RIE chemistries were developed and evaluated. During the dry etch tests special attention was paid on two features: sidewall verticality and smoothness. First, a room temperature  $\text{CH}_4/\text{H}_2/\text{Cl}_2$  chemistry was investigated but the strong mask edge erosion limited the maximum etching depth to 2.7  $\mu\text{m}$ . For this reason alternative high temperature  $\text{Cl}_2/\text{Ar}$  based chemistries were developed and evaluated. Excellent sidewall verticality and acceptable sidewall roughness was achieved by adding  $\text{N}_2$  to the base chemistry and a further improvement of the sidewall smoothness was achieved by replacing  $\text{N}_2$  with  $\text{BCl}_3$ . A drawback of the currently developed  $\text{BCl}_3$  process is the slightly over chemical etching profile, which results in a  $\sim 200$  nm under cut waveguide profile in case of a 4.5  $\mu\text{m}$  etch. The sidewall verticality of the  $\text{Cl}_2/\text{Ar}/\text{BCl}_3$  process can be improved with additional process development.

Finally, the properties of the developed dielectric quasi-planarisation were discussed and the p- and n-type metallisations were briefly described.

# Chapter 3

## Material properties

In this chapter the properties of the material used for this work are discussed. First, a brief overview of the epitaxial layer structure is given, then the phenomenological equations that describe the material are detailed. By combining the theory and experimental data the main material parameters are derived. The last part of the chapter investigates the capability of the material for laser size reduction.

### 3.1 Material design

All the fabricated devices in this thesis are based on a commercially available<sup>1</sup>, compressive strained, multiple quantum well (MQW) structure. Table 3.1 shows the simplified layer structure of the epitaxial wafer. Above and below the five quantum wells, two 60 nm thick, graded refractive index layers are used to assure better optical confinement. These are sandwiched by two wide band-gap layers, which prevent electrons and holes from escaping the quantum well (QW) region. Theoretical and experimental studies show that the conduction band offset of AlGaInAs/InP materials ( $\Delta E_c=0.72\Delta E_g$ ) is larger compared to that of the traditional InGaAsP/InP materials ( $\Delta E_c=0.4\Delta E_g$ ). As a result, devices based on Al-quaternary materials have a lower carrier leakage and a higher characteristic temperature [69, 70, 71]. The characterisation of the basic material parameters allows the assessment of wafer quality and aids the designer to estimate device performance. Usually the very first and most fundamental measured property of a semiconductor laser is the

---

<sup>1</sup>IQE Ltd. - [www.iqep.com](http://www.iqep.com)

**Table 3.1:** Epitaxial layer structure of the wafer. IQE part number: IEGENS-13-17.

Thickness	Material	Layer	Strain	Dopant	Refr. index
200 nm	Ga <sub>0.47</sub> In <sub>0.53</sub> As	Cap layer		Zinc	3.646
50 nm	Ga <sub>0.29</sub> In <sub>0.71</sub> As <sub>0.62</sub> P <sub>0.38</sub>	Lattice match		Zinc	3.470
1600 nm	InP	Upper cladding		Zinc	3.146
20 nm	Ga <sub>0.15</sub> In <sub>0.85</sub> As <sub>0.33</sub> P <sub>0.67</sub>	Wet etch stop		Zinc	3.310
50 nm	InP	Transition layer		Zinc	3.146
60 nm	Al <sub>0.42</sub> Ga <sub>0.05</sub> In <sub>0.53</sub> As	Electron conf.		Zinc	3.279
60 nm	Al <sub>0.34</sub> Ga <sub>0.13</sub> In <sub>0.53</sub> As	GRIN		-	3.328
10 nm	Al <sub>0.22</sub> Ga <sub>0.29</sub> In <sub>0.49</sub> As	Barrier	-0.3 %	-	3.389
5×6 nm	Al <sub>0.07</sub> Ga <sub>0.22</sub> In <sub>0.71</sub> As	QW	1.2 %	-	3.553
5×10 nm	Al <sub>0.22</sub> Ga <sub>0.29</sub> In <sub>0.49</sub> As	Barrier	-0.3 %	-	3.389
60 nm	Al <sub>0.34</sub> Ga <sub>0.13</sub> In <sub>0.53</sub> As	GRIN		-	3.328
60 nm	Al <sub>0.42</sub> Ga <sub>0.05</sub> In <sub>0.53</sub> As	Electron conf.		Silicon	3.279
~ 350 μm	InP	Substrate		Silicon	3.146

optical power – current (P – I) characteristic. From this curve the threshold current ( $I_{th}$ ) of a device can be determined and from the slope the differential quantum efficiency can be calculated:

$$\eta_d = \frac{q}{h\nu} \frac{dP}{dI}, \quad (3.1)$$

where  $q$  is the charge of the electron,  $h$  is the Planck constant,  $\nu$  is the optical frequency of the laser light. Internal device parameters, like the quantum efficiency ( $\eta_i$ ) and the net internal loss  $\alpha_i$ , cannot be extracted from a single laser. Usually these parameters are determined from lasers of different cavity lengths. From the P – I plots, the  $\eta_d$  values for each device length can be derived and then this data is fitted to the following equation [72]:

$$\frac{1}{\eta_d} = \frac{\alpha_i}{\eta_i \ln(1/R)} L + \frac{1}{\eta_i}, \quad (3.2)$$

where  $L$  is the total device length and  $R=(R_1R_2)^{0.5}$  is the mean mirror reflectivity of the two facets<sup>2</sup>. The plot  $1/\eta_d$  versus  $L$  forms a straight line, which intersects the y-axis at the value  $1/\eta_i$ . From this intersect and from the slope of the fitted

<sup>2</sup>Facet reflection was calculated using the Fresnel-equations.

line one can calculate  $\alpha_i$ . Once the internal losses of the cavity are known, the gain of the material can be calculated, since at threshold it is equal to the total losses of the cavity. More specifically:

$$n_w \Gamma g_{th} = \alpha_i + \alpha_m = \alpha_i + \frac{1}{L} \ln \left( \frac{1}{R} \right), \quad (3.3)$$

where  $n_w$  is the number of quantum wells,  $\Gamma$  is the optical confinement factor of one well,  $\alpha_m$  is the net mirror loss and  $g_{th}$  is the material gain per quantum well at threshold (the  $g_m = n_w \Gamma g_{th}$  product is called the modal gain). In the case of narrow or strained QWs the relation of gain and current density can be approximated with a logarithmic function [72, 73]:

$$g = g_0 \ln \left( \frac{J}{J_0} \right) + 1, \quad (3.4)$$

where  $J_0$  and  $g_0$  are fitting parameters and denote the point where the  $g/J$  is maximum, i.e. the optimum operation point on the gain curve. This knee of the gain curve can be found graphically by drawing a tangent line through the origin, or if there is not enough experimental data available then the value of  $J_0$  and  $g_0$  can be calculated from the equations 3.2, 3.3 and 3.4. The combination of these yields:

$$\ln(J_{th}) = \ln \left( \frac{J_0}{e} \right) + \frac{\alpha_i}{n_w \Gamma g_0} - \frac{1}{L} \frac{\ln(R)}{n_w \Gamma g_0}, \quad (3.5)$$

where the slope of  $\ln(J_{th})$  versus  $1/L$  plot gives  $1/g_0$ . The first two terms on the right hand side are constant as a function of the length and denote the case when the mirror losses of the laser are negligible, i.e. the theoretical threshold current density of an infinitely long cavity ( $J_\infty$ ).

Usually, material parameters are acquired experimentally from the P–I characteristics of broad area lasers (BALs). The lateral current spreading and current leakage of these gain guided lasers can be neglected and only material imperfections contribute to the internal losses of the device. In order to incorporate the waveguide propagation losses, the extraction of  $\eta_i$  and  $\alpha_i$  was performed on a set of 2  $\mu\text{m}$  wide half ring lasers. Figure 3.1 plots the schematic of three different length half ring lasers. This geometry takes longer to fabricate, but with proper design all

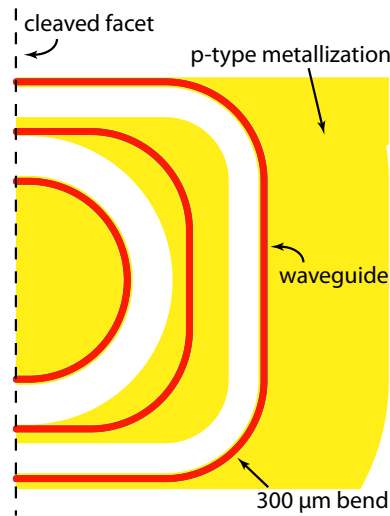


**Figure 3.1:** Layout design of different length half ring lasers.

of the required lengths can be produced with a single cleave. In order to minimize the effect of curvature losses all the devices have a bending radius of  $300\ \mu\text{m}$ .

The material parameters extracted from the P–I curves of the ridge waveguide half ring lasers can be seen in Table 3.2. Compared to the BAL data, as expected, the  $g_0$  value is lower and  $J_\infty$  is higher. The reason for this lies in the greater losses of the ridge waveguide and in the increased junction heating of the half ring lasers, as these were tested using a direct current (DC) sweep, while the BALs were measured with current pulses. Figure 3.2(a) reports the modal gain of the material as a function of the current density. On the graph, the curve tangent through the origin is drawn with a dashed line and the optimum operating point is marked with a black cross. Around the optimum operation point  $(J_0, g_0)$  the gradient of the curve is small. As a consequence, a relatively wide range of threshold gain values can be used without having a significant penalty on the device threshold current. An easy way to determine the design tolerance is to plot  $J/g$  as function of  $g$ , as shown in Figure 3.2(b). Modal gain values in the range of 29 to 97 (below the dashed, horizontal red line) do not deviate more than 20% from the optimum  $J/g$  value. If the mirror losses of the cavity are known, then the cavity lengths corresponding to these gain values can be calculated by rearranging Equation 3.3. For example, a FP cavity with cleaved facets ( $R \simeq 0.3$ ) of lengths from 0.15 mm to 1 mm would be in the 20% interval of the optimum operating point. If we now

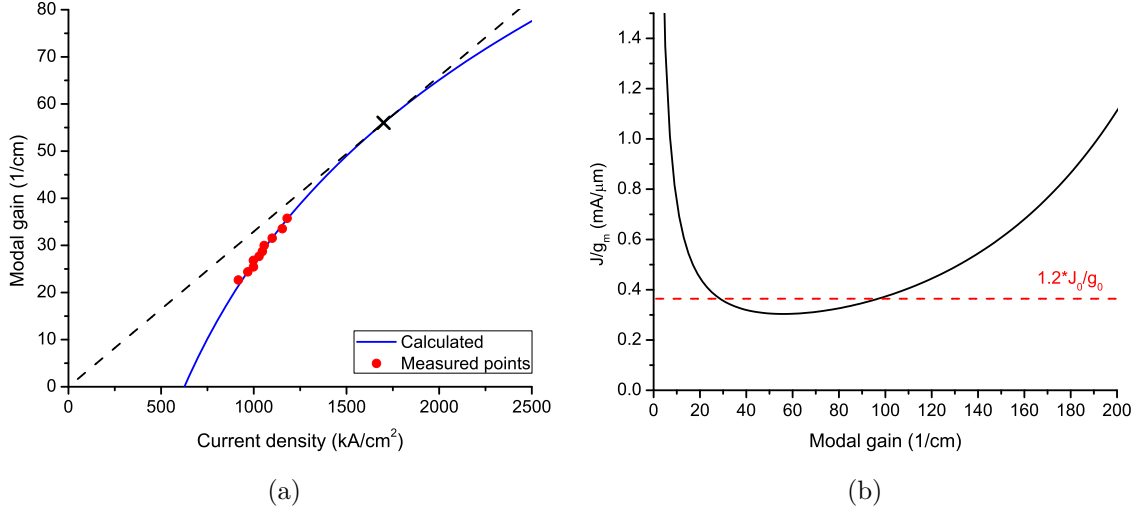


**Figure 3.2:** (a) Calculated modal gain versus current density plot of the IEGENS-13-17 material. Measured data of the half ring lasers is plotted with red dots. (b) Current density over modal gain plotted as function of the modal gain. This plot illustrates clearly the problem of operating too far into saturation or near to transparency.

**Table 3.2:** Measured material parameters of the IEGENS-13-17 wafer. The very small number of fabricated BALs prevented the extraction of all parameters.

	$\eta_{int}$	$\alpha_i$ [cm <sup>-1</sup> ]	$J_\infty$ [A/cm <sup>2</sup> ]	$J_0$ [A/cm <sup>2</sup> ]	$n_w \Gamma g_0$ [cm <sup>-1</sup> ]
BAL	-	-	530	-	65
Ridge wg.	0.91	18.4	830	1700	56

consider a laser cavity with an average reflection of 0.9 as a second example (an SRL with a weak coupler or a FP laser with strong Bragg reflectors), the 20% optimum operation interval of such a device lies between a cavity length range of 13 μm to 88 μm.

## 3.2 Threshold current analysis

The next and final step is to assess whether this material is good enough to fabricate micro-sized ring or disk lasers. This can be answered through the equations derived by McIlroy and Kurobe for MQW structures [73, 74].

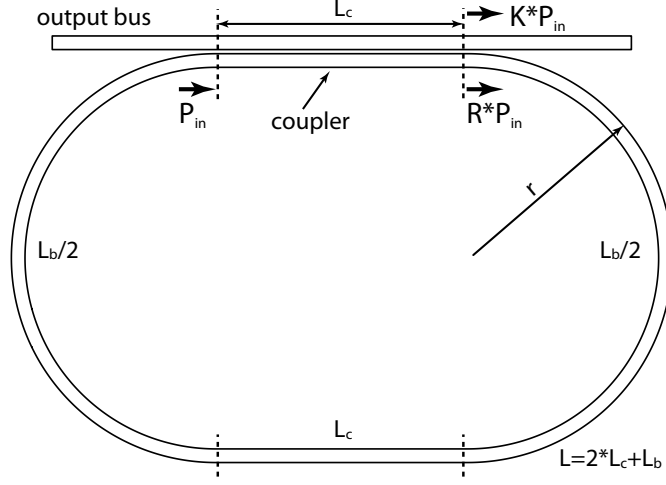


**Figure 3.3:** Schematic of a racetrack shape semiconductor ring laser.

**Table 3.3:** Values substituted into Eq. 3.6 to calculate the threshold current as a function of ring radius with out-coupling as a parameter.

$W$	$\alpha_i$ [ $\text{cm}^{-1}$ ]	$J_0$ [ $\text{A}/\text{cm}^2$ ]	$n_w \Gamma g_0$ [ $\text{cm}^{-1}$ ]
$1 \mu\text{m}$	18.4	1700	56

Figure 3.3 plots the schematic of a racetrack shape SRL which threshold current can be approximated by:

$$I_{th} \simeq J_0 W L \exp \left( \frac{\frac{L_b}{L} \alpha_b(r) + \alpha_i - \frac{1}{L} \ln(R)}{n_w \Gamma g_0} - 1 \right), \quad (3.6)$$

where  $W$  is the waveguide width and  $L$  is the length of the cavity,  $r$  is the radius of the curved section,  $\alpha_b$  is the bending loss and  $L_b$  is the length of the curved part. The variables used for calculating  $I_{th}$  of various length SRLs are the experimentally extracted material properties and are summarised in Table 3.3. It is assumed here that the  $\alpha_b$  of deep etched curves is negligible down to a few microns radius and that  $\alpha_i$  is comparable to that of shallow etched devices (this assumption is confirmed in Chap. 5). On Figure 3.4 the  $I_{th}$  of a  $W=1 \mu\text{m}$  wide SRL is plotted as a function of the device radius with out-coupling ( $K=1-R$ ) as a parameter. Each curve follows a similar trend as the device length decreases. Long cavities are dominated by internal losses. In this case the  $I_{th}$  of the SRL decreases proportionally with

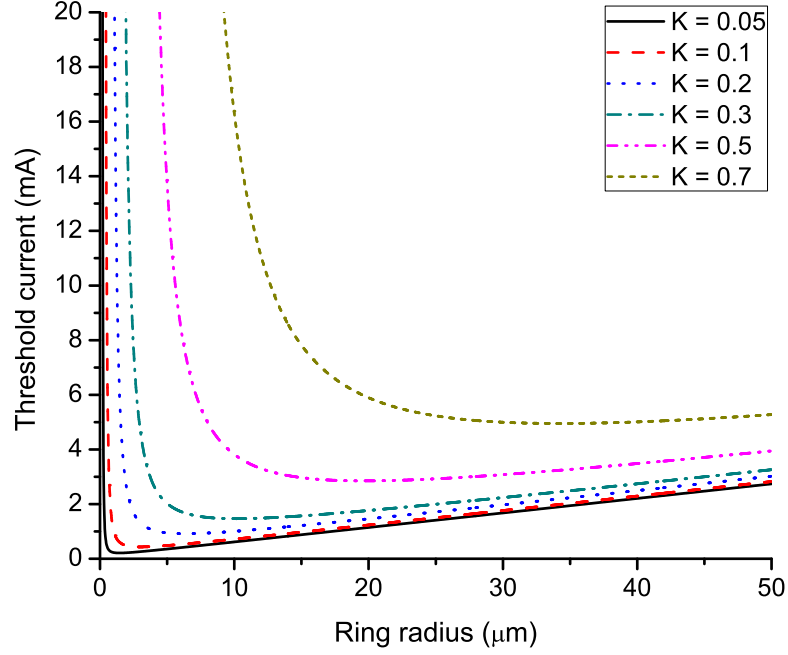


**Figure 3.4:** Calculated threshold current as a function of the radius of a ring cavity. Waveguide width is  $1 \mu\text{m}$ . During the calculations it was assumed that bending losses are negligible.

the radius since  $L\alpha_i \gg \ln(1/R)$ . After reaching a minimum point, the so called optimum length ( $L_{opt}$ ), the threshold increases exponentially as the mirror/coupler losses overtake the other losses ( $L\alpha_i \ll \ln(1/R)$ ). The SRL radius, for which the current threshold is minimum depends strongly on the out-coupled power. Devices with up to 20% output coupling can lase down to a radius of 3-4  $\mu\text{m}$  without having a noticeable increase of the  $I_{th}$ . Couplers stronger than 20% prevent the lasing of small diameter devices. Finally, it can be concluded that if there are no significant loss factors apart from  $\alpha_i$  and  $\alpha_m$  then the strong gain of the 5 QWs of this material is sufficient to support lasing in micro-sized SRLs down to a radius of 3-4  $\mu\text{m}$ . The significant issue of the additional bending losses will be dealt with in Chapter 4 and Chapter 5.

### 3.3 Chapter summary

In this chapter the fundamental properties of the used lasing material were discussed. First, the epitaxial layer structure of the material was described, then the phenomenological equations that model the performance of the material were reviewed. Evaluation of the measured P–I characteristics of different length broad area laser and half ring laser devices allowed the determination of the most common material parameters, such as internal losses of the waveguide ( $\alpha_i$ ), internal efficiency ( $\eta_i$ ), optimum modal gain of the QWs ( $g_0$ ) and the corresponding current density ( $J_0$ ).

In the second part of the chapter, based on the calculated material parameters, the current threshold dependence of the SRL was analyzed as a function of the device size. It was found that in case of moderate output coupling (up to  $\sim 20\%$ ) the size of SRLs can be reduced down to a radius of 3-4  $\mu\text{m}$  without a significant penalty of the threshold current density. Based on this it can be concluded that the 5 QW Al-quaternary material has enough gain to support lasing in micron-sized SRL devices.

# Chapter 4

## Shallow etched device design

This chapter details the design considerations of shallow etched waveguide SRLs. The key requirements of such a cavity are: single transverse mode operation and minimal bending losses for low threshold current lasing, and low back-reflection couplers for robust unidirectional operation. Each of these design aspects are thoroughly investigated via simulations and experiments. The back-reflection reduction of the outputs facets is also discussed as low feedback from these points promotes the robustness of unidirectional operation. The final part of the chapter details the properties of SRL devices that were fabricated based on the previously discussed design considerations.

### 4.1 Waveguide design

In Section 2.4.1 it was shown that the high etch selectivity of the  $\text{CH}_4/\text{H}_2/\text{O}_2$  chemistry allows the waveguide etching to stop accurately on the top of the core of the material. In such a waveguide the effective refractive index difference ( $\Delta n_{eff}$ ) of the etched and non etched areas confines the light horizontally, while the vertical confinement comes from the core-cladding refractive index difference. Figure 4.1(a) shows the supported fundamental transverse electric (TE) mode of a  $2\ \mu\text{m}$  wide and  $1.92\ \mu\text{m}$  deep slab. Due to the weak horizontal confinement ( $\Delta n_{eff} < 0.1$ ) the optical mode is particularly sensitive to bending losses. On the other hand, the shallow etch is advantageous if one wants to keep sidewall recombination minimal. Furthermore, as the etch does not penetrate into the core, the sidewall roughness

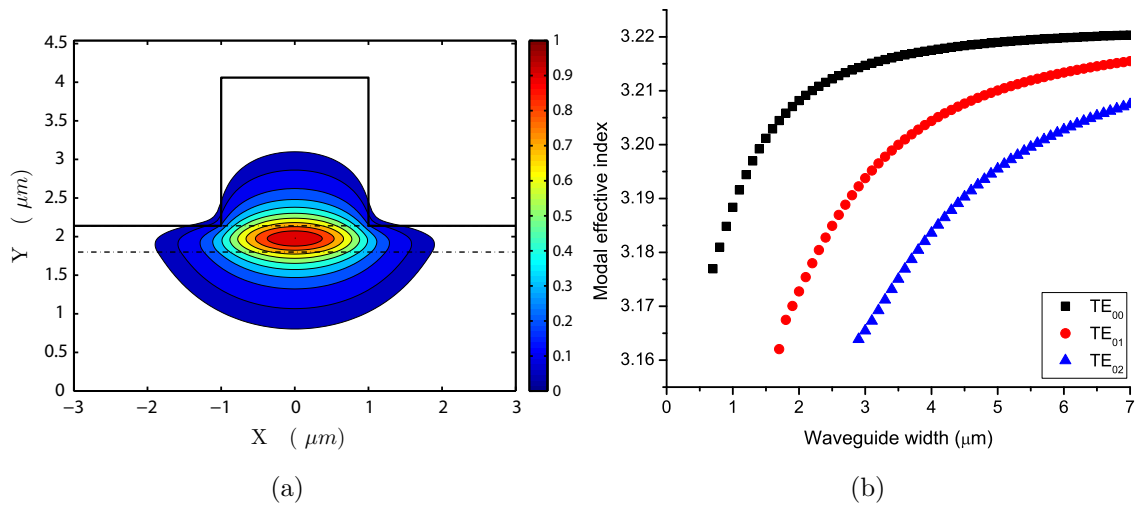


**Figure 4.1:** (a) Contour map of the TE<sub>00</sub> mode of a shallow etched waveguide. The dashed lines indicate the active core of the material. (b) Simulated modal effective index of the first three TE modes as a function of the waveguide width.

induced back-reflections can be neglected. This is beneficial as feedback affects the directional bi-stability of SRLs [20, 75].

Low bending losses and single transverse mode propagation are the main requirements of a SRL cavity geometry. To determine the optimal waveguide widths, 3D beam propagation method (BPM) simulations were carried out with a commercially available design software<sup>1</sup>. First, the effective modal index values of the first three TE modes versus the width of a straight waveguide were calculated (see Figure 4.1(b)). The results indicate that the dielectric waveguide does not support any modes below the width of 0.7-0.8 μm, and the first order mode cuts off at around 1.5 μm. This width should be preferable for single mode operation as the substrate losses of the TE<sub>00</sub> mode increase as the waveguide becomes narrower.

A second aspect to be considered is that the mode of a curved waveguide should have negligible evanescent losses. Bending losses versus the radius of curvature were simulated using 3D BPM<sup>2</sup> with the waveguide width as a parameter, as shown in

<sup>1</sup>RSoft Design Group, Inc. - [www.rsoftdesign.com](http://www.rsoftdesign.com)

<sup>2</sup>The conventional BPM is not capable of simulating curved waveguides due to paraxiality limitations. However, the conformal index mapping technique extends the method's capability to handle tight bends.

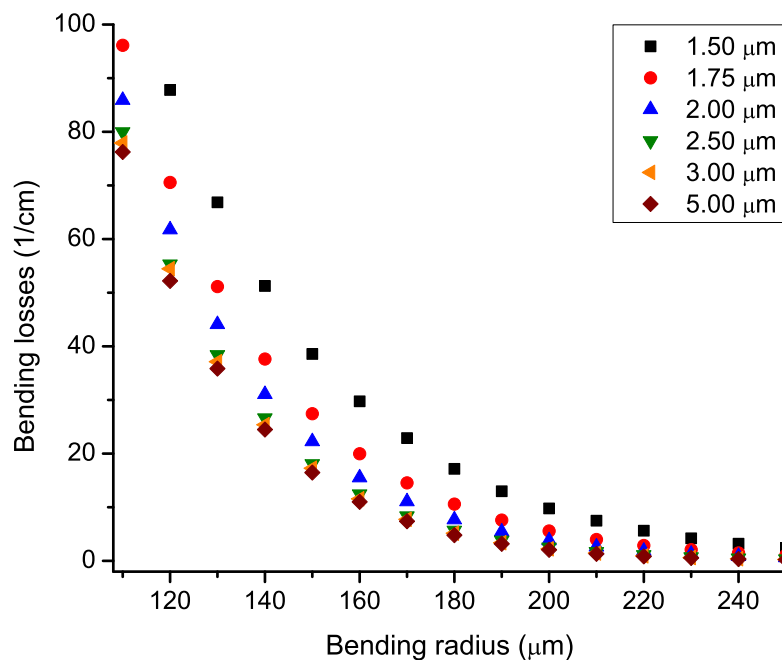


**Figure 4.2:** Simulated bending losses as a function of the bend radius. The parameter is the width of the shallow etched and curved waveguide.

Figure 4.2. It can be clearly seen that narrower waveguides suffer from stronger bending losses. Ideally, 3-5  $\mu\text{m}$  wide guides should be used to minimise losses due to curvature; however, straight waveguides of such a width support higher order transverse modes and in a strongly pumped racetrack cavity these modes can reach the lasing threshold. To avoid this, a compromise of 2  $\mu\text{m}$  width was used in the shallow etched device designs. At this trade-off width, the bending losses do not increase considerably and the first order mode of a straight waveguide is ten times more lossy than the fundamental one. The bending loss of a 2  $\mu\text{m}$  wide waveguide increases exponentially with decreasing radius and reaches the material loss level ( $\alpha_{mat} \approx 4 \text{ cm}^{-1}$ ) around the radius of 200  $\mu\text{m}$  and  $\alpha_i$  at around 150  $\mu\text{m}$ . Simulations indicate that SRL devices of this geometry can lase down to a radius of 130-120  $\mu\text{m}$ , below this value the losses overtake the modal gain. Measurements on SRLs and half ring lasers confirm the simulations: the smallest lasing devices found have a radius of 120  $\mu\text{m}$  [52]. However, the performance penalty of  $J_{th}$  and  $\eta_d$  due to bending losses makes it impractical to fabricate devices with a radius smaller than 150  $\mu\text{m}$ .

## 4.2 “Semi-shallow” waveguides

The low etch rate of the  $\text{CH}_4/\text{H}_2/\text{O}_2$  chemistry in the Al containing layers can be used to stop very accurately near the top of the QWs. On one hand such a slow, 1-2 nm/min etch rate is advantageous as a few minute miscalculation of the etch time results only in a  $\pm 10$  nm inaccuracy of the etch depth. On the other hand the total device etch time is greatly increased. Calculations show that  $\Delta n_{eff}$  increases significantly when the etch penetrates the confinement layers and stops near to the top of the QWs. 3D BPM simulations were performed to investigate how this affects the net losses of a curved waveguide as a function of the waveguide depth. Results, plotted in Figure 4.3(a), show a clear trend of decreasing losses with increasing depth. Waveguides, where the etch is stopped at around 80-100 nm below the top of the core (see dashed line in Figure 4.3(c)), have low bending losses down to a radius of  $100 \mu\text{m}$ .

Half ring lasers with different values of radius were fabricated in order to confirm the simulations. Each half ring consisted of a  $180^\circ$  bend and two  $100 \mu\text{m}$  long straight waveguides that were  $2 \mu\text{m}$  wide. Devices were etched with the  $\text{CH}_4/\text{H}_2/\text{O}_2$  chemistry for 79 minutes, which results in a total etch depth of around 2010 nm (90 nm below the core top). P-I and V-I characteristics of the devices were recorded and evaluated, and the extracted  $J_{th}$  and area specific resistance ( $r_a$ ) data are plotted as a function of the half ring radius in Figure 4.3(b). The trend of  $J_{th}$  is in a good agreement with the simulations since it increases slowly down to  $100 \mu\text{m}$  radius. Below that value  $J_{th}$  shoots up abruptly as bending dominates the cavity losses. Large radius devices have an unusual, around two times higher,  $J_{th}$  than expected. Most likely, this is due to the high area specific resistance of the devices. The extrapolated  $r_a$  for zero length is  $7.3 \times 10^{-4} \Omega\text{cm}^2$ , which is more than an order of magnitude higher than previously measured specific contact resistances. One possible explanation for the increase of the waveguide resistivity is that during the etch, the  $\text{H}_2$  diffuses into the lattice, passivates the Zn acceptor ions and so the p-type conductivity is reduced [76]. This theory is also supported by the fact that on the same chip, the  $r_a$  of other shallower etched devices, which were masked after 54 minutes of etching, did not increase.

“Semi-shallow” waveguides provide an easy solution to further decrease the size of the SRLs down to a radius of  $100 \mu\text{m}$ . These devices are too large to be called

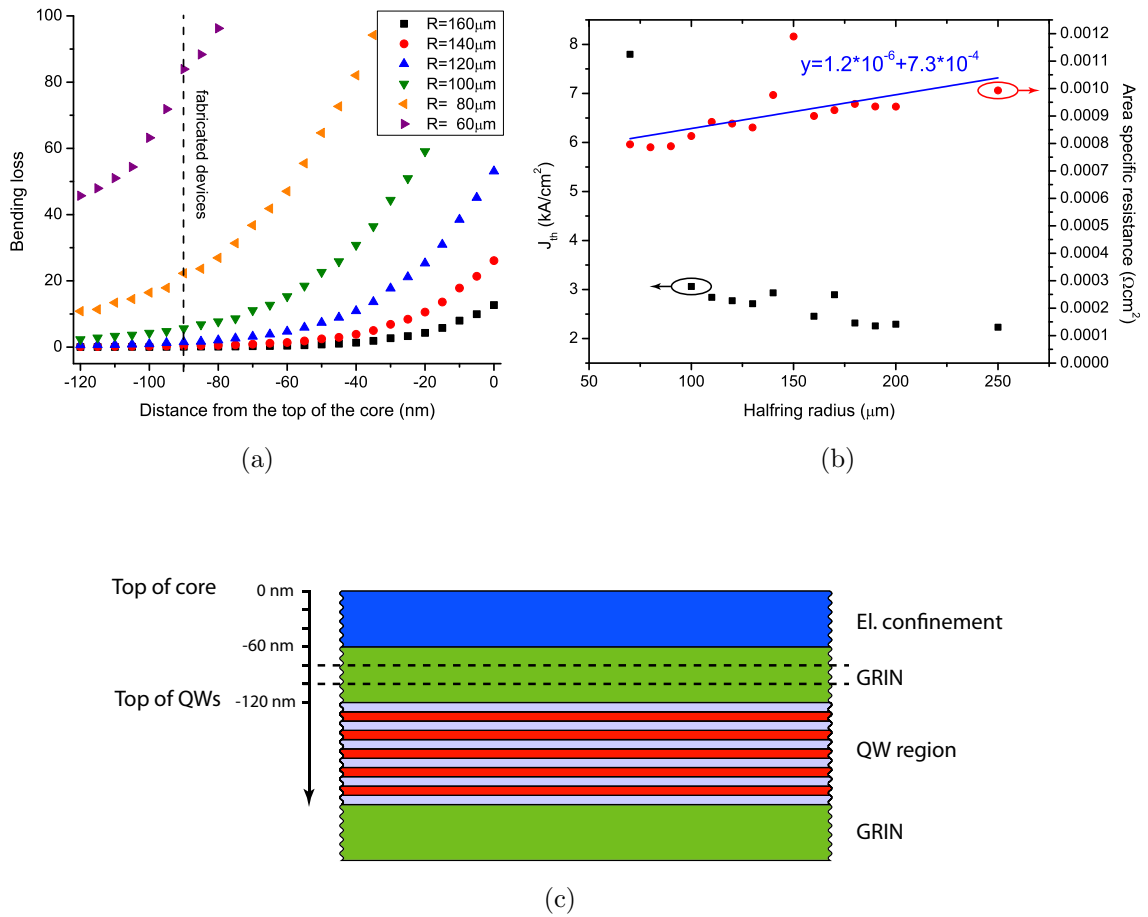


**Figure 4.3:** (a) Simulated bending losses as a function of the etch depth with bending radius as a variable parameter. The 0 value of the x-axis corresponds to a depth where the etch was stopped on the top of the core ( $1.92\mu\text{m}$  total height). (b) Plot of the measured  $J_{th}$  (black squares) and  $r_a$  (red dots) as a function of the radius of 2010 nm deep etched half ring lasers. The  $y=m\cdot x+b$  type linear fit of the  $r_a$  is plotted with a blue line. (c) Schematic of the core cross section.

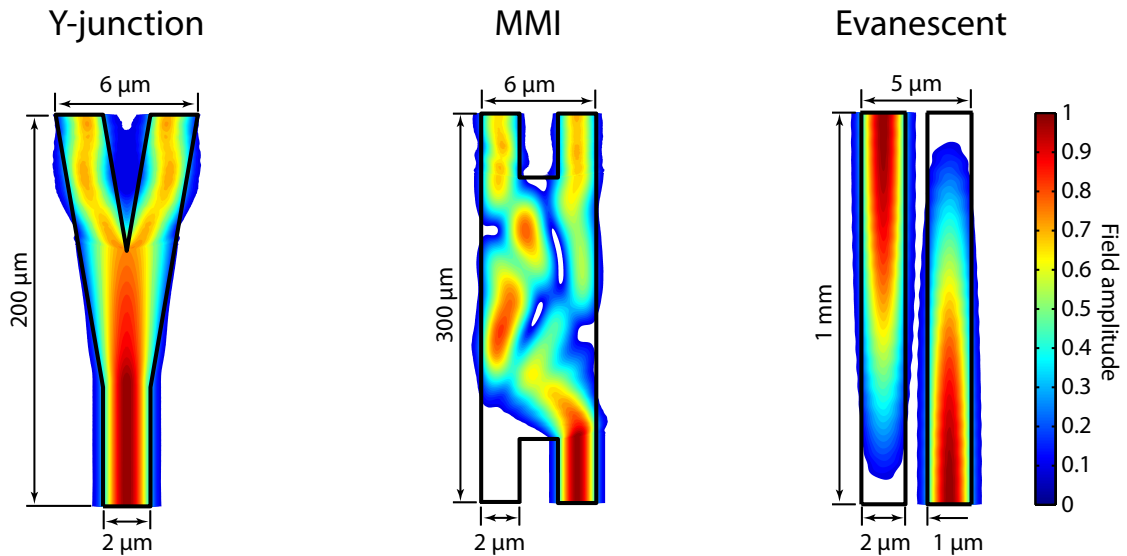


**Figure 4.4:** Schematic of the Y-junction, MMI and directional coupler.

micro size SRLs, but they are small enough to realise SRLs that are compatible with the 100 GHz ITU<sup>3</sup> channel spacing standards (a free spectral range (FSR) of 100 GHz requires a cavity length of  $\sim 860 \mu\text{m}$  or a ring radius of  $\sim 135 \mu\text{m}$ ). Moreover, this approach preserves the design flexibility of shallow etched evanescent field couplers.

### 4.3 Coupler design

Three different coupler types can be used to extract power from shallow etched SRLs, namely: evanescent field couplers (also called directional couplers) [77], multimode interference (MMI) couplers [78] and X- or Y-junction couplers [79]. Figure 4.4 plots the schematic of the three different coupler types. For each coupler also the simulated distribution of the propagating optical field is plotted in order to illustrate their operation. The theory of operation and properties of these couplers is well understood and numerous publications deal with the design and fabrication issues of these elements.

The most compact geometry is the Y-junction coupler. Symmetric branches

<sup>3</sup>International Telecommunication Union

**Table 4.1:** Summary of the properties of the three different coupler types.

	Y-junction	MMI	Directional
Device size	very short	compact	large
Fabrication tolerance	excellent	good	medium
Cross talk	low <sup>a</sup>	low	medium
Pol. sensitivity	no	negligible	sensitive
Uneven splitting	yes <sup>b</sup>	yes <sup>c</sup>	yes
Back-reflections	strong	medium <sup>d</sup>	negligible
Tunability	no	no	yes

<sup>a</sup>depends on the splitting angle

<sup>b</sup>only in asymmetric configurations

<sup>c</sup>only fixed splitting ratios are available

<sup>d</sup>can be reduced if tapered access guides are used

split the power equally, while asymmetric configurations have an angle dependent, oscillatory varying power splitting ratio [80]. Both types produce relatively high intra cavity back-reflections, which increases with the  $\Delta n$  of the waveguide.

MMI couplers are based on the self-imaging nature of multimode waveguides: Along the propagation direction interference effects reproduce single and multiple images of the input field. MMI couplers are ideal 50% couplers but they are not suitable for smaller or larger splitting ratios. MMI devices have a good fabrication tolerance and they are almost insensitive to the polarization of the input field [81]. A drawback of conventional MMI designs is that the access waveguide- multimode section interface has sidewalls perpendicular to the propagation direction. These parts are sources of back-reflection and they can form an unwanted FP subcavity/etalon inside of a SRL. These reflections can be reduced greatly if instead of a sharp, step like transition the waveguide terminates with a linear taper to the MMI region that has a half angle greater than the divergence of the light [82]. A major weakness of MMI couplers is that heavy current pumping detunes the beating length of the modes and so increases their back-reflection. As a consequence these waveguide sections must be kept unpumped, which increases the current threshold of the laser.

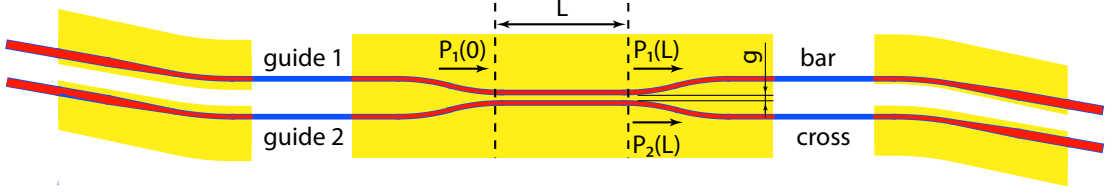


**Figure 4.5:** Schematic of a directional coupler. Devices with a similar layout were used to measure the power splitting of 800 nm wide gap couplers as function of the length.

Directional couplers transfer the optical power between two parallel running waveguides via the overlapping tail of their evanescent fields. These devices need a longer interaction length to achieve the same power transfer when compared to the other two coupler types. One big advantage of directional couplers is that arbitrary coupling ratios can be designed by simply adjusting the length of the coupler. However, the state of polarization of the input field and inaccuracies of the fabrication are critical for these devices since a small mismatch in the propagation constants of the two waveguides can completely change the coupling ratio. This phenomenon is exploited in tunable evanescent field couplers, where the refractive index of one side is intentionally changed either with injected carriers or by applying a reverse voltage [83]. The back-reflection of the directional couplers is negligible, since the light propagating along the waveguides does not encounter any major discontinuity. Table 4.1 summarises the main properties of the three coupler types.

The most important requirement of a coupler, to be used in a SRL cavity, is that it should produce as low coupling between the two counter propagating modes as possible. Therefore, despite of their disadvantages, directional couplers were used in most of the shallow etched SRLs to tap the light of the cavity. Figure 4.5 shows the schematic of a four-port directional coupler. Blue waveguides are passive, without the possibility of electrical pumping, while red ones have an open contact window and current may be injected into or voltage applied on them through the p-type contact pads (yellow). In case the two waveguides are phase matched, then the periodic power transfer between them can be formulated as follow [72]:

$$\frac{P_2(L)}{P_1(0)} = \sin^2(\kappa L), \quad (4.1)$$

where  $\kappa$  is the coupling coefficient,  $L$  is the length of the coupled part,  $P_1(0)$  is the

input optical power, and  $P_1(L)$  and  $P_2(L)$  are output powers in the bar and cross state, respectively. The length,  $L_\kappa$ , for which all of the power is transferred from *guide 1* to *guide 2* is called *beating* or *coupling* length and it is inversely proportional to  $\kappa$  ( $2L_\kappa \equiv \pi/\kappa$ ). The value of the coupling coefficient, which can be calculated as the integral of the overlapping evanescent fields of the two waveguides, depends strongly on the width  $g$  of the gap in between the waveguides. BPM simulations were carried out to investigate the influence of waveguide separation ( $g$ ) and the RIE lag on the beating length of a  $2\ \mu\text{m}$  wide waveguide directional coupler. Results are plotted in Figure 4.6. As expected, a shallower etch or a narrower gap results in a shorter  $L_\kappa$  (stronger  $\kappa$ ). It can also be seen that the etch depth strongly influences the final coupling of the design: For example, a depth inaccuracy of just 20 nm causes an  $L_\kappa$  change of around 20%. Luckily, the large selectivity of the  $\text{CH}_4/\text{H}_2/\text{O}_2$  chemistry on the Al containing layers provides an effective solution to control the etch depth. If one wants to reduce the size of the device, then the best choice is to select an as small a gap as possible. In practice, a compromise has to be found between the extent of the RIE-lag effect and the device size. Based on SEM inspections and the RIE lag data of Figure 2.11(b), gaps of 700 nm to 800 nm were selected to be used for the directional couplers of the SRLs. These separation widths correspond to a beating length of  $419\ \mu\text{m}$  and  $615\ \mu\text{m}$  and require an additional etch time increase of 20% and 25%, respectively.

The accuracy of the coupling length simulations was verified on a set of varying length directional couplers with a gap of 800 nm. The splitting ratio of the devices realised on passive material is usually measured by injecting the light of an external tunable laser source into a waveguide on one side and then the power of both outputs is recorded on the other side. However, facet damage or misalignment of the focusing elements are this method's main source of inaccuracy. Alignment errors were eliminated by using the left contact pad as a reference light source (*guide 1*), rather than an external tunable laser. The optical power out of the bar and cross outputs was collected with a polarisation maintaining (PM) fiber lens and a photodiode was used to record power levels<sup>4</sup>. Figure 4.7 plots the measured power splitting of the fabricated devices as a function of the length of the coupler (red dots). The  $\sin^2(x)$  function fitted to the data (dashed blue line) quantifies the

---

<sup>4</sup>If one wants to use the cross and bar diodes as light detectors, then the lock-in technique should be used to reduce the dark current noise.

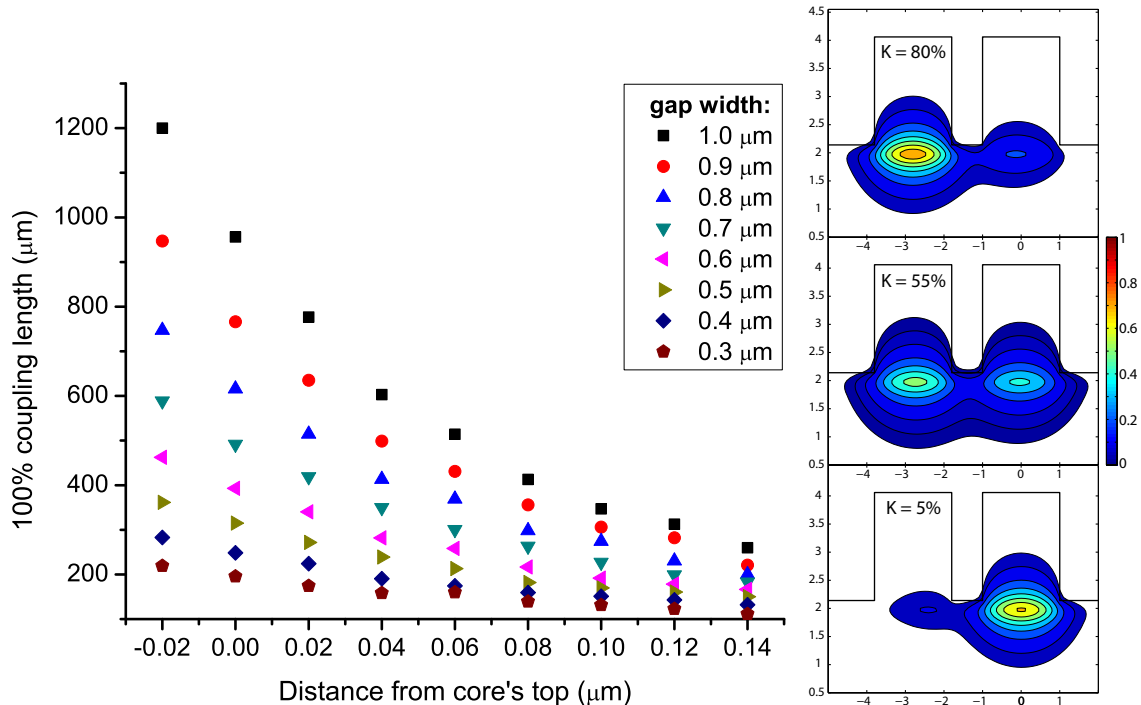


**Figure 4.6:** Simulated beating length of a directional coupler as a function of the distance from the core top with the gap separation as a parameter. Positive values of the x-axis mean a shallower gap. On the right side, the three examples show the contour map of the field distribution of the evolving super mode for splitting ratios of 5 %, 55 % and 80 %.

deviation from the design. Compared to the simulations (drawn with black line), the beating length of the fabricated devices is  $35 \mu\text{m}$  longer. This 5 % increase corresponds either to a few nanometers over etch of the electron confinement layer or to a 20 nm increase of the gap width. The price to pay for the short coupling length of a narrow gap is the increased cross talk: in this case only 87 % of the total power is transferred to the cross arm. Based on the application, it is up to the designer to balance size and cross talk requirements of the device.

A “zero” length directional coupler, also called point coupler, captures just a small fraction of the SRL power and therefore only slightly disturbs the circular symmetry of the cavity. Table 4.2 lists the coupling strength of a few fabricated point couplers with different separation widths. It can be observed that with

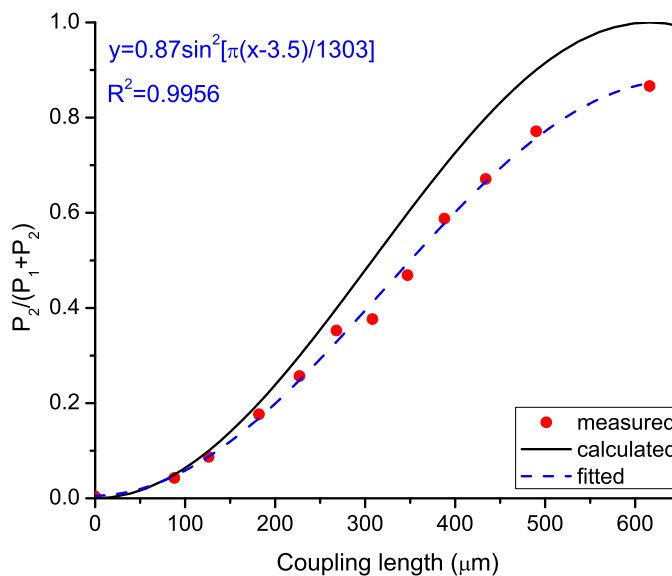


**Figure 4.7:** Measured splitting ratio as a function of the propagation distance of a 800 nm gap evanescent field coupler. The fitted  $\sin^2(x)$  curve is plotted with a dashed blue line. Its equation and coefficient of determination ( $R^2$ ) are given in the top left corner of the graph, and the simulated coupling of the same coupler is plotted with a black line.

**Table 4.2:** Measured power coupling of point couplers. The separation between the two curved waveguides is given in the first row.

	$g=0.8 \mu\text{m}$	$g=1.2 \mu\text{m}$	$g=1.5 \mu\text{m}$
Coupling [%]	0.42	0.1	0.055

increasing gap width the coupling strength decreases. Such a trend is to be expected since with growing gap width the overlap between the evanescent fields of the straight and the curved waveguides decreases, i.e. the coupling between them decreases. Coupling values of around  $10^{-3}$  can be achieved through this geometry and may find applications in coupled multi-ring geometries.

## 4.4 Facet back-reflection

Any back-reflections from the facets of the access bus waveguides into the SRL cavity strongly influence the device behaviour. High feedback levels can spoil unidirectional operation; therefore, it is of utmost importance that these reflections are kept at minimum. There are two well known methods to reduce the reflections of a cleaved facet, namely the application of antireflection (AR) coatings, or tilting of the output waveguides with respect to the cleaving plane. The former requires the deposition of single-layer or multi-layer thin films on the semiconductor – air interface. The refractive index and thickness of these layers is designed such that the reflections from the multiple interfaces interfere destructively and cancel each other. For example, the refractive index ( $n_c$ ) of an optimal single layer coating is the geometric mean of the two surrounding indices and the film thickness is a quarter of the free space wavelength of the light ( $\lambda_0/(4n_c)$ ). The back-reflection from a waveguide facet can also be reduced if the output mirror is placed at an angle. For angles below 10-12 degrees the reflectivity of a dielectric interface does not change significantly, but the amount of reflected power coupled back to the waveguide greatly reduces in the case of sufficiently large angles. Further, the mismatch of the phase fronts of the incident and reflected field causes a  $[\sin(x)/x]^2$  type modulation of the reflection as a function of the angle [84].

The reflectivity of a cleaved waveguide facet has to be determined experimentally in order to quantify the feedback from the output bus waveguide facets to the SRL cavity. Two techniques exist to measure the reflectivity of a cleaved output waveguide facet: a) threshold current shift of a laser, and b) Kaminow-Eisenstein method [85].

The reduction of the laser mirror reflectivity in a FP cavity (due to tilt or AR coating) increases the  $\alpha_m$  of the cavity and thus also increases the threshold current of the device. By using Eq. 3.3 and Eq. 3.4, one can relate the change of the modal reflectivity of a laser mirror to the ratio of the original and new threshold current densities:

$$R_2 = R_1 \ln \left[ \frac{J_1}{J_2} \right]^{2Lg_0}, \quad (4.2)$$

where  $R_1$ ,  $J_1$  are the reflectivity and current threshold density, respectively, of the reference FP laser (uncoated or untilted facets) and  $R_2$ ,  $J_2$  are the reflectivity and



**Figure 4.8:** Layout of a one side tilted FP lasers.

current threshold density of the laser, with coated or tilted facets. It is not possible to measure very low reflectivity values with this technique, since the large mirror losses prevent lasing action.

A second approach, which is better suited for devices with very low reflectivities, such as traveling wave SOAs or superluminescent diodes, derives the mirror reflection loss from the optical spectrum [85]. Here, the devices are biased at the threshold current of a reference device and the mirror reflectivity is calculated from the measured modulation depth of the optical spectrum. Both experimental methods rely on the knowledge of the threshold current of a reference laser with known mirror reflectivities.

FP lasers with one perpendicular mirror and a tilted facet on the other side of the cavity were fabricated with the aim of extracting the angle dependency of the reflectivity of the tilted mirror. A schematic of the layout of the fabricated devices is shown in Figure 4.8. The P–I characteristic of each device was measured, and from the recorded  $I_{th}$  values the corresponding reflectivity was calculated. Results are plotted versus the mirror angle in Figure 4.9. It can be seen that a  $10^\circ$  tilt reduces the back-reflection from the facet down to  $2 \times 10^{-2}$ . Larger angles provide even lower back-reflection levels, but the wide angle of the free space beam makes the light collection a challenging task. Figure 4.9 also plots the measured slope efficiency of the non-tilted facet (slope efficiency of facet B) as a function of the angle. The observed periodic dips in the efficiency are caused by the modulation of reflectivity of the tilted facet, which is a result of the angle dependent destructive interference between incident and reflected fields [84]. It is not recommended to design devices in a way that the low reflection of these minima is exploited, as the position of these local minima is strongly wavelength dependent. Moreover, a bad cleave or a  $\pm 0.1^\circ$  lithographic misalignment of the pattern would ruin such a design easily.

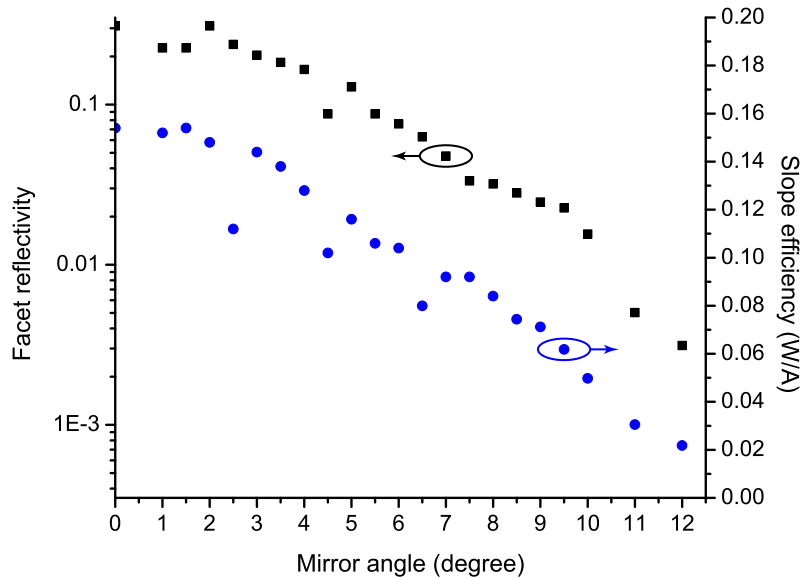


**Figure 4.9:** Measured slope efficiency of the tilted output (blue dots) and facet reflectivity (black squares) as a function of the mirror angle of a  $2\ \mu\text{m}$  wide waveguide FP laser.

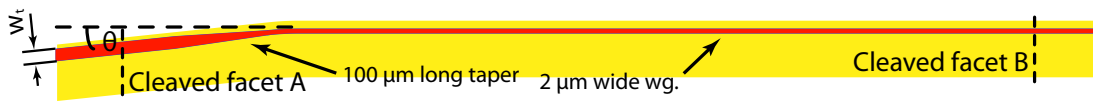


**Figure 4.10:** Layout of the tilted and tapered FP lasers.

A further reduction of the facet reflectivity can be achieved by widening the tilted output waveguide using a taper [84, 86]. A critical design issue is the angle and the geometry of the taper that must be adiabatic to prevent modal conversions between the fundamental and higher order modes. In fact, depending on the taper width  $w_t$ , higher order modes may have a maximum of reflection whereas the fundamental mode has a reflection minimum [86]. It has to be noted that tapering a waveguide without tilt does not change the modal reflection from the facet.

In order to characterise the effect of the taper width on the facet reflectivity, FP lasers with a tilted and tapered waveguide on one side, and a perpendicular mirror on the other side were designed. Figure 4.10 shows a schematic of these devices. Two different FP sets were fabricated with tilt angles ( $\theta$ ) of 6 and 10 degrees and a  $w_t$  ranging from  $2\ \mu\text{m}$  to  $12\ \mu\text{m}$ . As before, the  $J_{th}$  of the devices was measured and

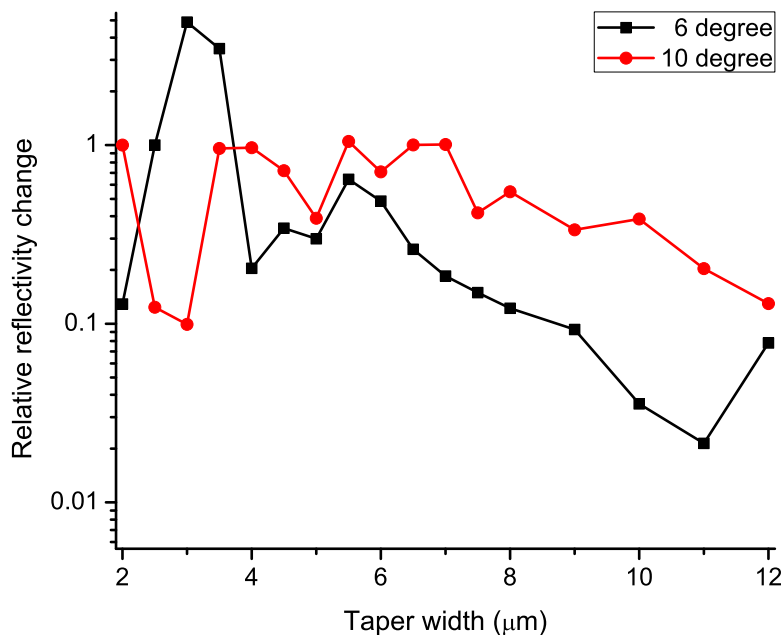


**Figure 4.11:** Measured relative reflectivity change of tilted waveguides as a function of their tapering width.

from this data the corresponding reflectivity of the tapered mirrors was calculated. Figure 4.11 plots the relative reflectivity change of the tilted outputs as a function of their width. It was found that the measured series resistance ( $r_s$ ) of the FP laser with a  $2\ \mu\text{m}$  wide and 6 degree tilted output is two times higher than the  $r_s$  of all the other devices. Possibly this is the result of a contaminated contact window that causes a spuriously high  $J_{th}$ , therefore this particular reflectivity value cannot be regarded as a reference for normalisation (but it is still plotted). For this reason, the reflectivity of the 6 degree tilted FPs was normalised to the reflectivity of the  $2.5\ \mu\text{m}$  tapered device. In the case of 10 degree tilted FPs, the reflectivity of the non-tapered,  $2\ \mu\text{m}$  wide device was used as a reference for normalisation. Although measurement points show a strong scattering, a clear trend of decreasing reflectivity can be observed, with a  $\sim 10$  times reflectivity reduction on a  $12\ \mu\text{m}$  wide taper. A possible explanation for the dips and peaks in the reflectivity, that is plausible with the theoretical results of [84], is as follows: As the width of the waveguide increases the  $[\sin(x)/x]^2$  modulation frequency of the reflectivity increases ( $x$  depends on the tilt angle, on the wavelength and on the waveguide width) and therefore some of the measured points may fall on or near the minima of this periodic function.

Based on the previously reported reflectivity measurements, it was decided to use a  $10^\circ$  tilted and  $12\ \mu\text{m}$  tapered waveguide output for the SRL devices. A further advantage of such a geometry is that the fiber lens alignment to a wide output facet is less sensitive to mechanical vibrations. This is particularly useful when several hours long automated measurements are carried out.

## 4.5 Overview of shallow etched ring laser characteristics

In the course of this work more than one hundred shallow etched, four port SRLs were fabricated with the aim of providing a large number of devices for testing the temporal switching response of SRL devices. Based on the results of the previous sections the following geometrical parameters were used:

- Device radius of  $150\ \mu\text{m}$  and  $200\ \mu\text{m}$
- Output coupler strengths of  $10\ \%$  and  $50\ \%$
- Two output bus waveguides
- Five p-type metal contacts are formed to allow separate biasing of the ring and the output SOAs
- The width of the output waveguides is tapered to  $12\ \mu\text{m}$  at an angle of  $10^\circ$  for reducing back-reflections
- Output waveguide spacing of  $270\ \mu\text{m}$  for fiber array compatibility

These specifications yield four different SRL geometries with cavity lengths ( $L$ ) of  $1.1\ \text{mm}$  ( $r=150\ \mu\text{m}$   $K=10\ \%$ ),  $1.3\ \text{mm}$  ( $r=150\ \mu\text{m}$   $K=50\ \%$ ),  $1.4\ \text{mm}$  ( $r=200\ \mu\text{m}$   $K=10\ \%$ ) and  $1.6\ \text{mm}$  ( $r=200\ \mu\text{m}$   $K=50\ \%$ ). The schematic of the bar design that consists of seven devices can be seen in the top part of Figure 4.12. The bottom of the figure shows the optical micrograph of a fabricated,  $L=1.3\ \text{mm}$  device.

The performance of the SRL devices was assessed by recording the P–I and V–I characteristics of 37 devices. As an example the P–I curve of a  $1.3\ \text{mm}$  long cavity<sup>5</sup> ( $r=150\ \mu\text{m}$  and  $K=50\ \%$ ) is plotted in Figure 4.13 to illustrate the

---

<sup>5</sup>Throughout the section the characteristics of this device will be shown as an example.

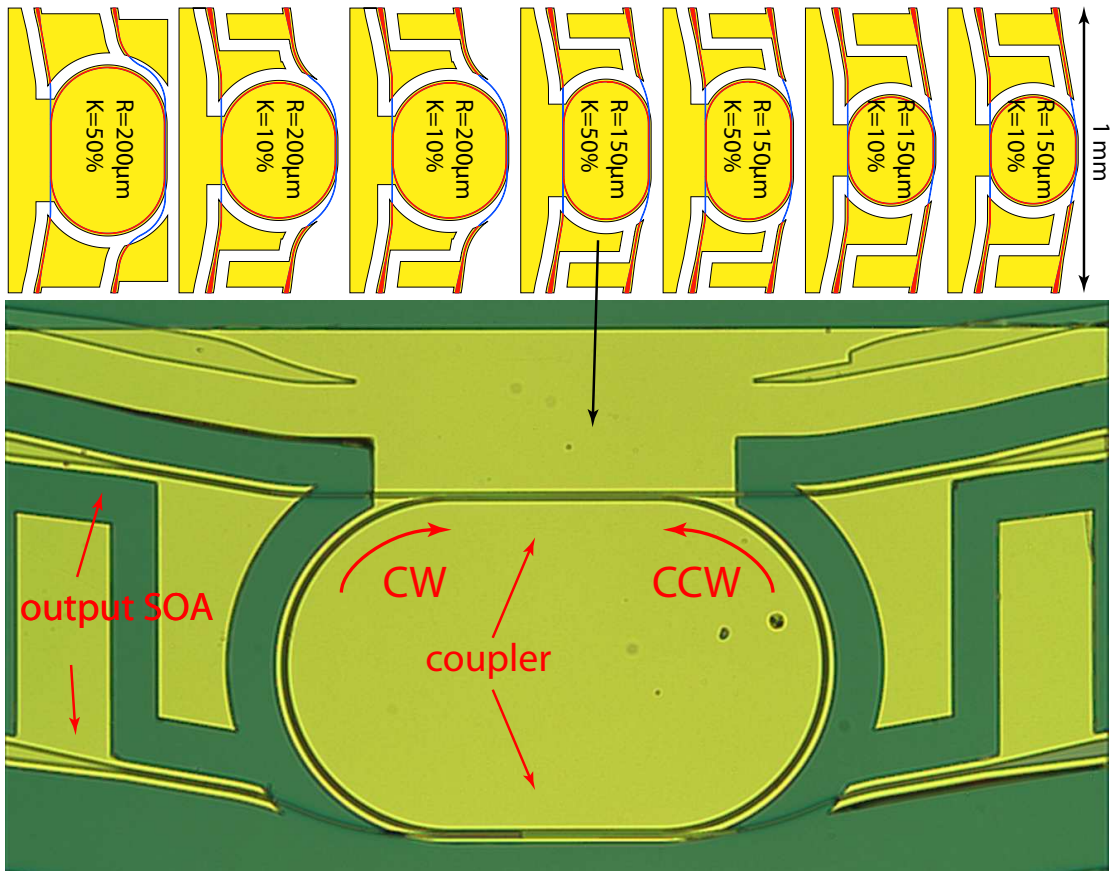


**Figure 4.12:** Optical micrograph of a  $150\ \mu\text{m}$  radius racetrack shaped SRL. On the top the schematic of the SRL bar design for switching experiments can be seen.

general behaviour of the fabricated SRL devices. From threshold ( $I_{th}=30\ \text{mA}$ ) to an injected current value of  $42\ \text{mA}$ , the counter-propagating modes lase simultaneously (bidirectional region). A further increase of the current level leads to unidirectional operation, where only one direction lases, while the other is suppressed due to cross gain saturation. The relatively short,  $\sim 10\ \text{mA}$  wide bidirectional region and the long and robust unidirectional region is a crucial requirement for all-optical flip-flop operation, as in these applications the bistable property of the unidirectional SRL is exploited. Compared to previously fabricated SRLs, this design shows excellent unidirectional behavior thanks to the minimal coupling of the counter-propagating modes [52,20] that is a result of the low back-reflection from the tilted and tapered facets and the very low waveguide roughness. In fact theory shows that in an

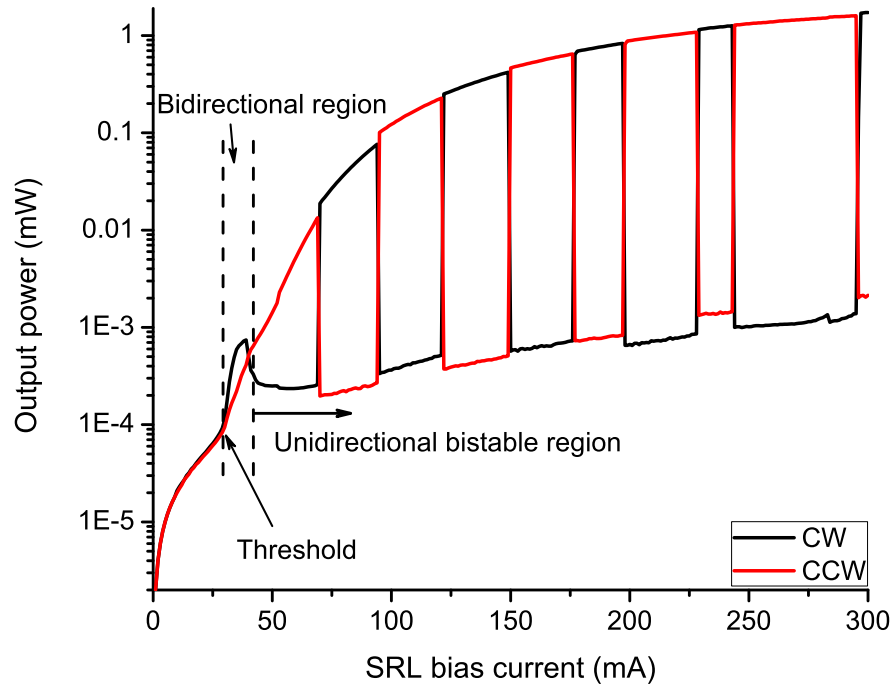


**Figure 4.13:** Measured P–I characteristic of a 150  $\mu\text{m}$  radius and 50% coupler SRL.

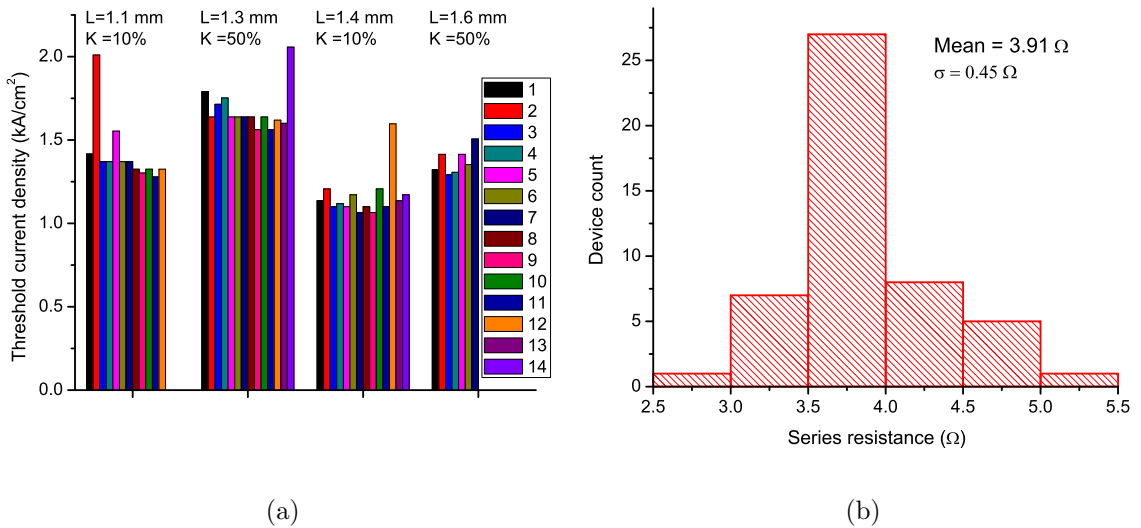


**Figure 4.14:** Device performance statistics. (a) Recorded threshold current density of 37 devices. The columns are grouped for SRLs of the same geometry. (b) Histogram plotting the measured series resistance distribution of the SRL devices.

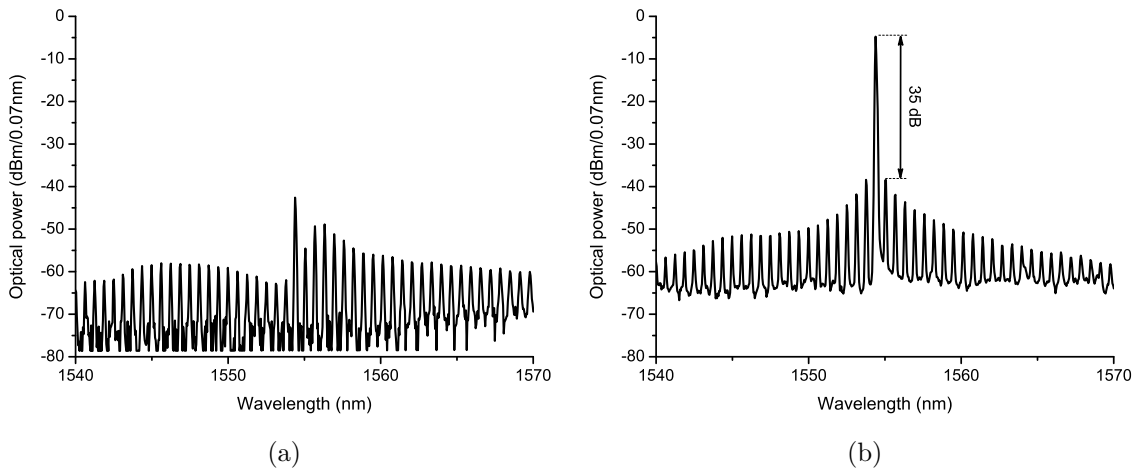


**Figure 4.15:** Measured optical spectra of a  $150\ \mu\text{m}$  radius and 50% coupler SRL for the  $I_{SRL}$  of 200 mA. (a) CW direction. (b) CCW direction.

ideal ring laser (i.e. no coupling between CW and CCW travelling waves) the strong gain competition of the counter-propagating waves leads to unidirectional bistable operation [87, 88]. However, in real devices the output coupler and the bus waveguide breaks the rotational symmetry of the SRL (i.e. the CW and CCW waves become coupled) and new operational regions, such as the bidirectional, appear [20]. In case of weakly coupled counter-propagating modes only a relatively short bidirectional region is predicted before the SRL transits to unidirectional bistable operation (as seen on the P–I curve in Figure 4.13).

The fact that 98% of the finished devices exhibited room temperature *cw* lasing indicates the excellent quality of the fabrication processes. Assessment of the fabrication uniformity was performed by analysing the recorded P–I and V–I characteristics of SRLs from a  $11 \times 12$  mm size chip. For each device, the threshold current density ( $J_{th}$ ) and the series resistance ( $r_s$ ) was evaluated. Figure 4.14(a) shows the bar plot of the  $J_{th}$  for the four different cavity geometries. It can be seen that the threshold values corresponding to each device group are highly uniform, only a minimal scattering can be observed. Figure 4.14(b) plots the histogram of the evaluated series resistance distribution of the SRLs. Statistical analysis of the data shows that the devices have a mean  $r_s$  of  $3.91\ \Omega$  with 95% ( $2\sigma$ ) of the recorded values within a  $\pm 0.9\ \Omega$  interval.

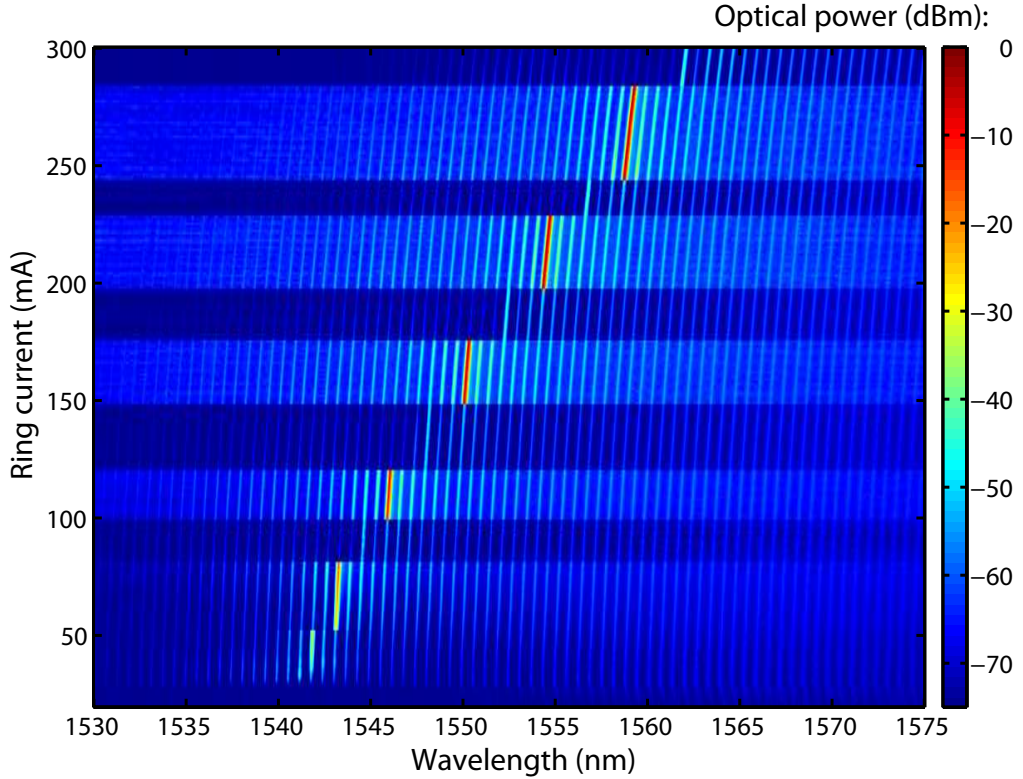


**Figure 4.16:** Measured CCW direction spectral map of the device whose P–I curve is reported in Fig 4.13. The bar on the right side links the optical power in dBm to the colours.

Finally, the optical spectrum of few selected SRLs was measured and from the collected data the directional extinction ratio (DER)<sup>6</sup> and SMSR of the devices was evaluated. DER and SMSR values as high as 30-35 dB can be observed in Figure 4.15, where the CW and CCW optical spectra of an SRL device is plotted for the bias current ( $I_{SRL}$ ) of 200 mA ( $\sim 5.5 \times I_{th}$ ). It has to be noted that all the tested devices show similarly excellent DER and SMSR values.

It was shown in Fig. 4.13 that with increasing  $I_{SRL}$  directional reversals can be observed in the unidirectional operation region. These directional flips are accompanied by jumps in the lasing wavelength, as is illustrated in the spectral map of Figure 4.16. Each of the four fabricated SRL geometries show similar wavelength

<sup>6</sup>Defined as the ratio of the CW and CCW peak optical power of the recorded optical spectra at a particular SRL current.

jumps over three FSRs. Both the wavelength jumps and the directional reversals are the result of preferential longitudinal mode selection that arises from the red shift of the gain peak and the transmission characteristics of the SRL device [88, 75, 52]. These modal properties were studied extensively in other papers, therefore they are not reported here in detail.

## 4.6 Chapter summary

This chapter described in detail the design issues of shallow etched waveguide semiconductor ring lasers. First, simulations were carried out to identify the optimum waveguide width for single mode operation and low bending losses. Results show that a width of  $2\ \mu\text{m}$  and an etch depth of  $1.92\ \mu\text{m}$  ensure single mode operation, with negligible bending losses down to radii of  $150\text{--}200\ \mu\text{m}$ .

The bending radius can be further reduced by etching into the Al containing upper confinement layers. The very slow etch rate of these layers provided an accurate control of the etch depth. Measurements carried out on fabricated half ring lasers showed that bends with a total etch depth of  $2010\ \text{nm}$  ( $30\ \text{nm}$  above the QWs) have low bending losses down to a radius of  $100\ \mu\text{m}$ . Such smaller radii become crucially important for the development of devices that match the  $100\ \text{GHz}$  ITU grid (cavity length of  $\sim 860\ \mu\text{m}$ ).

Integrated coupler geometries (Y-junction, MMI and directional) for extracting power from the ring cavity were reviewed. Directional couplers were selected as the best option in shallow etched SRL designs because their coupling ratio is easily adjustable and their low intra cavity back-reflections do not prevent unidirectional device operation. Based on simulation results, waveguide separation gaps of  $700\ \text{nm}$  to  $800\ \text{nm}$  were selected for these couplers. Measurements on fabricated  $800\ \text{nm}$  gap directional couplers showed that even the slightest fabrication inaccuracies may cause a few percent deviation from the designed beating length. It was also found that such small separation couplers have a cross talk of around  $9\ \text{dB}$ .

In order to reduce the coupling between the counter-propagating modes of the cavity, the output facet reflections were reduced. By tilting the outputs  $10^\circ$  with respect to the cleaving plane and by tapering the output waveguides to a width of  $12\ \mu\text{m}$  reflections levels of around  $10^{-3}$  were demonstrated.

Finally, based on the design considerations gathered in the previous part of

the chapter, four different SRL cavity geometries with lengths of 1.1 - 1.6 mm were designed and fabricated. The good fabrication quality of these SRLs was confirmed by the fact that more than 98% of them exhibited *cw*, room temperature lasing with a current threshold dispersion of less than 2 mA. Thanks to the careful design optimisation for low coupling between the counter-propagating modes, very robust, and high DER and SMSR unidirectional lasing was observed on the fabricated SRLs. No lifetime analysis was performed but most of the devices, fabricated in the first batch, still lase after 3 years with no sign of performance degradation. The excellent reliability of these SRLs<sup>7</sup> allowed the start of an intensive and successful research in the field of all-optical switching, that produced more than 30 peer reviewed papers and publications. The main findings and most important results of this research will be summarised in Chapter 6.

---

<sup>7</sup>Project nickname TD2p2 devices.

# Chapter 5

## Deep etched design

In this chapter, the design considerations of deep etched SRLs are discussed. The very strong horizontal mode confinement of very small radius deeply etched waveguides allows for the miniaturisation of SRL devices. Most of the design rules and fabrication procedures for these geometries, however, were never optimised before. Therefore a number of challenges need to be carefully addressed. The key requirements are: single transverse mode operation for kink free laser operation; smooth, adiabatic straight to curved transitions for racetrack cavities; short and strong couplers for high output power levels. All these issues were investigated in detail with a strong focus on keeping the intra cavity back-reflections low, and hence preserving unidirectional operation.

### 5.1 Waveguide design

Similarly to the shallow etched devices, the first design step is to optimise the waveguide dimensions, so that only a single transverse mode exists. The horizontal confinement of a waveguide increases greatly, when the etching penetrates the optical core of the material. This also affects the shape of the modal profile that becomes more symmetrical, almost circular (see Figure 5.1.a). BPM simulations were initially carried out with the waveguide depth fixed to  $3.2\ \mu\text{m}$  ( $1\ \mu\text{m}$  below the core) to investigate how the increased horizontal confinement influences the losses of the supported transverse modes. Figure 5.1.b plots the simulated modal effective index of the first three TE modes as a function of the waveguide width ( $w$ ). Compared

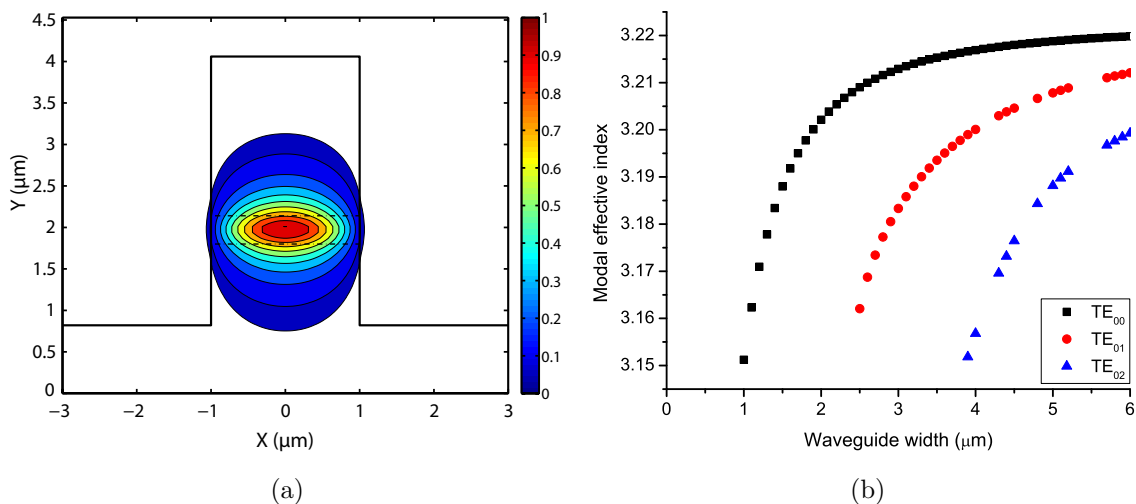


**Figure 5.1:** (a) The contour map of the  $TE_{00}$  mode of a  $2\ \mu\text{m}$  wide and  $3.2\ \mu\text{m}$  deep waveguide. The straight line plots the waveguide bounds and the dash dotted line indicates the core of the material. (b) Simulated modal  $n_{eff}$  of the first three TE modes plotted versus the waveguide width.

to the shallow etched waveguide geometry (see Figure 4.1.b), the corresponding higher order optical mode cut-off occurs at larger values of the waveguide width. A simple explanation of this is as follows: the horizontal confinement is much stronger than the vertical one, and - as the width of the waveguide is reduced - the guided optical mode is squeezed along the horizontal direction, the optical field expands vertically and the substrate losses becomes dominant. Below a width of  $2.4\ \mu\text{m}$  no higher order TE modes are supported and the waveguide becomes single mode. Based on these simulations the optimum width range for low loss and single mode operation is between  $2\ \mu\text{m}$  and  $2.4\ \mu\text{m}$ .

Three different batches of 1 mm long, deeply etched FP lasers were fabricated with the aim of confirming the calculated waveguide losses. Each device set was fabricated with a different dry etch chemistry. Waveguides were etched to a depth of  $2.7\ \mu\text{m}$ ,  $3.1\ \mu\text{m}$  and  $4.5\ \mu\text{m}$  with the  $\text{Cl}_2/\text{CH}_4/\text{H}_2$ ,  $\text{Cl}_2/\text{Ar}/\text{N}_2$  and  $\text{Cl}_2/\text{Ar}/\text{BCl}_3$  chemistries, respectively. Figure 5.2 plots the measured threshold current density as a function of the waveguide width of the FP lasers for the three different chemistries. The trend of the measured  $J_{th}$  values agrees well with the BPM simulations: For widths smaller than  $2\ \mu\text{m}$  the threshold increases sharply indicating a pronounced

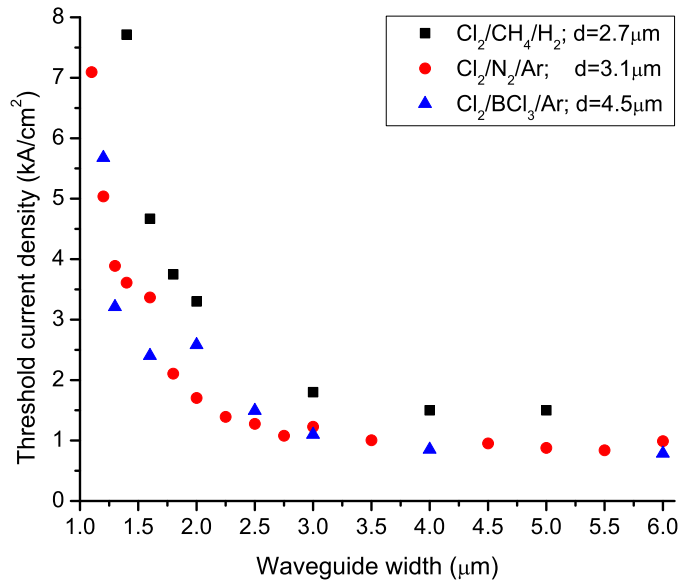


**Figure 5.2:** Measured threshold current density of FP lasers as a function of the waveguide width.

increase of losses. Below a width of  $1\ \mu\text{m}$ , which is the calculated cut-off width of the  $\text{TE}_{00}$  mode, devices cease lasing. One can also observe that the etch depth does not influence the waveguide losses considerably (the higher  $J_{th}$  values of the waveguides etched with the  $\text{Cl}_2/\text{CH}_4/\text{H}_2$  chemistry, are the result of metallisation problems). The threshold current minimum can be found between the widths of  $2\text{--}3\ \mu\text{m}$ . No kinks, associated with the lasing of higher order modes, were observed up to three times threshold on the P–I characteristics. Based on the simulations and measurements, waveguide widths between  $2\ \mu\text{m}$  and  $3\ \mu\text{m}$  appear as an optimum choice for low threshold SRL devices. Note that the theoretical cut-off (see Fig. 5.1(b)) for the first order mode is at  $w=2.4\ \mu\text{m}$ ; however the real cut-off is shifted to waveguide widths larger than  $3\ \mu\text{m}$  because of waveguide imperfections that increase the losses of the weakly guided first order mode. This figure is shifted even further if bent waveguides are used (see Section 5.3).

## 5.2 Non-radiative losses

The three main non-radiative processes of a semiconductor laser are: defect or impurity recombination, Auger recombination and surface recombination [72]. Fig-

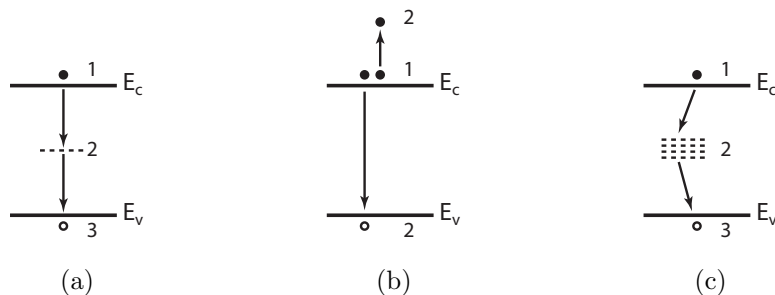


**Figure 5.3:** Non-radiative recombination processes. (a) Defect and impurity recombination. (b) Auger recombination. (c) Surface recombination.

Figure 5.3 illustrates these recombination processes. Material defects and impurities, such as a void at an atomic site or undesired dopant atoms, introduce inter band energy levels. In the case of Auger recombination the collision of two electrons knocks one to a higher energy state and the other to a lower state in the valence band. Both of these processes are related to the intrinsic material properties and layer quality, therefore they must be addressed during the epitaxial layer design and growth. They are not discussed further as material design and growth is out of the scope of this work.

It is inevitable that unmatched bonds will be incurred at the terminations of a crystal by deep etching waveguide structures or at the interfaces between different layers during epitaxial growth. These dangling bonds can act as a trap or a recombination center for carriers and, if present in a high density, they can form minibands inside the bandgap. Interface recombination of epitaxial stacks is minimal thanks to the high quality of today's growing technologies. On the other hand, etched waveguides may suffer from poor sidewall quality, and thus from high recombination levels that depletes the carriers within one diffusion length from the sidewalls. This effect is especially detrimental when the surface area over volume ratio of a device is large (i.e. narrow waveguides/rings or small diameter disks/VCSELs). The effect of the recombination current can be inserted into the phenomenological equations as a reduction of the effective carrier density in the quantum wells, more specifically:

$$J_w = \eta_r \eta_i J, \quad (5.1)$$

where  $J$  is the current density injected into the device,  $J_w$  is the current density in



**Figure 5.4:** Schematic of the transmission loss measurement setup.

the QWs and  $\eta_r$  is the relative change of internal efficiency due to recombination effects. By combining this equation with Eq. 3.6 one can calculate the  $\eta_r$  from the measured threshold current density data of the different width FP lasers. Because this equation contains  $\alpha_i$ , which varies with the waveguide width, the transmission loss of the FP lasers must be known before calculating  $\eta_r$ . A simple technique for measuring transmission losses is the FP contrast method [89], the setup of which is shown in Figure 5.4. The internally modulated, polarised output of the tunable laser is injected into the waveguides by a PM fiber lens. On the other side of the chip an objective lens is used to collimate the output light of the waveguide and the intensity is detected by a photodiode. The wavelength sweep time of the tunable laser is synchronised to the time sweep of the oscilloscope with the trigger signal, so that the screen of the oscilloscope displays the spectral transmission of the device. From the modulation depth of the measured FP fringes the device propagation losses can be calculated. To minimise the contribution from the band edge absorption, the measurements were carried out at the wavelength of 1580 nm (i.e. 25-30 nm below the bandgap of the material). The collected data is plotted in Figure 5.5 as a function of the waveguide width (red dots). Below the width of 1.3  $\mu\text{m}$  the loss of the 1 mm long waveguide becomes so high that no spectral modulation could be observed. In order to predict the transmission loss for narrower widths an exponentially decaying function was fitted to the recorded data (dashed black line). The relative efficiency change as a function of  $J_{th}$  and  $\alpha_i$  can be expressed by combining Eq. 3.6 and Eq. 5.1:

$$\eta_r \simeq \frac{J_0}{J_{th}\eta_i} \exp \left[ \frac{\alpha_i - \frac{1}{L} \ln(R)}{n_w \Gamma g_0} - 1 \right]^{-1}. \quad (5.2)$$

Using the previously measured  $J_{th}$  values of the FP lasers combined with the fitted

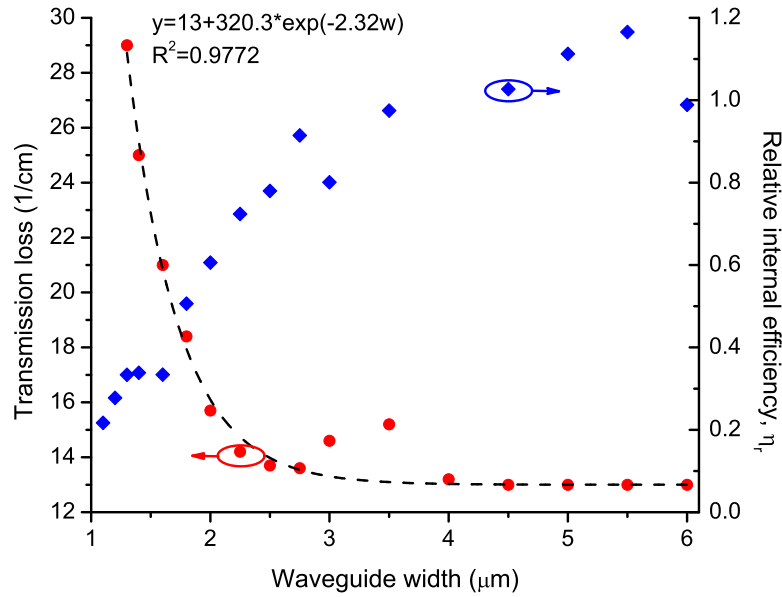


**Figure 5.5:** Measured transmission loss and calculated relative efficiency as a function of the waveguide width. The dashed line plots the  $y=y_0+A*\exp(-b*x)$  fit of the transmission loss data.

data of  $\alpha_i$  and with the material parameters extracted from shallow etched devices (see Table 3.3), the relative change of the internal efficiency ( $\eta_r$ ) was calculated and plotted in Figure 5.5 as a function of the waveguide width (blue rhombuses). The bigger than one relative efficiency values are the result of lateral current spreading present in shallow etched lasers, which have a slightly higher average threshold current density (and so  $J_0$ ) compared deeply etched devices. Two regions with different slopes can be distinguished on the plot with a knee point at a width of around 2.25 - 2.5  $\mu\text{m}$ . The change of slope below the knee point can be explained by the increased recombination rate of the carriers, which happens as the waveguide width becomes less than twice the diffusion length. The plotted data show clearly that the contribution of surface recombination to the device losses is minimal down to a width of 2 - 2.5  $\mu\text{m}$  and that below this width recombination strongly degrades lasing performance. In fact this is the main reason for the  $J_{th}$  increase, which can be observed in Fig. 5.2. Deeply etched waveguides with a width narrower than 2  $\mu\text{m}$  require a passivation of the dangling bonds at the surfaces [90, 91, 92, 93].

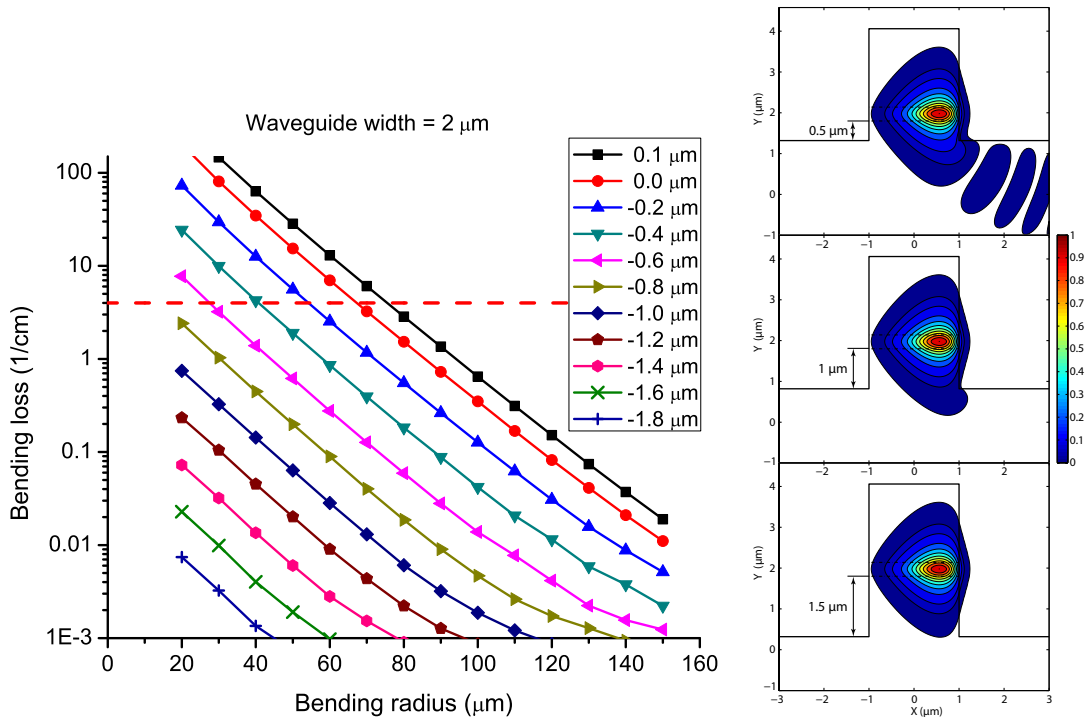


**Figure 5.6:** Simulated bending losses of a deeply etched waveguide as a function of the bend radius, with the etch depth as a parameter. On the right side, the three examples plot the contour map of the field distribution of a 20  $\mu\text{m}$  radius and 2  $\mu\text{m}$  wide waveguide for etch depths of 2.76  $\mu\text{m}$ , 3.26  $\mu\text{m}$  and 3.76  $\mu\text{m}$ .

### 5.3 Bending losses

Below a radius of 150–120  $\mu\text{m}$  the shallow etched waveguide geometry suffers from very high bending losses. A further radius reduction of approximately 50  $\mu\text{m}$  can be achieved with the “semi-shallow” approach, presented in Chap. 4. Smaller device dimensions require a different waveguide geometry with a deeply etched profile well below the core layers. 3D BPM simulations were performed to quantify the decrease of bending losses as the waveguide height increases. This method provides accurate results if the radius is much greater than the waveguide width (i.e.  $r \geq 10 \mu\text{m}$ ). Bends narrower than this can be simulated with other methods, which do not use the paraxiality approximation, such as the finite difference time domain (FDTD) technique. Figure 5.6 plots the bending losses as a function of the radius with

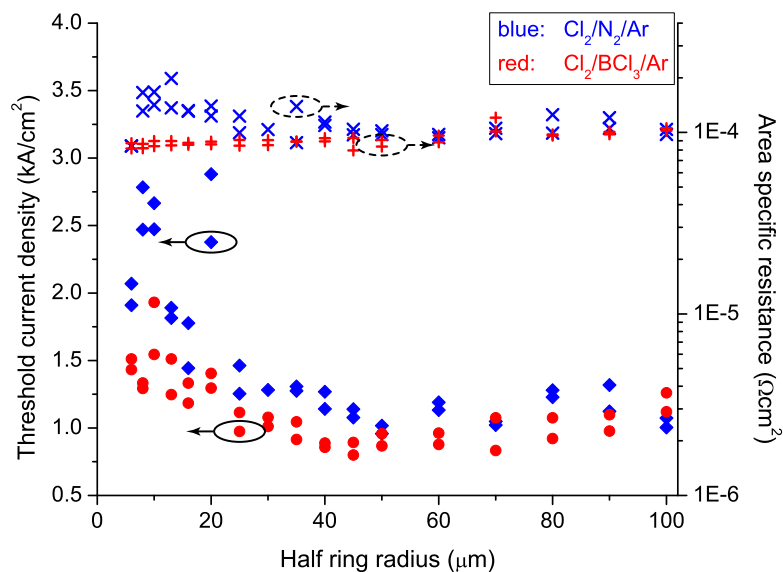


**Figure 5.7:** Measured threshold current density (rhombuses and circles) and area specific resistance (crosses) of half ring lasers as function of the radius. Blue colored points belong to the  $\text{Cl}_2/\text{Ar}/\text{N}_2$  and the red colored ones to the  $\text{Cl}_2/\text{Ar}/\text{BCl}_3$  etch.

the relative depth from the bottom of the material core as a parameter. Results indicate a ten times decrease in the curvature loss for every 400 nm increase of the waveguide height. By extrapolating the straight lines of the semi-logarithmic plot for radii below 20  $\mu\text{m}$ , one can predict that bent waveguides with a total depth of 3.26  $\mu\text{m}$  (i.e. 1  $\mu\text{m}$  below the core) have negligible bending losses down to a radius of few microns. The three transverse field distribution maps in the right side of Figure 5.6 illustrate how the lossy evanescent component of the field diminishes as the slab height is increased. Relying only upon the shape change of the modal cross section, one can intuitively predict that bending losses will be completely negligible if the etched lower cladding is at least as high as the upper cladding (a total etch depth of 4.2  $\mu\text{m}$ ). This conclusion agrees well with the calculated bending loss data.

Half ring lasers consisting of a half circle and of two 200  $\mu\text{m}$  long straight sections were fabricated with the aim of confirming the bending loss simulations with experiments. The external radius of the half rings was varied from 6  $\mu\text{m}$  to 100  $\mu\text{m}$ . Two device sets with waveguide widths of 2  $\mu\text{m}$  and 3  $\mu\text{m}$  were etched with the  $\text{Cl}_2/\text{Ar}/\text{N}_2$  and the  $\text{Cl}_2/\text{Ar}/\text{BCl}_3$  chemistries (etch depths of 3.1  $\mu\text{m}$  and 4.5  $\mu\text{m}$ ,

respectively). Figure 5.7 plots both the device threshold current density ( $J_{th}$ ) and the area specific contact resistance ( $r_a$ ) of the  $3\ \mu\text{m}$  wide half rings as function of the radius. The shallower devices (blue colored data) have a consistently higher  $J_{th}$  values in the radius range of  $8\ \mu\text{m}$  to  $20\ \mu\text{m}$ . However, a series resistance increase of 1.5 to 2 times was recorded on these half rings suggesting a contamination of the contact window or a non-perfect annealing of the p-type metallic contacts. Based on this observation it can be concluded that the threshold values of the shallower etched devices can not be trusted for further evaluation, but the data of the deeper etched devices can be used.

The half rings show a slowly increasing trend of the  $J_{th}$ , which can be explained with the growing mirror losses per unit length as the cavity length decreases. Calculations - using Eq. 3.6 - indicate that the shortest devices should have a  $\sim 1.3$  times higher threshold current density than the longest ones. A small radius bent section accounts only for  $\sim 5\text{-}10\%$  of the total cavity length, therefore its contribution to the total cavity losses becomes only visible, in the form of a threshold change, when it is very lossy. For example a half circle, with a total bending power loss of  $10\%$ , changes the  $J_{th}$  of a  $400\ \mu\text{m}$  long cavity from  $1.46\ \text{kA}/\text{cm}^2$  to  $1.52\ \text{kA}/\text{cm}^2$ . Such a small threshold change is hard to detect experimentally, as a slightly damaged mirror or a contaminated contact window can cause a similar increase. Despite the insensitivity of this design to low bending losses levels, the radius for which bending losses become intense, should be easily detectable this way. For example a  $180^\circ$  bend with a bending power loss of  $50\%$  and  $90\%$  increases the  $J_{th}$  of a  $400\ \mu\text{m}$  long cavity to  $1.98\ \text{kA}/\text{cm}^2$  and  $4.05\ \text{kA}/\text{cm}^2$ , respectively. As no sharp increase of the threshold current density could be observed, it can be concluded that the measured data confirms the main findings of the simulations, namely: bending losses can be neglected down to a radius of  $3\text{-}4\ \mu\text{m}$  if the waveguides are etched to a depth of  $4.5\ \mu\text{m}$ . Furthermore, based on the measured  $J_{th}$  value of the  $3.1\ \mu\text{m}$  deep and  $6\ \mu\text{m}$  radius half ring, it can be concluded that the shallower etched bends do not show a considerable bending loss increase down to a radius of  $6\ \mu\text{m}$ .

The previous set of simulations and measurements analyzed the effect of bending losses as a function of the waveguide depth only and for a fixed waveguide width of  $2\ \mu\text{m}$ . Because the bending losses depend on both the width and depth of the waveguide, BPM simulations were performed to determine the propagation losses as a function of the waveguide width with the bending radius as a parameter, of

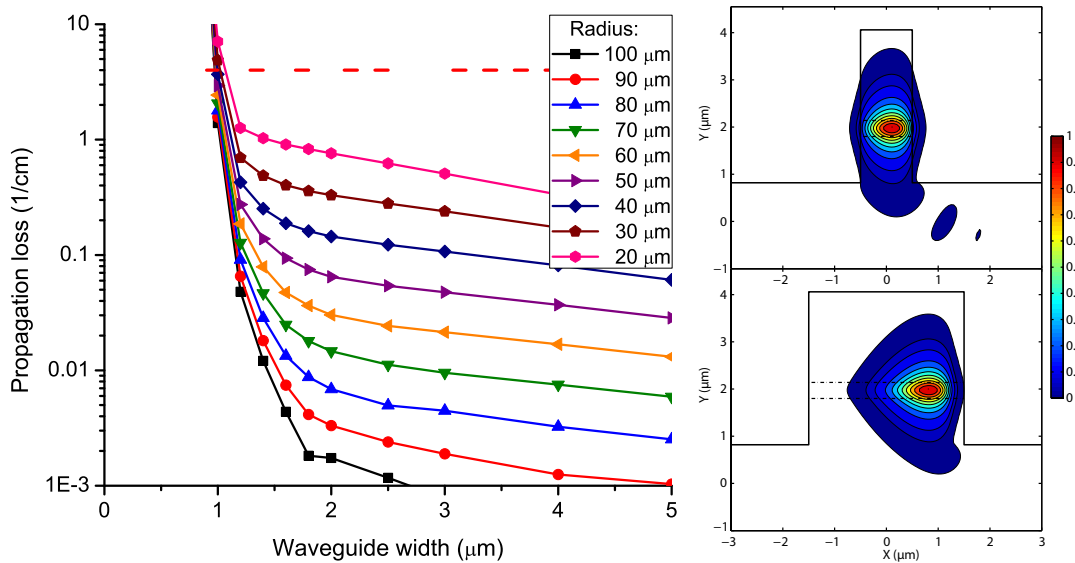


**Figure 5.8:** Simulated bending losses as a function of the width of a deep etched waveguide, with the radius as a parameter. On the right side, the two contour maps illustrate the field distribution of a  $3.26 \mu\text{m}$  high and  $20 \mu\text{m}$  radius curve for waveguide widths of  $1 \mu\text{m}$  (top) and  $3 \mu\text{m}$  (bottom).

which results are plotted in Figure 5.8. Each curve shows a similar trend: for larger widths, the bending losses dominate the propagation losses. Below a width of  $2 \mu\text{m}$ , strong substrate losses overtake the bending losses. These simulation results suggest that the modal cut-off and optimum operation width of a curved waveguide does not change significantly as a result of the bend. Like before, half ring lasers consisting of a  $40 \mu\text{m}$  diameter bend and two  $200 \mu\text{m}$  straight sections were fabricated with a width varying from  $1 \mu\text{m}$  to  $5 \mu\text{m}$  to compare calculations and performance of real devices. From the measured P-I and V-I characteristics the threshold current density and the area specific resistance of each device was calculated and is plotted in Figure 5.9 as a function of the waveguide width. Down to a width of  $2 \mu\text{m}$ , the  $J_{th}$  values of both chemistries follow a similar trend. Below this width, the data points belonging to the deeper waveguides (red colour) are highly scattered - due to cleaving problems that often occur on high aspect ratio waveguides. The  $J_{th}$  versus width plot of the half rings and the same plot of the different width FP lasers (see Figure 5.2) seems to be nearly identical. A more

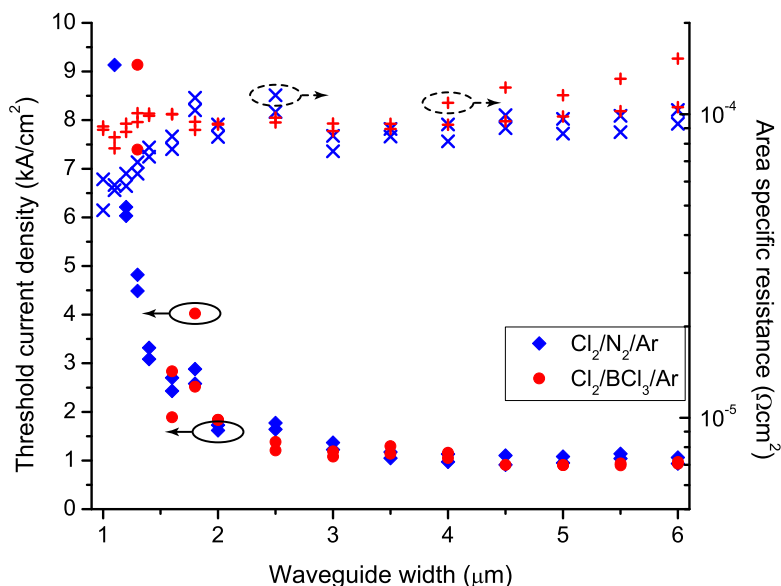


**Figure 5.9:** Measured threshold current density (rhombuses and circles) and area specific resistance (crosses) of  $20\ \mu\text{m}$  radius half ring lasers as function of the waveguide width. Blue coloured points belong to the  $\text{Cl}_2/\text{Ar}/\text{N}_2$  and the red coloured ones to the  $\text{Cl}_2/\text{Ar}/\text{BCl}_3$  etch.

careful inspection of these plots reveals that the measured  $J_{th}$  values of the half rings start to increase at  $100\ \text{nm}$  wider widths, i.e. the  $J_{th}$  curve is shifted to the right. This observation agrees well with the fact that the  $20\ \mu\text{m}$  radius bend increases the total cavity losses. Similarly to the FP devices, no kinks, which can be associated with the lasing of higher order transverse modes, could be observed below a waveguide width of  $3\ \mu\text{m}$ .

The key findings of this section, which are based on both simulations and experimental data, can be summarised as follows:

- Waveguides, which are etched at least  $\sim 2\ \mu\text{m}$  below the bottom of the core, have negligible bending losses down to a radius of  $3\text{-}4\ \mu\text{m}$
- Waveguides, which are etched at least  $\sim 1\ \mu\text{m}$  below the bottom of the core, have low bending losses down to a radius of  $6\ \mu\text{m}$
- A width of  $2\ \mu\text{m}\text{-}3\ \mu\text{m}$  is the best option for curved waveguides. This guarantees single transverse mode propagation, low surface recombination and low proportionate substrate losses.

## 5.4 Micro-ring and micro-disk lasers

The results of the previous sections provide a complete set of data to allow the design and fabrication of micro size SRL and semiconductor disk laser (SDL) devices. Figure 5.10 shows the general layout of four port SRL and SDL devices. As before, sections colored in red denote pumped waveguides, blue waveguides are passive and the yellow pads are the metal contacts. On the right side of the figure the magnified schematic of the lasing cavity and the coupling region is shown. Narrow-gap, 200-400 nm evanescent point couplers are used to tap the light of the cavity. Two, 10  $\mu\text{m}$  long contact windows are opened on the output waveguides, next to the point couplers to prevent dephasing of the output waveguides when current is injected into the rings or disks. To avoid the excitation of higher order modes and the excess heating of the junction, a circular, 1.6  $\mu\text{m}$  wide injection window is defined on the outer boundary in the disk cavity.

SDLs and SRLs with waveguide widths of 2  $\mu\text{m}$  and 3  $\mu\text{m}$ , and coupling gaps of 200 nm and 400 nm were fabricated with the aim of testing the device performance. The combination of these variations yields altogether six different device sets, the radius of which was varied from 120  $\mu\text{m}$  to 5  $\mu\text{m}$ . In order to test the effect of sidewall smoothness on SRL characteristics, two chips were processed in parallel with all fabrication steps being the same, but the dry etch etching. The  $\text{Cl}_2/\text{Ar}/\text{N}_2$  (3.1  $\mu\text{m}$  deep waveguides) and  $\text{Cl}_2/\text{Ar}/\text{BCl}_3$  (4.5  $\mu\text{m}$  deep waveguides) chemistries, that were detailed in Chapter 2, were used to etch the waveguides. Figure 5.11 shows the SEM image of a finished, 7  $\mu\text{m}$  radius disk laser and an even smaller, 6  $\mu\text{m}$  diameter SDL is shown in the inset of the figure.

P-I characteristics were measured with a large area photodiode and a thermoelectric cooler (TEC) was used to keep the back side temperature of the chip at a constant 20°C. Figure 5.12 plots  $J_{th}$  of the 400 nm coupling gap and 4.5  $\mu\text{m}$  deep devices as a function of the ring/disk radius. Room temperature, *cw* lasing was observed on both rings and disks down to a radius of 8  $\mu\text{m}$ . Due to the lack of the inner sidewall, SDLs suffer from current spreading, therefore only a part of the injected carriers contributes to the stimulated emission of the fundamental mode. In order to account for the spreading the  $J_{th}$  of the micro-disks is calculated for a 3  $\mu\text{m}$  wide circular area. The comparison of the different large radius rings shows, as expected, that the 2  $\mu\text{m}$  wide waveguide rings start lasing at a  $\sim 1.3$ -1.4 times

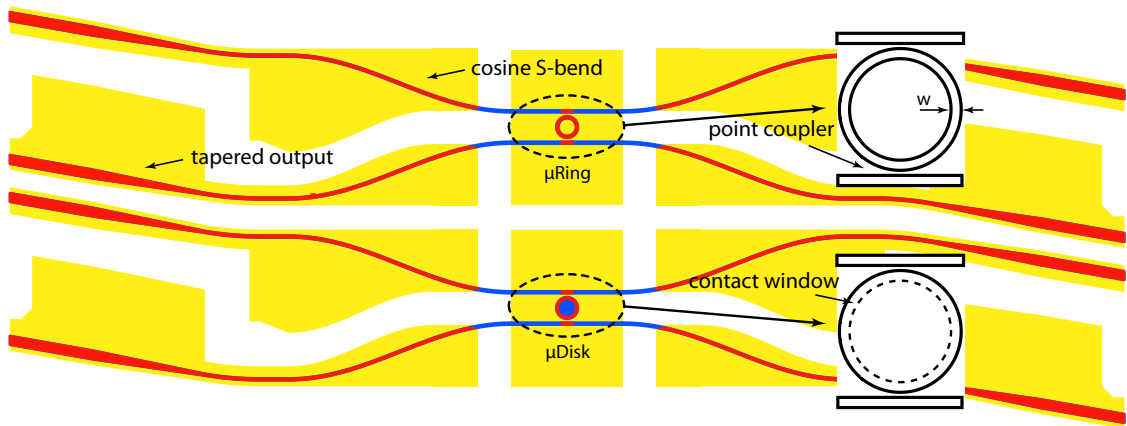


**Figure 5.10:** Schematic of fabricated ring (top) and disk (bottom) shape ring laser devices.

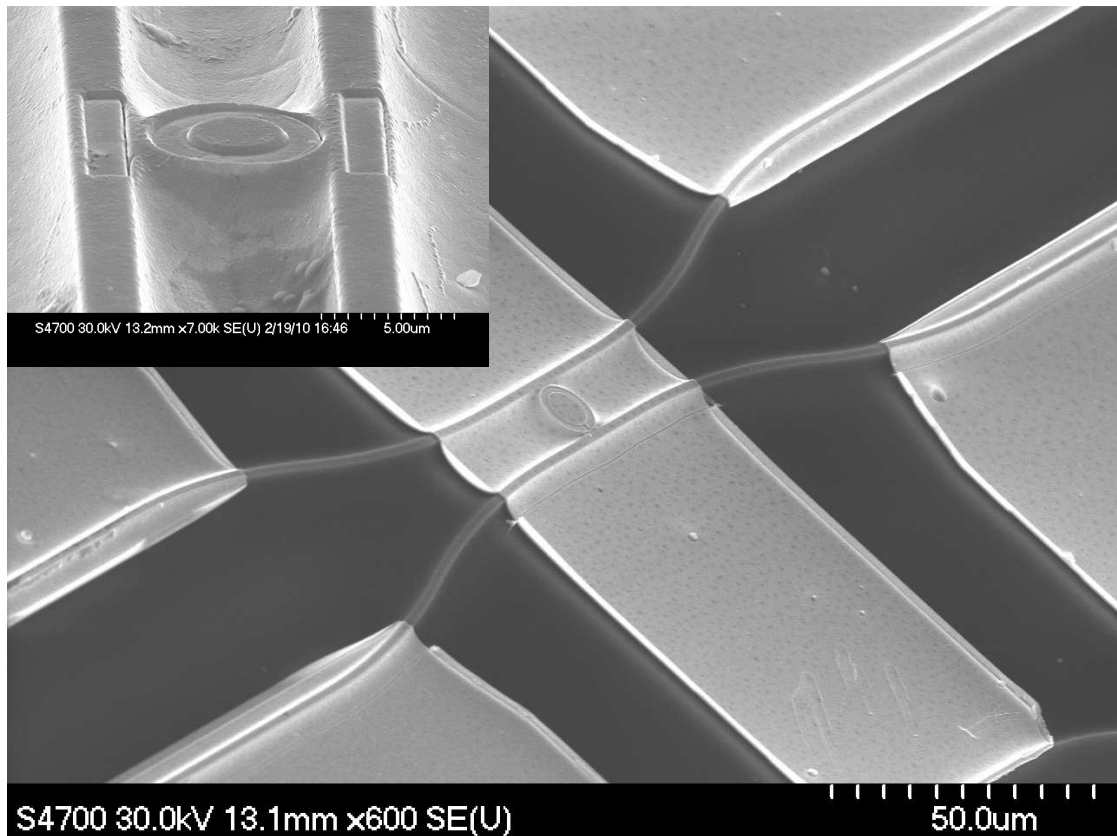


**Figure 5.11:** SEM photograph of a 7 μm radius SDL. The inset shows a close up of a 6 μm diameter micro-disk.

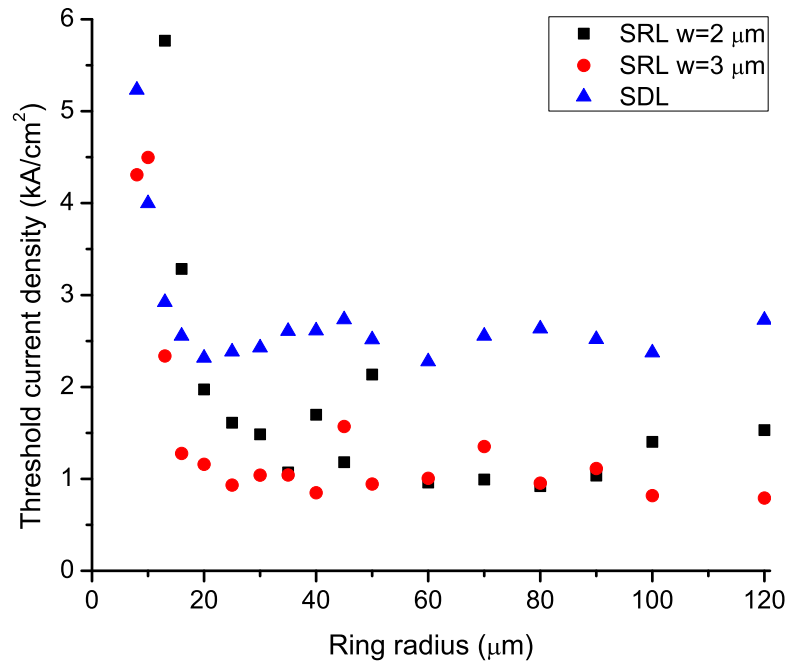


**Figure 5.12:** Measured threshold current density of micro-SRLs and SDLs as a function of the device radius. Devices etched with the  $\text{Cl}_2/\text{Ar}/\text{N}_2$  chemistry to an etch depth of  $3.1 \mu\text{m}$  show very similar characteristics and are not reported in the section.

higher  $J_{th}$  values than the  $3 \mu\text{m}$  wide waveguide rings. For the small radius devices a strong increase of threshold can be observed below a radius of  $20\text{--}25 \mu\text{m}$  for the  $2 \mu\text{m}$  wide rings and below  $16 \mu\text{m}$  for the disks and the  $3 \mu\text{m}$  wide rings. Such an increase is unexpected in the light of the previous waveguide and bending loss measurements of Section 5.1 and 5.3. The remaining part of the section analyses the reasons of this unforeseen loss increase of the small radius SRLs and SDLs.

#### 5.4.1 Junction heating in small SRL devices

A possible explanation for such a threshold increase may be a stronger junction heating as the device size reduces. In order to confirm this hypothesis the series resistance ( $r_s$ ) of the SRLs was derived from the measured  $V$ – $I$  characteristics, and it is plotted in Figure 5.13 as a function of the device radius. The calculated resistance values of the diode (dashed, dotted and dash-dotted lines) show a good agreement with the experiment, although resistance values are slightly shifted

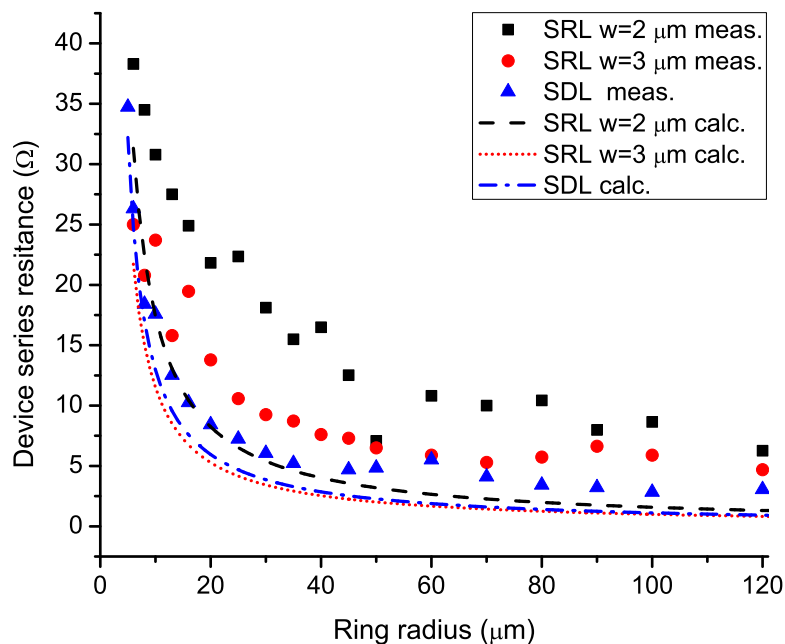


**Figure 5.13:** Measured and calculated series resistance of micro-SRLs and SDLs as a function of the device radius.

downwards with respect to the measured data (square, circle, triangle) because of the additional resistance of the instrument leads and the n-type contact. The analysis of the device resistance revealed that the two main contributing factors responsible for the high  $r_s$  of a short laser are the resistance of the upper cladding ( $r_{cl}$ ) and the p-type contact resistance ( $r_c$ ). As a consequence the major part of the dissipated heat is generated in the upper cladding and so directly heats the junction of the diode. When tested under pulsed-current condition devices showed the same lasing (or non-lasing) than under *cw* bias. This indicates that Joule-heating is not responsible for preventing the lasing action on small devices. Moreover, the P–I characteristic of the small radius SRLs was re-measured at a Peltier temperature of 0°C and devices showed a 1-2 mA lower  $I_{th}$ . Furthermore, the minimum radius at which lasing occurs decreased to 6 μm. As an example, Figure 5.14(a) plots the 20°C and 0°C P–I characteristic of a 10 μm radius and 2 μm wide SRL. Although the device has a high, 8.5 kA/cm<sup>2</sup> threshold current density it exhibits *cw* lasing with a current threshold of 12 mA. Above 20 mA (14 kA/cm<sup>2</sup>) the signs of thermal roll-off can be observed on the slope of the P–I curve. The

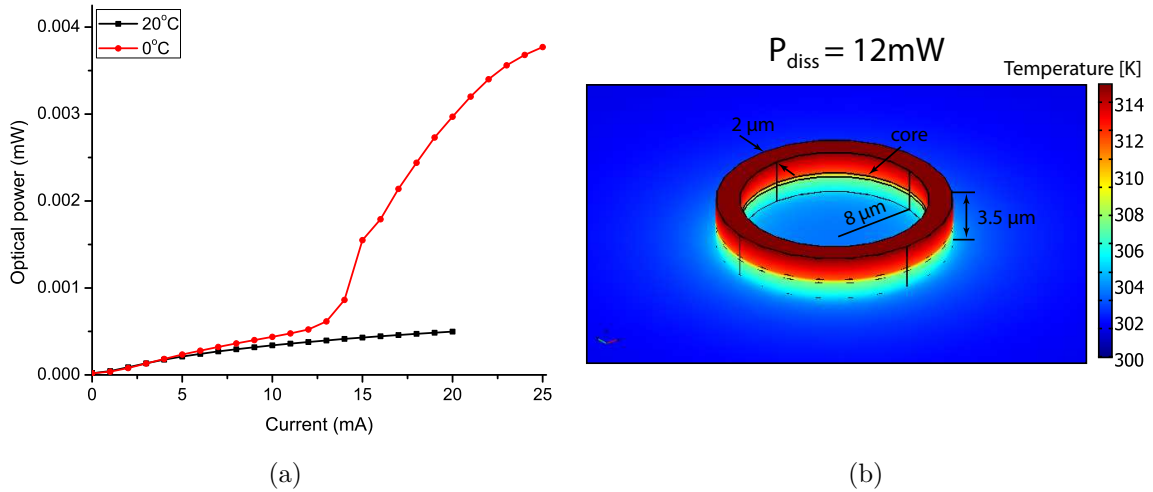


**Figure 5.14:** (a) P–I characteristic of a  $10\ \mu\text{m}$  radius SRL recorded at  $20^\circ\text{C}$  and  $0^\circ\text{C}$ . (b) Simulated isothermic colourmap of the same micro-ring for  $12\ \text{mW}$  dissipated power.

latter indicates that the thermal degradation of the gain becomes only significant at high device currents (i.e. above  $14\ \text{kA}/\text{cm}^2$ ), and therefore confirms that this can not be responsible for the termination of lasing of the small radius devices. To validate this observation and to quantify the temperature rise of the junction, thermal calculations were carried out. Heat generated in the upper cladding can either flow through the waveguide core and lower cladding toward the Peltier plate cooled back side or it can flow through the cap layer to the p-type metallisation. Since the cooling of the top contact by convection is negligible, only the conductive heat paths have to be considered (i.e. the heat flowing towards the back contact). The thermal conductivity ( $\sigma_{th}$ ) of indium phosphide is  $68\ \text{KW}^{-1}\text{m}^{-1}$ , and the InGaAs cap and the InGaAlAs core layers have a  $\sim 8$  times lower average thermal conductivity than InP [94,95]. Although InP conducts heat very well, the narrow cross section of the waveguide can form a considerable thermal resistance ( $r_{th}$ ). For example, the  $r_{th}$  of the lower cladding and the core of a  $10\ \mu\text{m}$  radius,  $2\ \mu\text{m}$  wide and  $3.2\ \mu\text{m}$  deep etched ring is  $\sim 120\ \text{KW}^{-1}$  and  $\sim 340\ \text{KW}^{-1}$ , respectively. These figures translate into an approximate half degree temperature increase of the core layers per every dissipated milliwatt. Calculations were checked with a commercially available finite element method (FEM) solver, *Comsol*<sup>1</sup>. Figure 5.14(b)

<sup>1</sup><http://www.comsol.com/>

plots the heat distribution map of the  $10\ \mu\text{m}$  radius SRL of the previous example for a  $12\ \text{mW}$  dissipated heat (equivalent to a  $20\ \text{mA}$  flowing through  $r_s=30\ \Omega$ ). A good agreement was found between the simple resistor ladder model and the FEM technique. There is only a small  $1\text{-}2^\circ\text{C}$  difference between the two results, which is the result of neglecting the  $r_{th}$  of the substrate in the concentrated parameter calculations. The evaluated thermal properties of SRLs show that material gain degradation due to junction heating becomes observable above a dissipated power level of  $20\text{-}25\ \text{mW}$  (e.g.:  $20\ \text{mA}$  flowing through a  $50\ \Omega$  resistor). Such dissipation levels are only present in the high series resistance sub- $10\ \mu\text{m}$  diameter devices or they can be achieved through a very strong pumping of larger SRLs (higher than  $18\ \text{kA}/\text{cm}^2$ ). Therefore the increased  $J_{th}$  of SRLs and SDLs with radii smaller than  $20\ \mu\text{m}$  can not be explained with thermal gain degradation.

#### 5.4.2 RIE-lag effects in small SRL devices

A second possible cavity dampening mechanism that scales with the curvature and so with the device size, is the bending loss. Measured data indicates that the signs of increasing losses become visible below the radius of  $16\ \mu\text{m}$ . Assuming that the extra losses are the result of bending losses would contradict the results of Section 5.3. Fortunately this is not the case: so far all SRL bending loss analysis was based on ideally etched ring and disk cavities (i.e. the etch depth is the same around the circumference), but this is not true anymore when couplers are included in the geometry. Referring back to Fig. 2.13 and Fig. 2.16 in Chapter 2, one can observe that the etch depth of the cavity is not constant, since the height of the rings and disks is reduced in the point coupler region as the result of the RIE-lag effect. SEM inspections show that this shallower etched region can accommodate as much as  $20\%$  of the total cavity circumference in small ring cavities. The increased roundtrip bending losses of the ring due to non-uniform etch depth provide a valid explanation for the unexpected threshold increase of the experimental data of the devices with radii smaller than  $20\ \mu\text{m}$ .

The presence of the RIE-lag explains a second observation, namely that below a device radius of  $20\ \mu\text{m}$  (independent of the etch chemistry used) no unidirectional bistability could be observed neither in rings nor in disks. A detailed explanation of this phenomenon is as follows: the modal mismatch caused by the shallower etched

parts of the point coupler induces back-reflections. The slope of the lag becomes steeper with decreasing radius, thus the coupling between the counter-propagating modes increases and the directional extinction decreases. Below the critical radius of  $20\ \mu\text{m}$  bistability completely vanishes due to high back-reflection levels and only bidirectional lasing could be observed.

## 5.5 Coupler design

Due to the low coupling strength of deeply etched point couplers, only a few micro watt optical power can be collected from their outputs with a fiber lens. Such power levels are sufficient for designing coupled ring devices, but these SRLs are inadequate for applications in a telecommunication system. In order to tackle low output power problems, cavity geometries, that offer the possibility of integrating small bends and reasonably strong couplers, should be employed. Such a design is the deep etched racetrack geometry.

In order to realise micro-SRLs not only the length of the curved waveguides but also the size of the cavity coupling region must be reduced. From the three coupler types discussed in the previous chapter (see Section 4.3), only MMI couplers and directional couplers will be discussed here. Deep etched Y-junction couplers are excluded from this discussion due to the large back reflection that originates from their branching point. In the following paragraphs the issues related to the size reduction of these two coupler types are discussed.

Figure 5.15(b) shows the schematic of a general-interference MMI coupler with tapered access waveguides, which does not contain any surfaces perpendicular to the propagation direction of the light. With this layout reflections can be kept at a minimum and possible internal resonances of the structure are avoided. The length of a 3 dB coupler scales quadratically with the width of the MMI region [78], more specifically:

$$L_{3dB} = 2n_e W_m^2 \lambda_0, \quad (5.3)$$

where  $n_e$  is the effective index of the interference region,  $W_m$  is the width of the MMI coupler and  $\lambda_0$  is the free space wavelength. BPM simulations were performed to find the  $L_{3dB}$  as a function of the width for this material. The width of the access waveguides was set at one third of  $W_m$  and was scaled proportionally

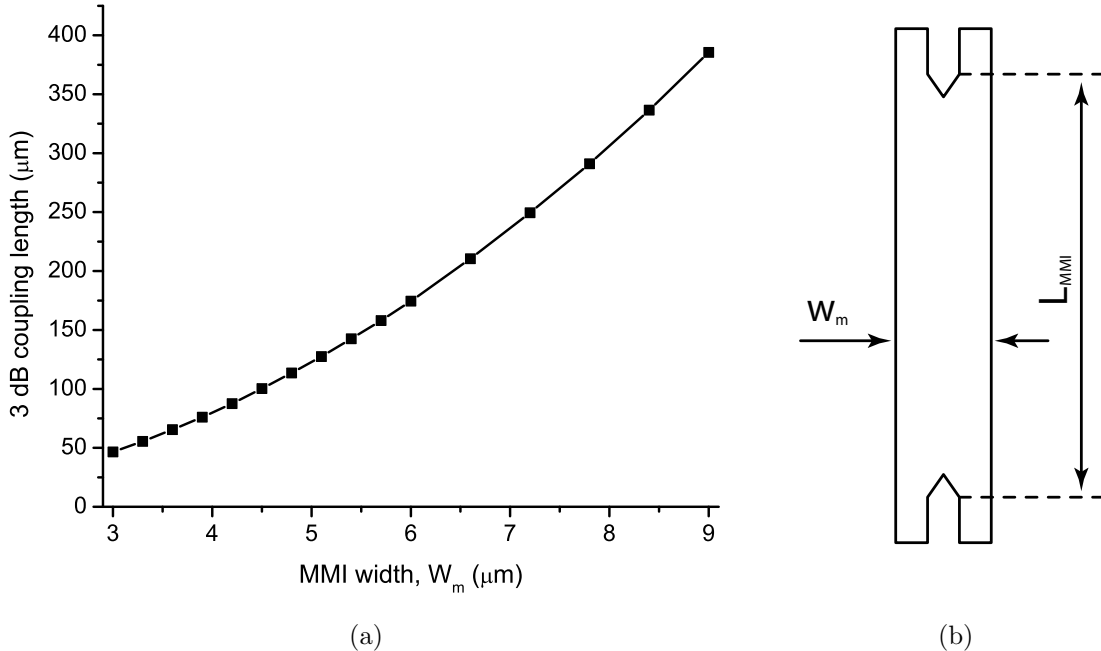


**Figure 5.15:** (a) Simulated 3 dB coupling length as a function of the width of the MMI coupler's interference region. (b) Schematic of a general-interference MMI coupler.

with the size of the structure. Results are plotted in Figure 5.15(a) and predict a beating length of  $46.5 \mu\text{m}$  for a  $W_m$  of  $3 \mu\text{m}$ . It is not advisable to reduce  $W_m$  below  $2.8\text{--}3 \mu\text{m}$ , since the self imaging in the interference region is not supported anymore as the first order mode is nearly at cut-off at these widths. Even the narrowest,  $3 \mu\text{m}$  wide, general interference MMI coupler is far too long if one wants to realize short racetrack cavities. A two to three times size reduction can be achieved by tapering the shape of the multimode region [96, 97], as illustrated in Figure 5.16, which means that the length of the device reduces to  $\sim 15 \mu\text{m}$ . An MMI coupler with this size is small enough to be part of a micro-SRL, but two serious design problems limit its applicability to SRL cavities. First, an adiabatic taper has to be introduced between the access waveguides of the MMI and the wider curved segments in order to maintain low losses and reflections. Second, as already mentioned in Section 4.3, the multimode region must be kept passive in order to avoid the increase of reflections caused by the detuning effect of the injected carriers. It is an unaffordable luxury to leave the interference region unpumped, as this would

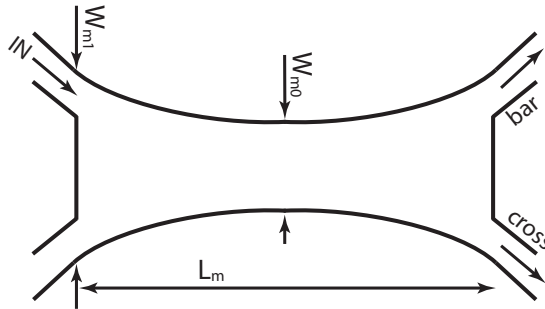


**Figure 5.16:** Schematic of a parabolically tapered MMI coupler.

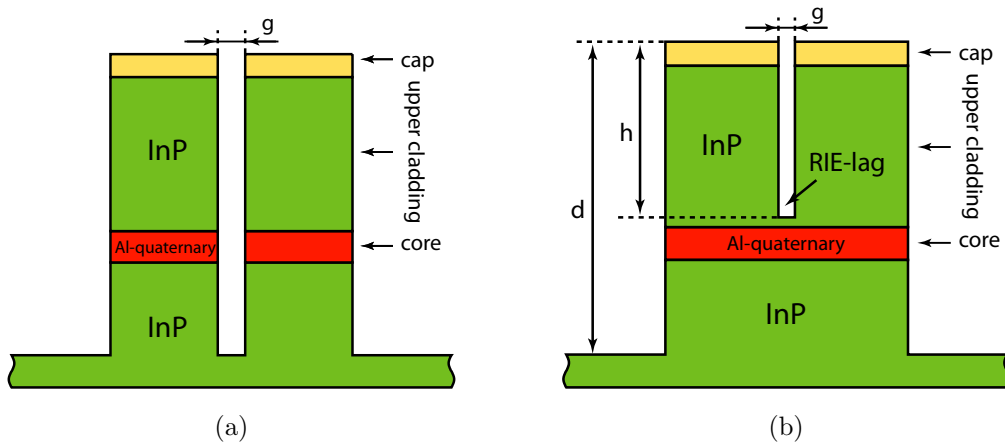


**Figure 5.17:** Cross section of a deep etched evanescent coupler, where (a) the separation has the same depth as the external trench (b) the gap shape is more realistic, it suffers from RIE lag.

drastically increase the threshold current density. It can be concluded that the requirement to keep the multimode region passive makes this geometry an inadequate candidate to construct miniature micro-SRL devices.

A second alternative to tap the light of an SRL cavity is the directional coupler. The beating length of a directional coupler scales with the waveguide width and the coupling gap ( $g$ ) [81]. Figure 5.17(a) shows the cross section of an “ideal” deeply etched evanescent field coupler. Both the gap and the trenches are etched through the core layers and well into the lower cladding. The 100% coupling length of this structure type was computed as a function of the width of the coupler gap ( $g$ ) and is plotted in Figure 5.18. The extremely long beating length of these couplers is the

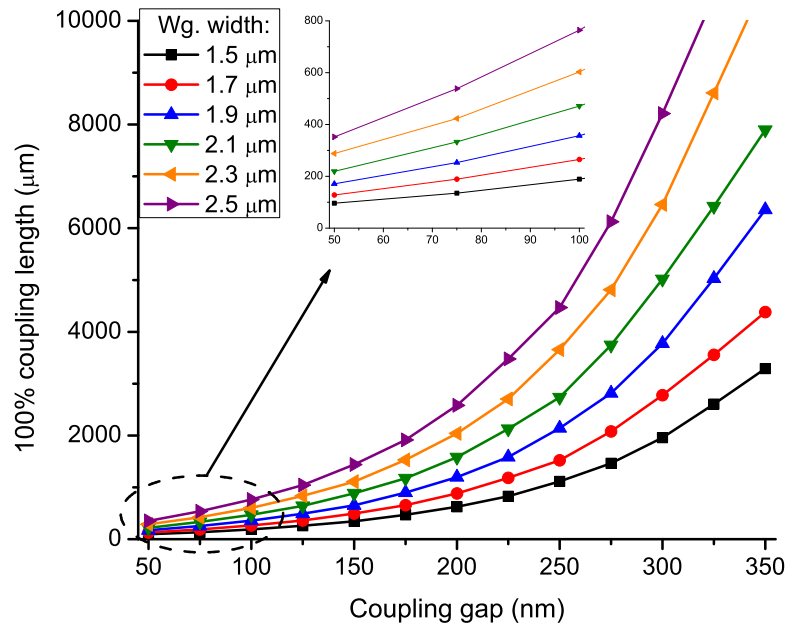


**Figure 5.18:** Simulated beating length of an “ideal” deep etched evanescent coupler as a function of the separation distance with the waveguide width as a parameter.

result of the very weak overlapping field in the air gap of the two parallel waveguides. To achieve reasonably short beating lengths a 50-100 nm wide and a  $> 2.5 \mu\text{m}$  deep separation gap should be fabricated between two 1-1.5  $\mu\text{m}$  wide waveguides<sup>2</sup>. The measured RIE lag data of Fig. 2.15 (page 30) clearly shows that gaps narrower than 300 nm can not be etched below the core with the standard lithographic and etching techniques developed in Chapter 2. The schematic of Fig. 5.17(a) is an ideal situation which does not reflect the real etching profile. A more correct analysis should account for the RIE lag effect, such as the more realistic cross section shown in Figure 5.17(b). The displayed structure is neither a directional nor a MMI coupler. Both two-mode coupling characteristics and multimode interference effects can be observed in these devices [98], and depending on the etch depth of the separation gap ( $h$ ) one or the other coupling effect dominates. Figure 5.19 plots the power distribution of the bar and cross waveguides as a function of the propagation distance for different etch depth values of a 400 nm gap between two 2  $\mu\text{m}$  wide waveguides. The evolution from an interference based coupling, Fig. 5.19(a), to the power transfer via the evanescent field, Fig. 5.19(f), can be observed as the gap

<sup>2</sup>This is impossible with today’s RIE tools.

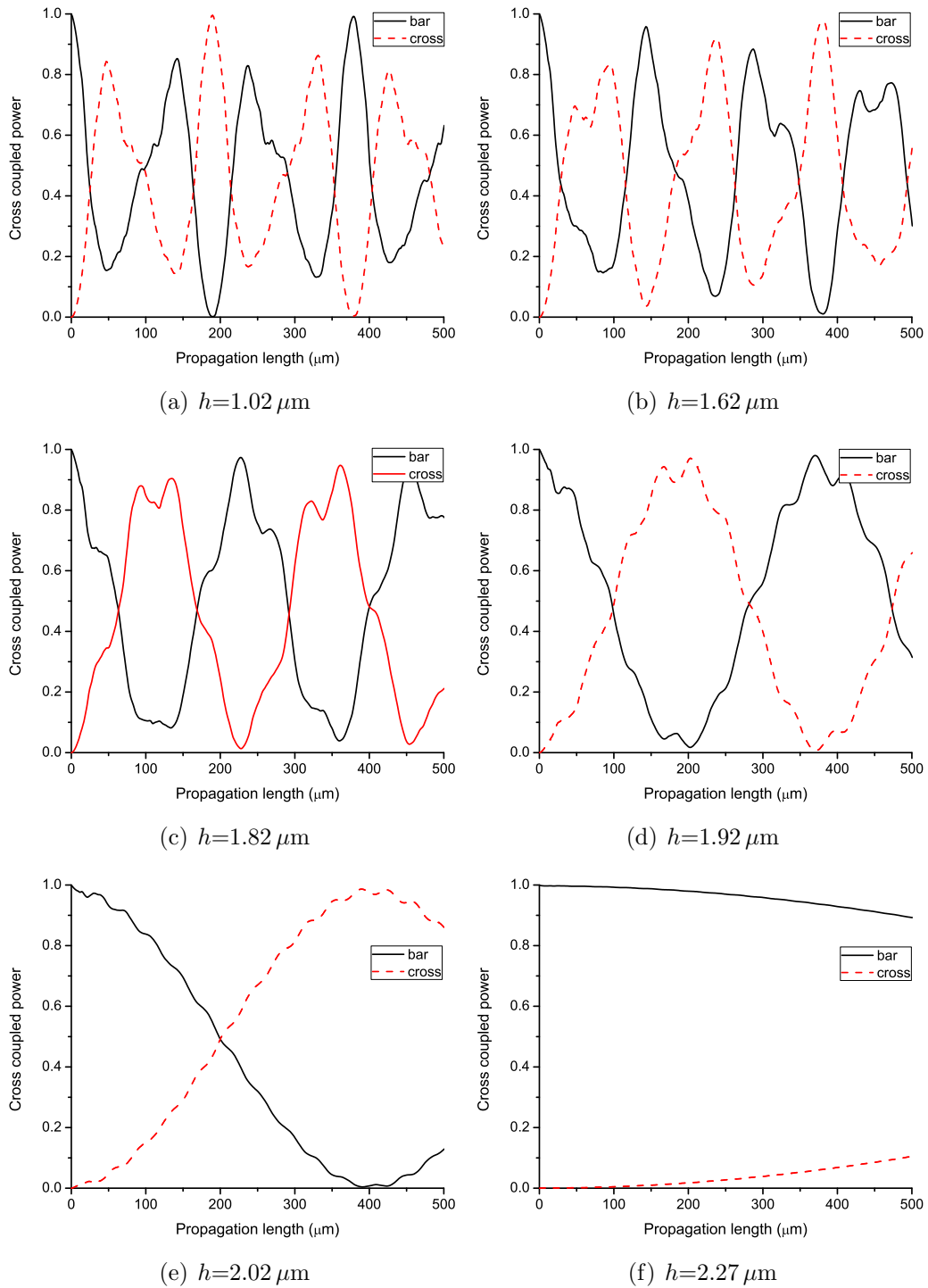


**Figure 5.19:** Power distribution as a function of the propagation distance for various gap etch depths. The waveguide parameters  $g$  and  $d$  were set to  $400 \text{ nm}$  and to  $3.26 \mu\text{m}$ , respectively.

becomes deeper. With increasing etch depth the ripples of the transferred power, which are caused by the interference effect, reduce, and when the top of the core is reached ( $h=1.92\ \mu\text{m}$ ), Fig. 5.19(d), only a 10% modulation is visible. A further 100 nm etching ( $h=2.02\ \mu\text{m}$ ) results in an almost undulation free evanescent power transfer, but this comes at the cost of a doubling the beating length. The coupling length increases steeply as the gap is etched deeper into the core and at the bottom of the core ( $h=2.27\ \mu\text{m}$ ) it is already  $\sim 2400\ \mu\text{m}$ , Fig. 5.19(f). It is clear that a trade off has to be made between short coupling length and reasonably small modulation. Moreover, the etching depth tolerance of the chemistry used has to be considered in order to estimate the deviation from the design. An ideal racetrack geometry would consist of deeply etched waveguides ( $d > 4.5\ \mu\text{m}$ ) to ensure low bending losses and an evanescent coupler with a gap etched down to the core layer ( $h=1.92\ \mu\text{m}$ ) for strong out-coupling. Based on the previously measured RIE lag data, a gap width of 300 nm was selected and the etching time was optimised in order to etch the gap to a depth of  $1.92\ \mu\text{m}$ . Such a bi-level directional coupler, which consists of two  $2\ \mu\text{m}$  waveguides and a 300 nm gap, has a  $\kappa$  of 4% and 10% for lengths of  $10\ \mu\text{m}$  and  $20\ \mu\text{m}$ , respectively. Though these coupler strengths appear rather weak, one must also consider that short cavities have a higher differential efficiency ( $\eta_d$ ) than long cavities for the same coupler strength. Figure 5.20 plots  $\eta_d$  as a function of the out-coupled power:  $10\ \mu\text{m}$  and  $20\ \mu\text{m}$  radius SRLs with a  $\kappa$  of 10% have efficiencies as high as 30-40%. As a comparison, a 1 mm long cavity needs a  $\kappa$  of 70% to reach similar  $\eta_d$  values. If required, a further decrease of the beating length can be achieved by reducing the waveguide width in the coupler section. For example, a  $10\ \mu\text{m}$  and a  $20\ \mu\text{m}$  long bi-level coupler consisting of  $1.5\ \mu\text{m}$  wide waveguides has a power coupling of 9% and 23%, respectively.

The excellent repeatability of the previously described etch chemistries (see Chapter 2.4.2) allows to control the depth inside of the gaps with a  $\pm 50\ \text{nm}$  accuracy, by relying solely on the calibration data of after etch trench depth measurements<sup>3</sup>. Such a small variation of gap depth changes the designed coupling value by as much as  $\pm 40\text{-}50\%$ . A more accurate control of the separation depth can be achieved by introducing an etch stop layer into the epitaxial stack [27]. With this technique the accuracy of the etch improves to at least  $\pm 5\ \text{nm}$ , which corresponds

<sup>3</sup>Unfortunately no other in situ depth monitoring methods were available on the ICP RIE machine.

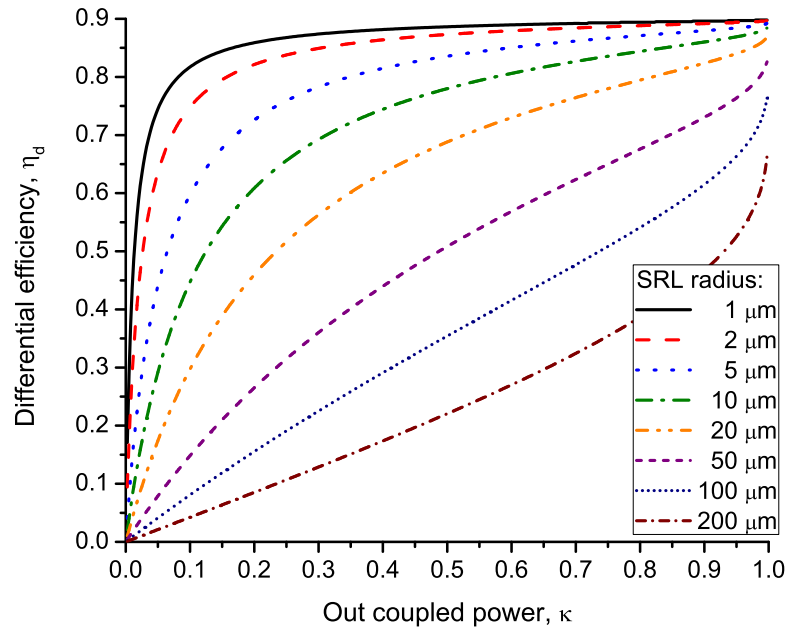


**Figure 5.20:** Calculated differential efficiency as a function of the out-coupled power with the SRL radius as a parameter.

to a design accuracy of few percent. Introduction of an etch stop layer would have required the complete re-design of the wafer epitaxy, which is outside of the scope of this work.

## 5.6 Adiabatic, low reflection transitions

The curvature discontinuity of two connected waveguide causes a mismatch of the optical field along the waveguide path. Abrupt, stepwise curvature changes, such as transitions between straight and bent waveguides, create both radiation losses and back reflections that become increasingly lossy (and back-reflecting) as the mismatch increases [99]. In a racetrack shaped SRL cavity four such discontinuity points can be found between the two half-circles and the two straight sections. As the device size decreases the elevated back reflection from the mismatched interfaces increases the coupling between the CW and CCW directions, which may prevent unidirectional bistability. The optical field distribution maps shown in Fig. 5.1(a) (p. 66) and Fig. 5.8 (p. 74) illustrate the problem well: the outward shifted and

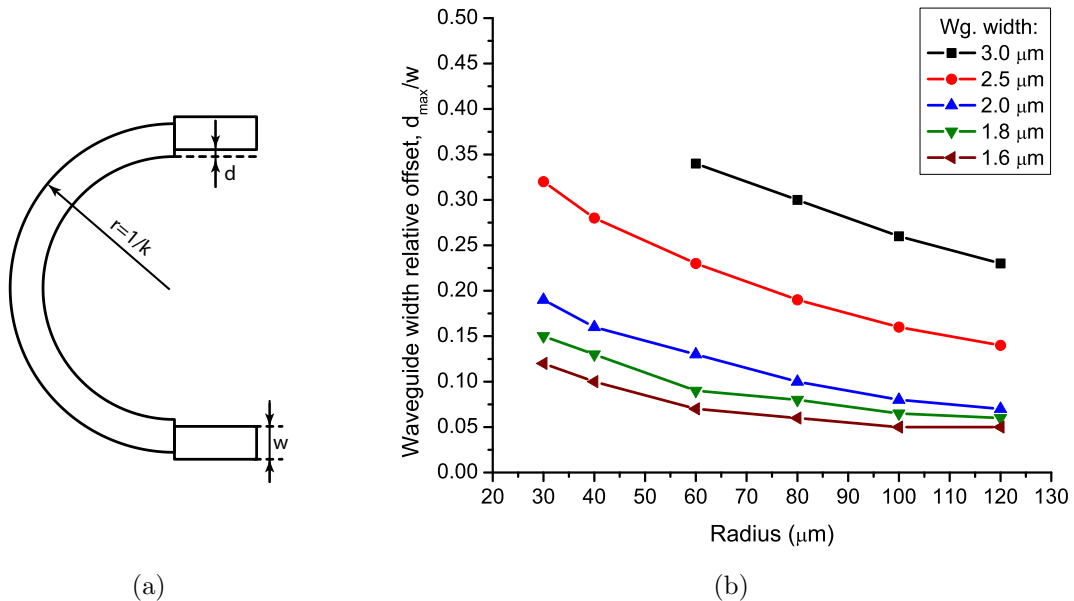


**Figure 5.21:** (a) Schematic illustrating the waveguide offset, which aims to minimise the transition loss between a curved and a straight waveguide. (b) Calculated offset values, where the power transfer is maximal, as a function of the waveguide radius with the waveguide width as a parameter.

asymmetric optical field of the curved section does not match the field of a straight guide.

A solution to this problem is based on the idea that at the transition the overlap of the optical fields should be maximised by offsetting the curved and straight waveguides by an amount ( $d$ ) proportional to their mode offset [100], as illustrated in Figure 5.21(a). BPM simulations were carried out to find the displacement values, at which the power transfer is maximal ( $d_{max}$ ). Results, shown in Figure 5.21(b), plot the width ( $w$ ) normalised  $d_{max}$  as a function of the radius. It can be seen that the relative displacement of the waveguide ( $d_{max}/w$ ) increases with decreasing bending radius, as a result of the outward shift of the optical mode, and that  $d_{max}/w$  decreases as the waveguide width becomes smaller. The latter trend is the consequence of the less deformed mode field of a narrower waveguide that results in a better overlap with the mode of the straight guide.

A drawback of this mismatch compensation approach is that the offset at the interface is an abrupt transition, therefore cannot realise a perfect matching. More-

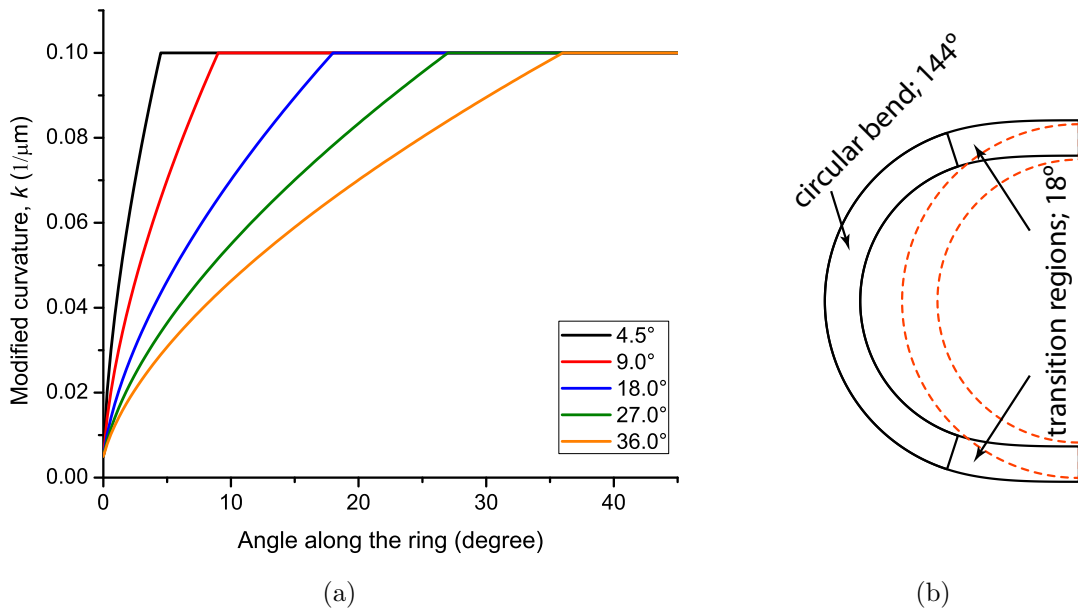


**Figure 5.22:** (a) Calculated curvature of an adiabatic transition segment as a function of the angular length. Each curve corresponds to a different transition length. (b) Schematic of a  $10\ \mu\text{m}$  radius adiabatic bend, black line. A conventional  $10\ \mu\text{m}$  radius half circle was plotted with dashed, red line for comparison.

over, as the radius of the curved part decreases, the modal mismatch increases and so does the back reflection of these shifted interfaces. Both problems make this mode matching strategy unsuitable to be applied for small radius, racetrack-shaped SRLs.

A better and more sophisticated approach, which creates an adiabatic power transfer, is based on a continuous curvature ( $k=1/r$ ) change between the straight and the curved sections. Most designs found in the literature join the two parts with a transition section of linearly increasing curvature [101,102]. The light propagating along a small curvature/ large radius waveguide ( $w \ll 1/k$ ) experiences a linear outward shift of the mode with increasing curvature. In case of large curvature bends, the modal shift becomes super-linear (faster than linear), therefore the transition region has to be optimised to follow the evolution of the mode correctly. A possible strategy is to vary  $k$  so that a constant change of  $n_{eff}$  is attained along the transition. The dependence of the effective refractive index on the bending radius was already computed in Section 5.3. In order to acquire the continuous ex-

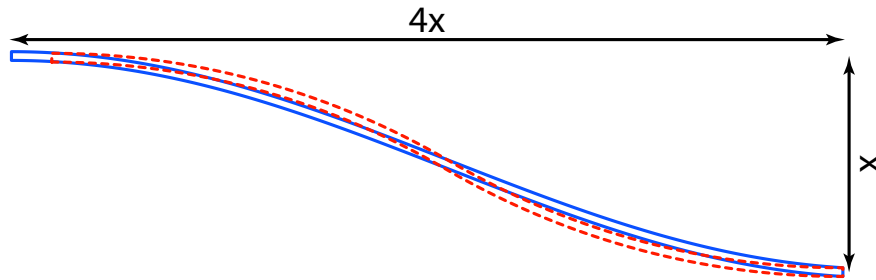


**Figure 5.23:** Schematic of a cosine shape S-bend (blue line) and that of a conventional S-bend (dashed, red line).

pression  $n_{eff}(r)$  from the discrete set of data, a  $y=a*x^b+c$  type equation was fitted to the simulated data points. Then this relation was used to convert the linearly changing  $n_{eff}$  to a curvature variation. As an example, the curvature transition from a straight waveguide to a  $10\ \mu\text{m}$  radius circle is shown in Figure 5.22(a), in which lines plotted with different colours correspond to different angular lengths. Compared to the linear curvature change, this design has a bigger curvature gradient at the beginning and a smaller at the end of the transition. The validity of this approach can be confirmed by comparing the calculated curvature gradient to the previously simulated modal displacement data of Fig. 5.21(b). Both curves show a very similar tendency: as the radius decreases the modal deformation changes faster, therefore a larger displacement change is required per unit radius change. Based on this algorithm a C++ macro was developed with the aim of automating the high resolution layout generation of the adiabatic bends. Such a  $180^\circ$  bend is plotted with a black line in Figure 5.22(b), consisting of a  $144^\circ$  circular part with a  $10\ \mu\text{m}$  radius and two  $18^\circ$  transition regions. Compared to a conventional half bend the total length of this curve is increased by 26%. As the radius of the circular part is reduced to a few microns the proportional length of the transition increases, therefore attention must be paid to find a good compromise between the angular length of the transition and the total length increase of the structure.

SRLs with two output buses are often required with an output waveguide spacing that matches the pitch of a standard  $250\ \mu\text{m}$  fiber array. The S-bend geometry is often used to connect the waveguides and to provide the required lateral offset at the cleaved facets. Similarly to what was discussed previously, designs have to address the mismatch of the straight to curved transitions at the two ends and

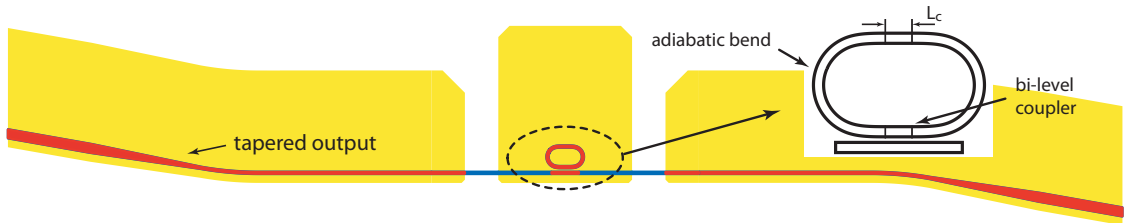


**Figure 5.24:** Schematic of racetrack shape SRL devices.

at the curvature reversal in the centre of the S-bend. The two most commonly used approaches, which reduce the transition losses, are based on cosine or sine curves [103] and on polynomial curves (P-curves) [100]. Cosine based S-bends were chosen for the design of SRL devices, despite the fact that their loss performance is slightly worse than P-curves. Their simple analytic form is advantageous, since it allows automated layout generation. Figure 5.23 plots a cosine shape S-bend (blue line), which connects two points with a horizontal to vertical distance ratio is 4 to 1. For comparison a conventional S-bend made of two arcs is plotted in dashed red line.

## 5.7 Racetrack shape micro ring lasers

Based on the design consideration of the previous sections, racetrack-shape SRLs were designed, whose general layout is shown in Figure 5.24. Each racetrack consists of two adiabatic bends and two straight waveguides with a bi-level etched coupler. Both curved and straight parts were designed to have a width of  $2\ \mu\text{m}$ . The bending radius of the fabricated SRLs was varied from  $50\ \mu\text{m}$  to  $10\ \mu\text{m}$  with a step of  $10\ \mu\text{m}$  and the coupling length ( $L_c$ ) was designed to be  $5, 10$  or  $15\ \mu\text{m}$ . The SEM image of fabricated racetrack-shape micro-SRLs is shown in Figure 5.25. As an example, Figure 5.26 plots the optical output powers of a  $10\ \mu\text{m}$  radius racetrack with an  $L_c$  of  $5\ \mu\text{m}$  and  $10\ \mu\text{m}$  as a function of the injected current. The output waveguide contacts were left unbiased, which means that the power levels at the device outputs can be further increased by 10-13 dB by biasing the bus waveguides to transparency. The evaluated threshold current density of the SRLs is between  $1.2\text{-}2.4\ \text{kA}/\text{cm}^2$ . Small radius devices have slightly larger  $J_{th}$  values, which is most likely the result of the higher coupling losses per unit length. The optical spectrum

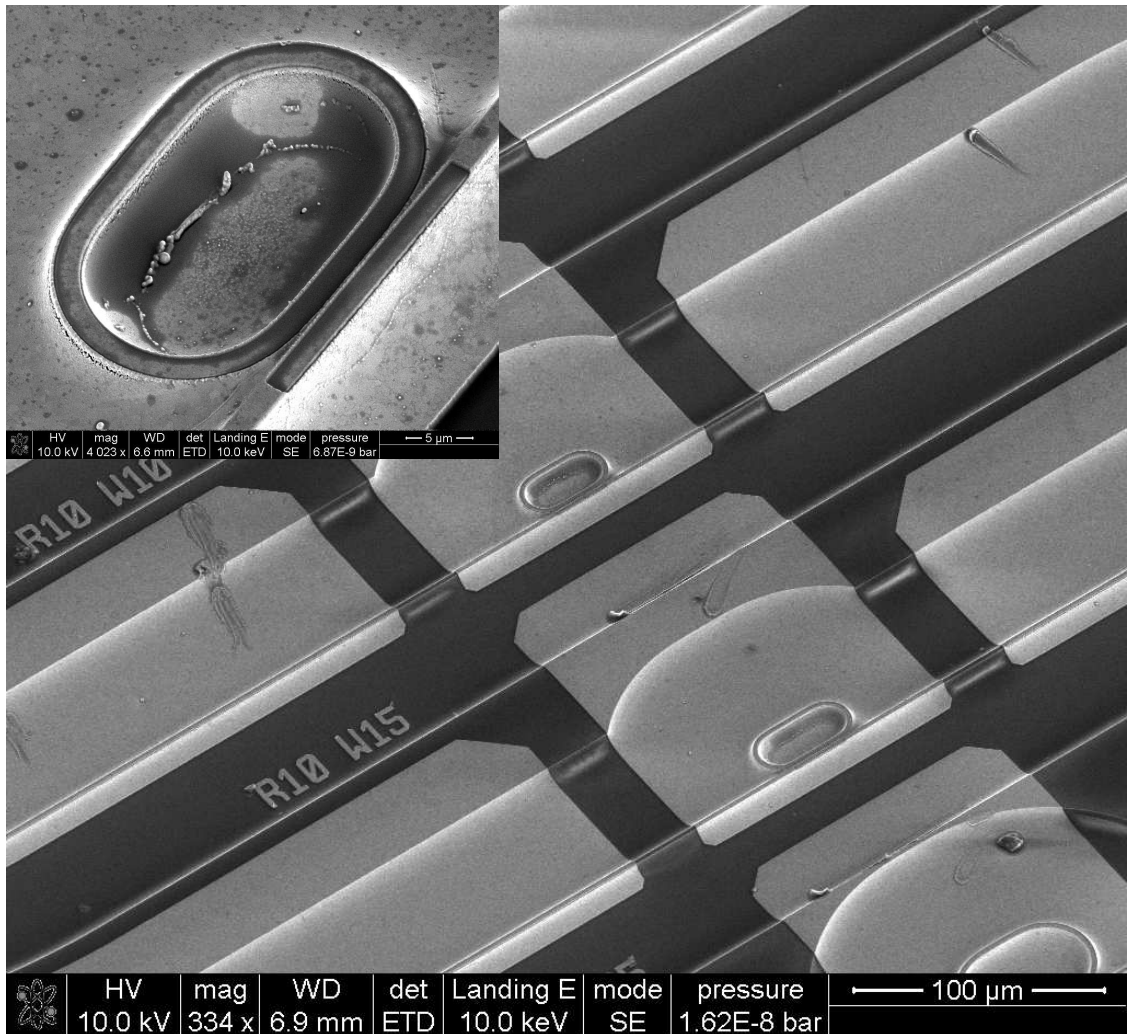


**Figure 5.25:** SEM photograph of racetrack-shape 10 μm radius SRLs. The inset shows a close up of an SRL consisting of a 10 μm radius adiabatic bend and 5 μm long coupler.

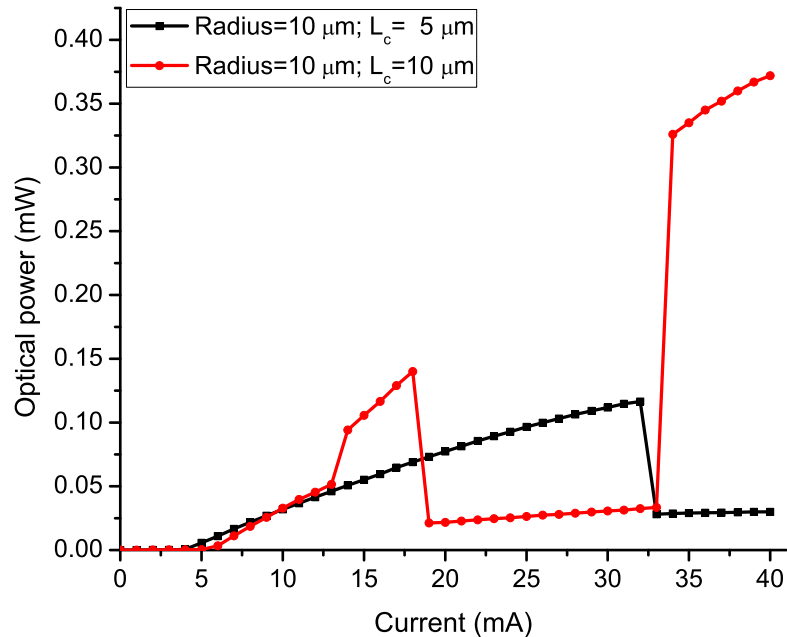


**Figure 5.26:** Recorded P–I characteristics of a 10  $\mu\text{m}$  radius racetrack SRLs with coupling lengths of 5 and 10  $\mu\text{m}$ .

of the devices were measured with fiber lenses aligned to each output. The spectra of a 10  $\mu\text{m}$  radius and 10  $\mu\text{m}$   $L_c$  racetrack at 40 mA bias current show a DER of 18 dB and an SMSR of 27 dB. It was observed that above 1.2-1.5 times  $J_{th}$  all devices show robust unidirectional bistable operation with  $\sim 20$  dB DER and  $\sim 30$  dB SMSR. An interesting finding of the spectral measurements is that racetracks fabricated with a smooth sidewall (etched with  $\text{Cl}_2/\text{Ar}/\text{BCl}_3$  chemistry) have a higher DER than the devices with a rough sidewall (etched with  $\text{Cl}_2/\text{Ar}/\text{N}_2$  chemistry). The reason for the degradation of the unidirectional operation is the stronger coupling of the counter-propagating modes due to the higher backscattering from the more rough waveguide sidewalls. This result confirms once more the huge impact of sidewall quality in deeply etched SRL devices and justifies the optimisation of the fabrication processing developed within this work.

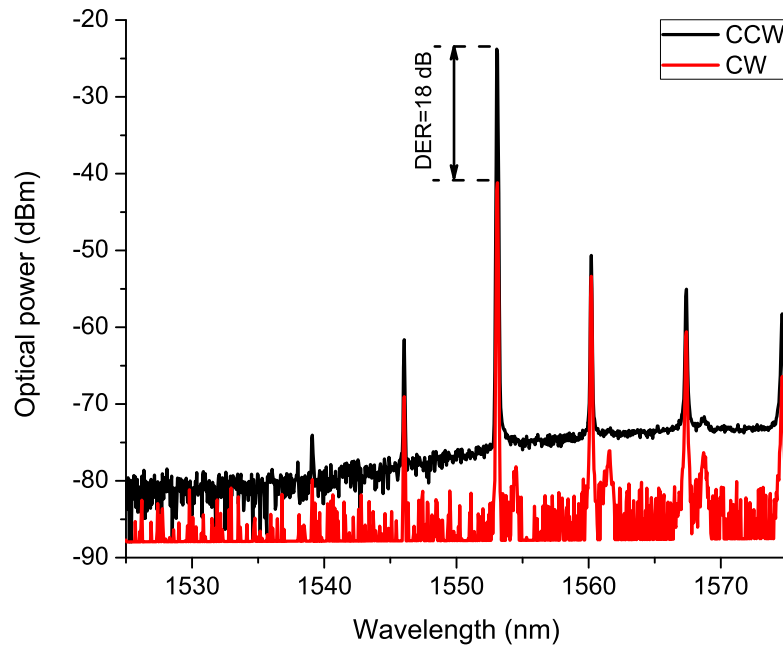


**Figure 5.27:** Recorded CW and CCW optical spectra of a  $10\ \mu\text{m}$  radius racetrack SRLs with an  $L_c$  of  $10\ \mu\text{m}$ .

## 5.8 Chapter summary

In this chapter, the design considerations of deeply etched semiconductor ring lasers and their building blocks were detailed. Based on BPM simulations and FP laser measurements, the waveguide width of  $2\text{-}3\ \mu\text{m}$  was found to be optimal for single mode operation. Non-radiative loss processes were reviewed and the effect of surface recombination on the device threshold current was investigated on different FP lasers with different waveguide widths. The contribution of the surface recombination losses was found to be negligible down to a waveguide width of  $2\text{-}2.5\ \mu\text{m}$ . If narrower waveguides are required, passivation of the dangling bonds is recommended. Then, bending losses of curved waveguides were simulated and measured, and it was found that a waveguide etch depth of  $3.26\ \mu\text{m}$  ( $1\ \mu\text{m}$  below the core) or deeper is an essential requirement to have minimal bending losses down to a radius of  $\sim 6\ \mu\text{m}$ . Furthermore, it was confirmed that a curved waveguide width of  $2\text{-}3\ \mu\text{m}$  is the optimum dimension for single transverse mode operation and for low bending losses.

Based on the simulated and experimental design data, SRLs with various dimen-

sions and evanescent point couplers were fabricated. These devices lased continuous wave at room temperature down to a radius  $8\ \mu\text{m}$ . The non-lasing operation below this radius was explained with increased bending losses as a result of the shallower etched point coupler regions. The increasing modal mismatch of these lag regions with reducing radius also clarified the reason for the disappearance of unidirectionality for devices with a radius smaller than  $20\ \mu\text{m}$ . Analysis of the resistive and thermal material properties also showed that the considerable dissipation of sub- $5\ \mu\text{m}$  radius devices causes early thermal roll-off and prevents SRL size reduction. Material and device design techniques used in VCSEL and high power laser research, such as reduction of the upper cladding thickness or the use of an n-type doped upper cladding with a buried tunnel junction [104], should allow a further miniaturisation of the rings.

The few microwatts output power level of the point coupler micro SRLs is inadequate for telecommunication applications, therefore as an alternative, racetrack shape SRLs with stronger output coupling were investigated. Different coupler design geometries were evaluated with a focus on short coupling length and low intra cavity back-reflections. Bi-level directional couplers were finally selected as the best candidates for high output power (4-10%), minimal intra cavity back-reflection and short length (10-20  $\mu\text{m}$ ). The intra cavity back-reflections and so the coupling between the counter-propagating modes was minimised by developing novel straight to curved transitions with continuously changing radius. These design efforts allowed the fabrication of compact racetrack shape SRL devices with output power levels in the milliwatt range. Moreover, thanks to the careful optimisation of the intra cavity reflections, robust unidirectional bistable operation was observed on all the fabricated SRLs with typical DER and SMSR values of 20 dB and 30 dB, respectively.

Finally, it has to be mentioned that other groups reported *cw*, room temperature lasing SDLs with a diameter of  $7.5\ \mu\text{m}$  on a III-V/SOI platform [105,22]. These reported devices also show robust unidirectional operation with excellent SMSR, but the DER is not reported. A great advantage of the III-V/SOI platform is that it can be incorporated into a CMOS fabrication flow. However, the small device size and the evanescent point coupling geometry only provides an output power of  $\sim 20\ \mu\text{W}$  (at the coupler). Such output power levels are sufficient for demonstrating optical functionalities but are inadequate for real telecom applications.

The low output power of these devices illustrates the fundamental problem of SRL size reduction very well: short cavity SRLs with a few microns radius require low mirror losses to allow low threshold lasing operation (or lasing at all). But this decreases the quantum efficiency considerably and hence the output power of the device. Therefore depending on the application the designer has to optimise both the threshold and the output power of the SRL by finding a good trade-off between the coupler strength and the device size.

# Chapter 6

## Dynamic device characterization

This chapter investigates the dynamical properties of SRLs. The response of directionally bistable SRL devices to ultra short external optical trigger pulses and telecommunication compatible signals is shown. The second part describes the monostable device behavior in the presence of a holding beam, which has the potential for creating all-optical logic using SRLs. Time domain measurements shown in this chapter were carried out by the IOLOS project partners at the University of Pavia.

### 6.1 SRL bistable characteristics – memory

The dynamical behavior of SRLs needs to be assessed in order to determine their response speed to external optical trigger signals. Figure 6.1 shows the setup that was used for the time domain characterisation of SRL devices. This general layout was used for the majority of the temporal measurements with slight modifications carried out if required. Input trigger signals were either the digitally modulated output of a MZ modulator or they were the few picoseconds long optical pulses from an optical parametric oscillator (OPO). The propagation delay of the evenly split input signal in the CW / EAST and CCW / WEST direction input fibers was balanced or unbalanced with a tunable delay line. Two circulators were used to separate the output signal from the same ports and the time traces were recorded with a 40 GHz bandwidth sampling oscilloscope. In case the input or output signal levels were too weak for triggering the switching or being detected by the oscilloscope,

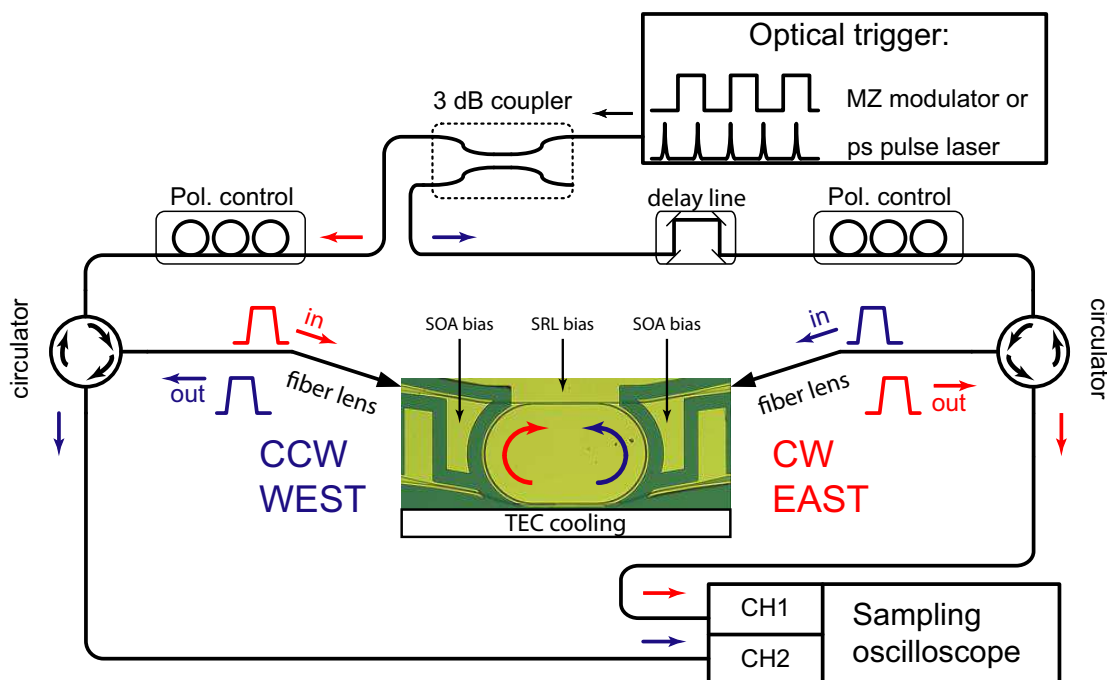


**Figure 6.1:** General layout of the experimental setup for measuring the dynamic properties of SRL.

erbium doped fiber amplifiers (EDFAs) were inserted into the signal propagation path.

The yield, robustness and performance of the shallow etched SRLs, which are reported in Section 4.5, proved to be excellent. Therefore, these fairly long ( $\sim 1.1\text{ mm} - 1.6\text{ mm}$ ) but highly reliable devices were selected to investigate the temporal response of SRLs to external optical trigger pulses. In order to avoid the overlap of the device response and the injected signal, a 5 ps optical pulse (1.2 nm FWHM bandwidth) was used to test the switching operation of the device. Figure 6.2(a) plots the experimental time traces of a 1.3 mm-long SRL (150  $\mu$  radius and 50% coupler device which was reported in Chapter 4.5) when two consecutive pulses are injected to the CW and CCW directions. Insertion losses of the fiber lenses and the losses of the non-pumped sections were partly compensated by injecting 30 mA into the output SOAs, and the bias current ( $I_{SRL}$ ) of the ring in this particular experiment was set to 130 mA ( $\sim 4 \times I_{th}$  – the P–I characteristic of the device is shown in Fig 4.13). The average in-fiber power of the injected

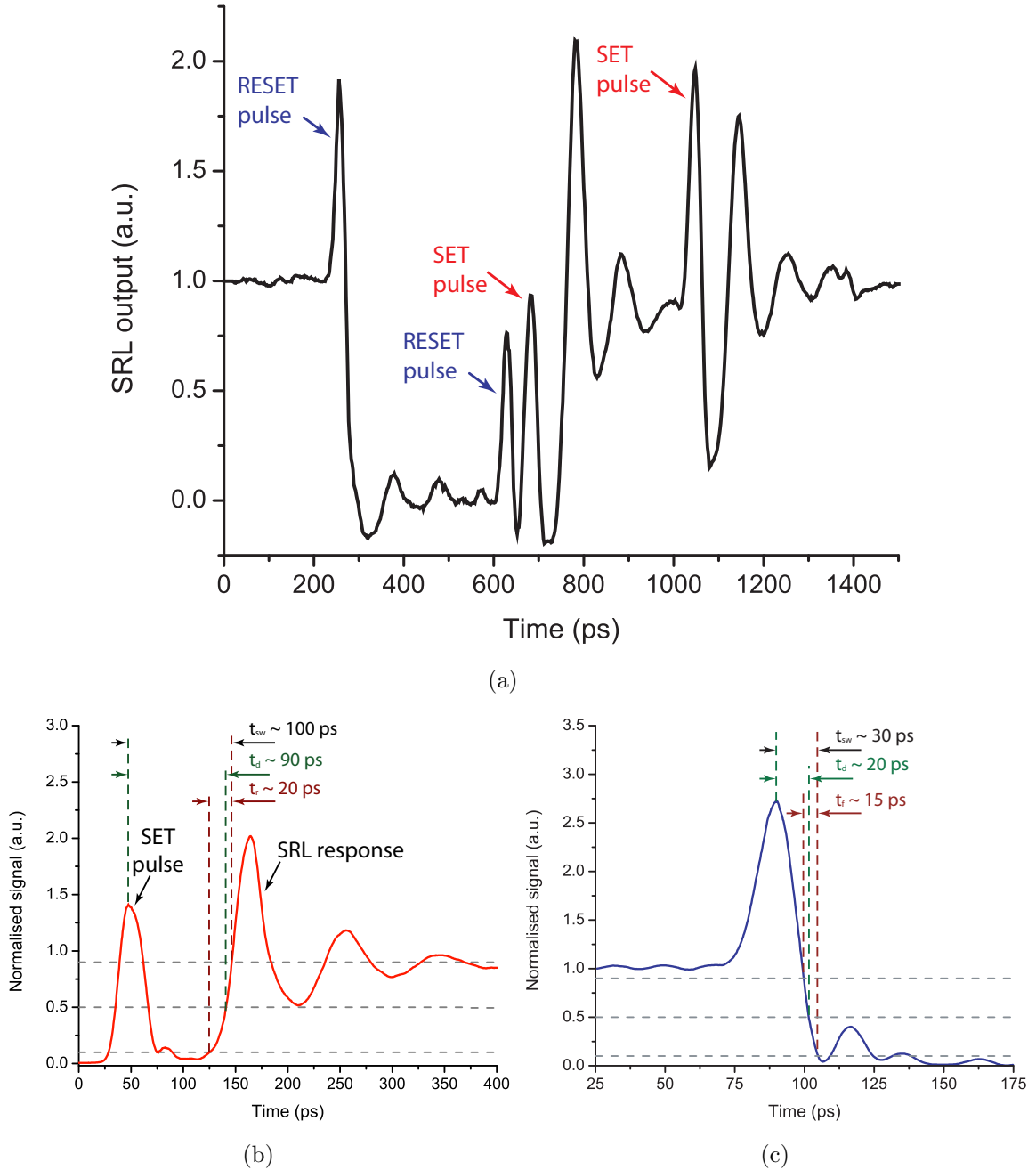


**Figure 6.2:** Experimental SRL time traces. (a) Device response to two subsequent set and reset pulses. (b) Typical switch on transition of a SRL. (c) Typical switch off transition of a SRL.

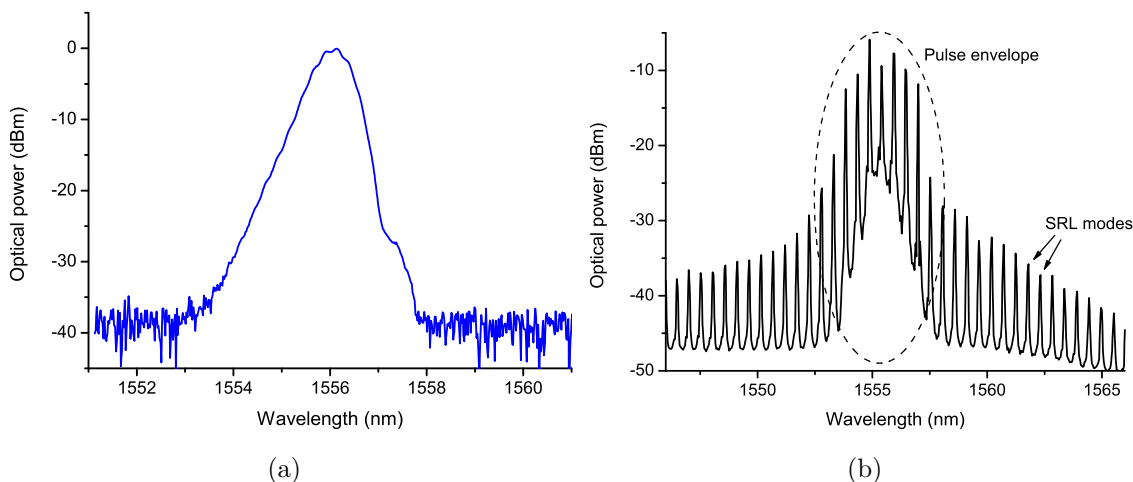


**Figure 6.3:** (a) Measured optical spectrum of the injected OPO pulses. (b) Measured optical spectrum of an SRL device under the injection of 5 ps pulses.

switching pulses was 20 mW and the peak wavelength of the pulses was aligned to 1556 nm, which is lasing peak of the SRL (see Figure 6.3(a)). A measured spectrum, which is the superimposition of the SRL output and the injected pulse, is shown in Figure 6.3(b).

In Figure 6.2(a) it can be seen that the trigger pulses, which are counter-propagating with respect to the actual lasing direction of the SRL, induce a direction reversal and those which are co-propagating do not trigger a direction change. If one considers the two lasing directions as logical states and the pulses injected into the CW and CCW access waveguides as logical inputs, then the above time trace demonstrates all the possible states and transitions of the truth table of a Set Reset flip-flop<sup>1</sup>. Careful observation of the time traces shows that the device has an unequal switch-on and switch-off time (see Fig. 6.2(b) and Fig. 6.2(c)). These figures clearly show that the rise and fall time ( $t_r$  and  $t_f$ ), which is the transition time required to change from 10% to 90% of the final value of the logic high level, is inadequate to define device switching speed. An additional time delay ( $t_d$ ) must be defined as the time required for the signal to reach the 50% value of the high level after the arrival of the pulse peak. These two characteristic times are sufficient to describe the response and total switching time ( $t_{sw}$ ) of a device. Fig. 6.2(b) and

<sup>1</sup>The input state SR=11 is not allowed.

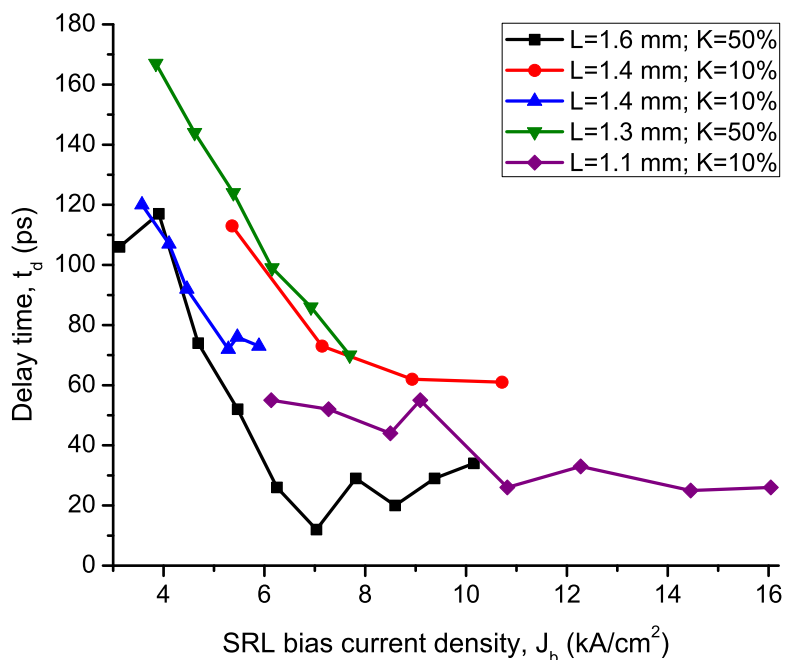


**Figure 6.4:** Measured switch-on time delay as a function of the SRL bias current in the case of different length and coupling strength devices.

in Fig. 6.2(c) also show that the rising edge of the device switching has an additional  $t_d$  of  $\sim 90$  ps, while the switch-off happens almost instantaneously in  $\sim 20$  ps. Rise and fall times are more symmetric, i.e.  $\sim 20$  ps and  $\sim 15$  ps, respectively. From these time traces it is ascertainable that the response speed of the device is strongly asymmetric and that it is limited by the switch-on delay.

The question one may ask now: is it possible to reduce the total switching time and to speed up the device operation by reducing the turn on delay? To answer this question the available temporal data of the shallow etched SRLs was analysed with the aim of determining how the device parameters, such as cavity length, coupling strength and bias current, influence the response time. Results indicate that the rise time, the fall time and the switching delay of a SRL are independent of the cavity length or the coupler strength. Preliminary switching tests carried out on  $250 \mu\text{m}$  long deep etched SRLs confirm this, since their fastest measured on and off  $t_{sw}$  of around 50 ps and 20 ps, respectively, are comparable to the best measured switching times of long cavity devices. On the other hand, it was found that the switch-on delay has a strong SRL bias current dependence. Figure 6.4

plots the recorded switch-on  $t_d$  values for different devices as a function of the SRL bias current density ( $J_b$ ). All the curves show a common trend: with increasing bias current, a decreasing trend of the on-delay is noticeable and after reaching a minimum value the delay does not decrease further with increasing current. It can be also seen that cavities of various sizes and couplers have a different  $t_d$  limit and slope as a function of the current, but based on the available data no evidence of  $t_d$  dependence on the design geometry could be found. A second observation made during the analysis of the time traces is that stronger pumping of the device also results in an increase of the frequency of the carrier relaxation related oscillation after a falling or a rising edge (Fig. 6.2 illustrates this phenomenon). It was also observed that the on-delay time becomes longer when higher energy pulses are used to switch the SRL. Furthermore, the minimum energy required to switch large SRLs was found to be  $\sim 200$  fJ, around the same order of magnitude as the energy stored in the cavity. This highlights a second advantage of device miniaturisation - apart from a smaller footprint - that micro size SRLs can be switched with a lower energy than large radius devices.

All of these results suggest that the delay before the rising edge is independent of the cavity size and that it is a type of large signal turn-on mechanism, which happens as a result of the pulse induced depletion of carriers below the threshold value, followed by resonant carrier relaxation. Such a laser turn-on delay phenomenon can be approximated by [72, 106]:

$$t_d \approx \tau_c \ln \frac{N_p - N_d}{N_p - N_{th}}, \quad (6.1)$$

where  $\tau_c$  is the carrier lifetime,  $N_d$  is the depleted carrier density as a result of the pulse,  $N_{th}$  is the carrier density of the active region at threshold, and  $N_p = \eta_i I_{SRL} / (qV)$  is the density of the externally injected carriers. The main assumptions of this relation are: a) the carrier density increases linearly with the current, and b) the carrier lifetime is constant. As a consequence of these assumptions, Eq. 6.1 produces accurate results only in the case of high carrier injection levels ( $N_p \gg N_d$ ). Moreover, Eq. 6.1 is an underestimation of the real value of  $t_d$  since the change of  $N$  as a function of the injected current is sublinear. Equation 6.1 was solved using the typical threshold values of large SRL devices and the measured  $\tau_c \simeq 0.27$  ns of the material from [54]. This calculated change of the turn-on delay as a function of  $I_{SRL}$  is plotted in Figure 6.5 for different rela-

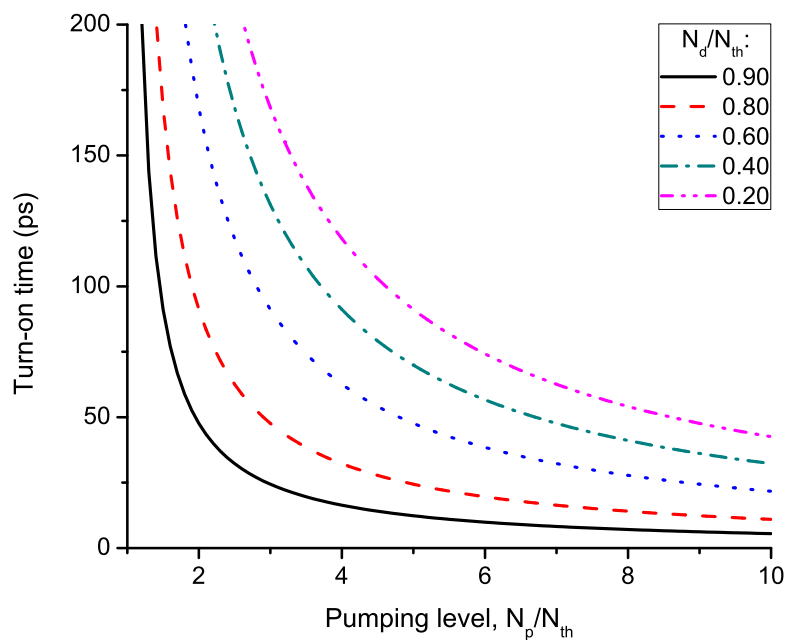


**Figure 6.5:** Calculated turn-on delay as a function of the external current injection with the relative carrier depletion as a parameter.

tive carrier depletion levels ( $N_d/N_{th}$ ). Despite the inaccuracy of the formula used, the approximation predicts a similar value range of  $t_d$  saturation levels as previously measured, and furthermore, the major trends of the plot agree well with the experimental observations:

- A deeper depletion of the carriers, i.e. a higher energy injected pulse, increases the delay time.
- A stronger carrier injection reduces the turn-on delay.
- The turn-on delay starts to saturate above a bias current of  $\sim 4-5 \times J_{th}$  (typical  $J_{th}$  values of the measured SRLs are 1.2-1.5 kA/cm<sup>2</sup>).

Based on the above findings, one can conclude that the major limitation of the SRL switching speed is the turn-on delay, which is a result of the pulse induced carrier depletion. The best measured total switch-on and switch-off times of large SRLs are  $\sim 60$  ps and  $\sim 30$  ps, respectively. These switching times make the SRL devices a suitable all-optical element for 10 Gbit/s optical networks. Higher bi-

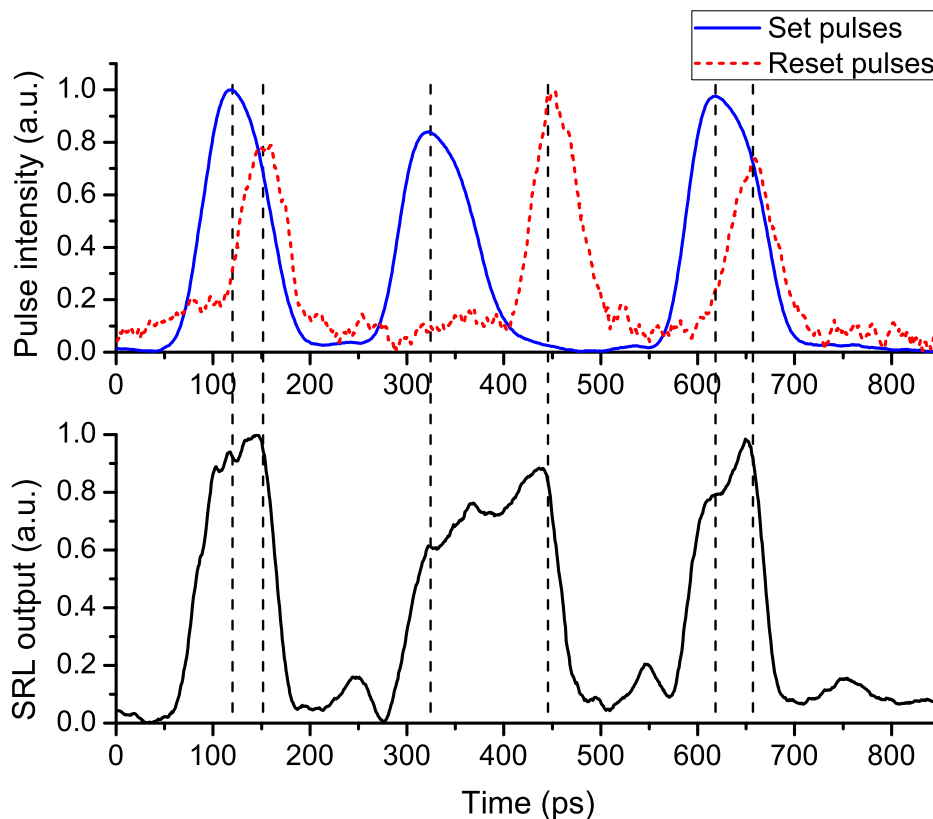


**Figure 6.6:** Time trace of the response of a SRL device to 50 ps switching pulses.

trate operations require the development of semiconductor structures with faster recombination times, such as p-type doped [107] or ion-implanted QWs [108].

Results shown so far characterised the switching response of large SRLs for very short optical pulses. In these experiments, the  $\sim 1.2$  nm bandwidth injected pulse excited multiple longitudinal modes of the cavity which may cause multi-mode laser dynamics and may alter device transients; therefore, it is important to confirm the operation speed of the device with longer, telecom compatible signals. Figure 6.6 shows a time trace, in which the SRL device was switched with 50 ps pulses (0.16 nm FWHM bandwidth) which have a bit period of 100 ps. It can be seen that in the case of such long switching pulses, the co-propagating set signal overlaps with the rising edge of the SRL and creates an asymmetric mark to space ratio, which potentially causes a narrow horizontal opening of the eye diagram. The masking effect of the switching signal can be eliminated from the time trace either

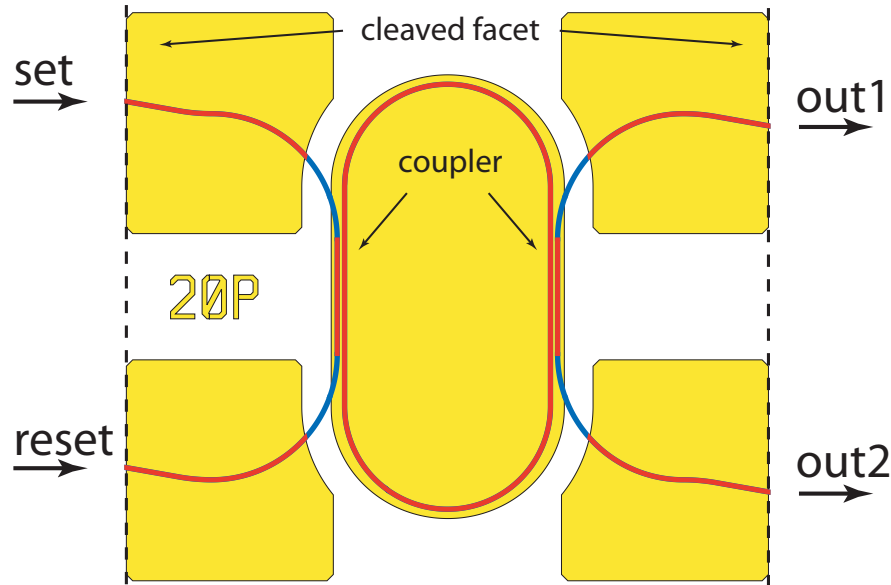


**Figure 6.7:** Alternative SRL design for eliminating asymmetric mark to space ratios, caused by the switching pulses.

by accessing all four output waveguides or with alternative design geometries, as illustrated in Figure 6.7. In this arrangement the CW and CCW access waveguides curve back to the same side hence the pulses injected from left and right side fiber lenses do not appear in the output time traces as they are separated by the ring. The coupled pulse will be visible though.

## 6.2 SRL monostable characteristics – logic gates

In the previous section it was shown that the lasing direction of a semiconductor ring lasers can be switched with external short pulses. The same functionality can be achieved by locking the SRL to a continuous wave external optical injection into the main lasing mode [109, 52]. As explained in Chapter 1.1, when two counter-directional *cw* beams are injected into the main lasing mode of an SRL, its directional bistability is not affected and the selected lasing direction of the device depends on the relative power of the two beams [110]: When a higher power ( $P_{high}$ ) beam is injected in the CW direction and a lower power beam ( $P_{low}$ ) is injected in the CCW direction the SRL prefers to lase co-directional with  $P_{high}$ . By turn-

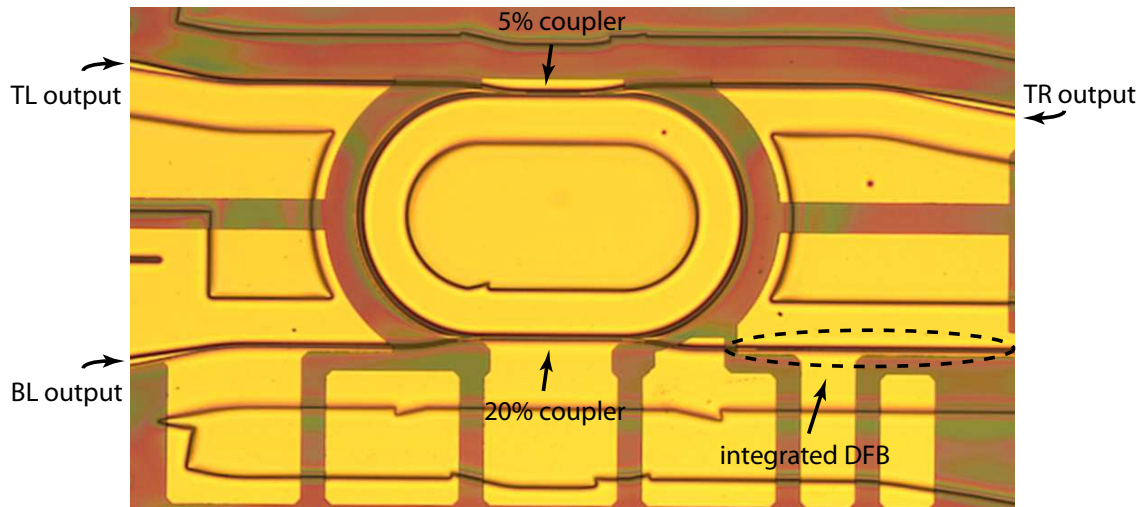


**Figure 6.8:** Optical micrograph of a fabricated SRL with integrated DFB laser.

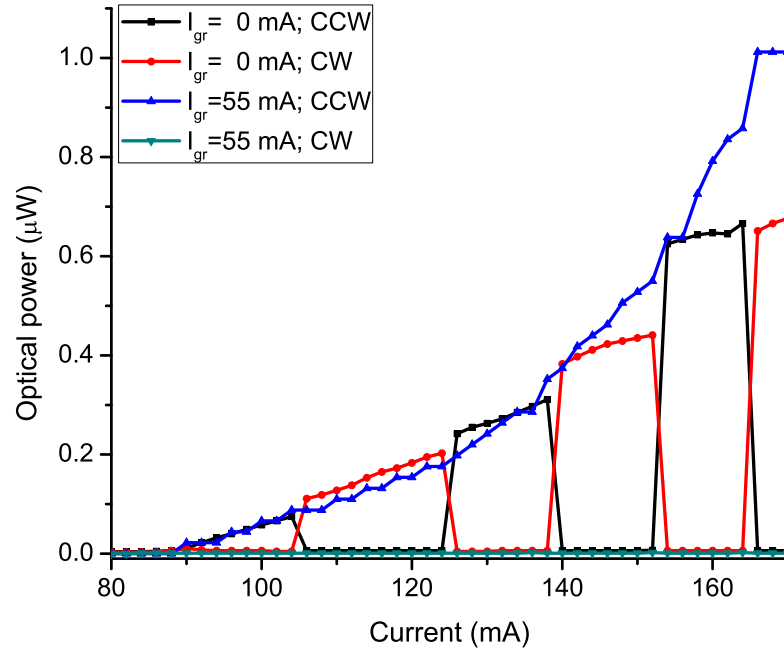
ing off the  $P_{high}$  beam a directional reversal is triggered and now the SRL lases co-directional with  $P_{low}$ . No directional change can be observed in case the  $P_{low}$  beam is turned off and  $P_{high}$  stays on. If one considers the  $P_{low}$  injection as a holding beam (HB) and the  $P_{high}$  injection as a trigger signal then this configuration realises a monostable device. Such a monostable can be used to realise all optical functionalities, such as logic gates (NOT, NAND, XOR etc.) [111, 112], signal regeneration (reamplification (1R), reshaping (2R), retiming (3R)) [113] and label swapping [114]. Unfortunately, earlier experiments showed that injection locking the SRL slows down the device operation considerably (compared to the bistable configuration), as the maximum achievable operation speed drops to around 0.6-0.7 Gbit/s.

Similarly to what has been proposed for SOAs, the photon energy of the HB must be higher than the gain peak of the material in order to improve switching speed [115, 116]. In order to test this idea, SRL devices with an integrated DFB holding beam source in one of the output arms were designed and fabricated. Two micrometer wide, rectangular shape lateral sidewall gratings were used as the integrated Bragg reflectors of the DFB lasers with a 500 nm recess on each side and with a duty cycle of 50%. On the top of the grating a 500 nm contact window was defined for current injection. Figure 6.8 shows an optical micrograph of a completed device. The weak output couplers of the SRLs (top: 5% and bottom: 20%) ensure

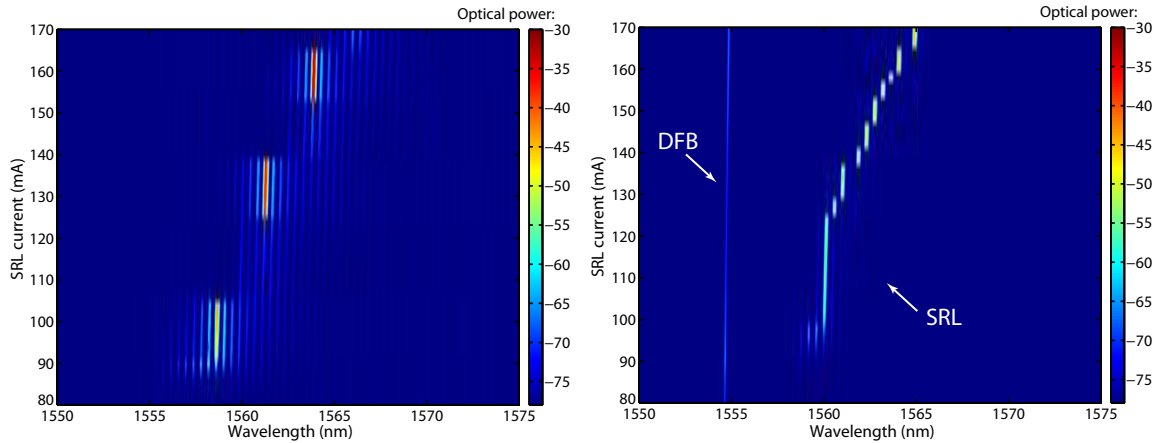
a device lasing wavelength above 1555-1560 nm, while the lasing wavelength of the integrated DFB sources is designed to be at 1500 nm and 1550 nm. Threshold currents of around 30 mA and 85 mA were measured for the integrated DFBs and for the SRLs, respectively.

The effect of the integrated holding beam on the device directionality was tested by recording the P–I characteristics of the SRL (integrated with the 1550 nm lasing wavelength DFB) for DFB bias current ( $I_{DFB}$ ) values ranging from 0 mA to 90 mA (5 mA steps). Lensed fibers were used to collect the output light corresponding to the two directions of the SRL at the TR and TL outputs (see Fig. 6.8). Below a DFB current of 40 mA (weak injection) usual unidirectional bistable SRL operation was observed. As an example, the  $I_{DFB}=0$  mA P–I curve of the SRL is plotted in Figure 6.9(a) showing the usual directional reversals for increasing  $I_{DFB}$ . The corresponding spectral map of the CCW direction is plotted in Figure 6.9(b). Between  $I_{DFB}$  of 40 mA to 55 mA, a transition from unidirectional bistability to monostability could be observed with less reversals observable on the P–I plot and a more dominant lasing in the CCW direction. For DFB currents of 55 mA and above, the bistable region vanished and the device became completely unidirectional, as illustrated in Figure 6.9(a). The corresponding spectral map for  $I_{DFB}=55$  mA is plotted in Figure 6.9(c), with the lasing peak of the DFB visible on the left side of the SRL longitudinal modes. The measured peak wavelength of the DFB laser is a few nm higher than designed, which is a result of the underestimation of the effective modal index of the waveguide grating. If the detuning between the HB and the SRL gain peak is too small, four-wave mixing (FWM) between the two beams may appear in the ring cavity when the wavelength of one of the longitudinal side modes of the SRL overlaps with the lasing wavelength of the DFB [117, 52]. For currents above  $I_{DFB}=65$  mA FWM effects similar to what previously reported [117] could be observed on the measured optical spectral maps. Similar threshold and directional holding was observed for the 1500 nm wavelength DFB integrated SRL devices but the FWM phenomenon was not observed since the wavelength of the holding beam is blue-shifted  $\sim 60$  nm with respect to the lasing longitudinal modes of the SRL. These results indicate clearly that an external beam that does not injection lock the SRL can hold the lasing direction of the device and may allow fast monostable operation.

The monostable behaviour and the switching speed of the integrated device



(a)



(b)

(c)

**Figure 6.9:** Measured output characteristics of the integrated DFB SRL device. (a) Recorded P–I characteristics for  $I_{DFB}$  values of 0 mA and 55 mA. (b) Measured spectral map of the CCW direction for  $I_{DFB}=0$  mA. (c) Measured spectral map of the CCW direction for  $I_{DFB}=55$  mA. The bars on the right side link the optical power in dBm to the colours.

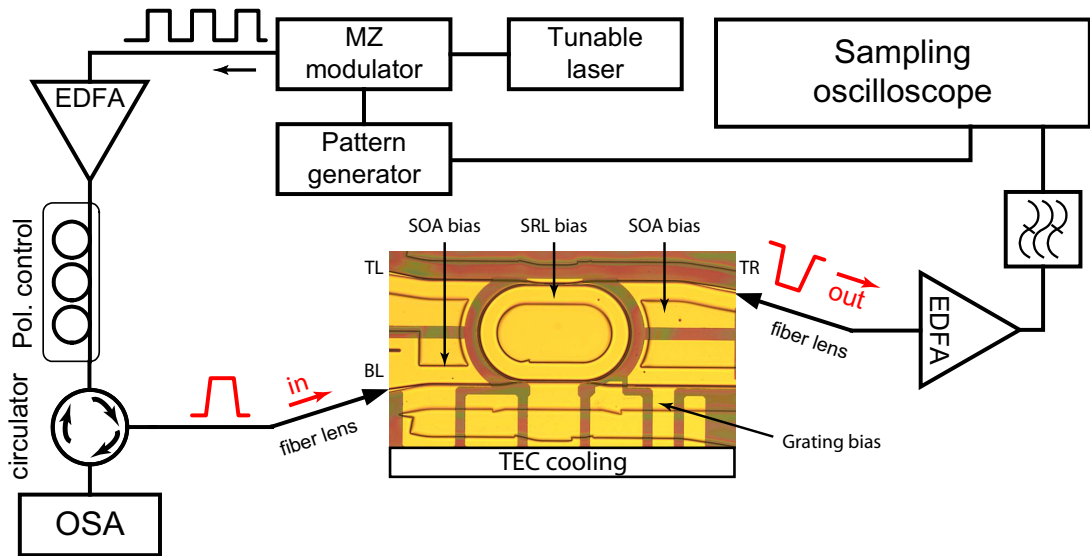


**Figure 6.10:** Experimental setup for the temporal characterization of the monostable SRLs and for the demonstration of an all-optical NOT gate.

has to be investigated to determine the potential of such an integrated SRL for all-optical logic applications. First, the capability of the device for monostable operation was confirmed. In these experiments, the 1500 nm DFB integrated SRL was used in order to avoid FWM effects. The SRL and the DFB were biased at 180 mA and 50 mA, respectively and the light of the tunable laser, the wavelength of which was matched to the main lasing mode of the SRL, was injected in the BL port. When the tunable laser was turned off, the SRL was lasing co-directionally with the holding beam (CW in Fig. 6.10). However, when the tunable laser was turned on with a power exceeding -6 dBm (in fiber), the SRL switched direction to the CCW direction. After the tunable laser was switched off the lasing direction of the SRL restored back to the CW direction. These observations demonstrate the ability of the integrated device to be employed as a monostable element.

The characterisation of the switching speed of the integrated SRL was carried out in the measurement alignment shown in Figure 6.10. The modulated signal was injected into the CCW lasing direction via the BL port and the signal of the complementary SRL direction was collected from the TR port. It was found that the rise and fall time of the SRL response decreases as the  $P_{high}$  of the injected modulated signal increases, therefore the maximum possible  $P_{high}$  of 10 dBm (in fiber) was

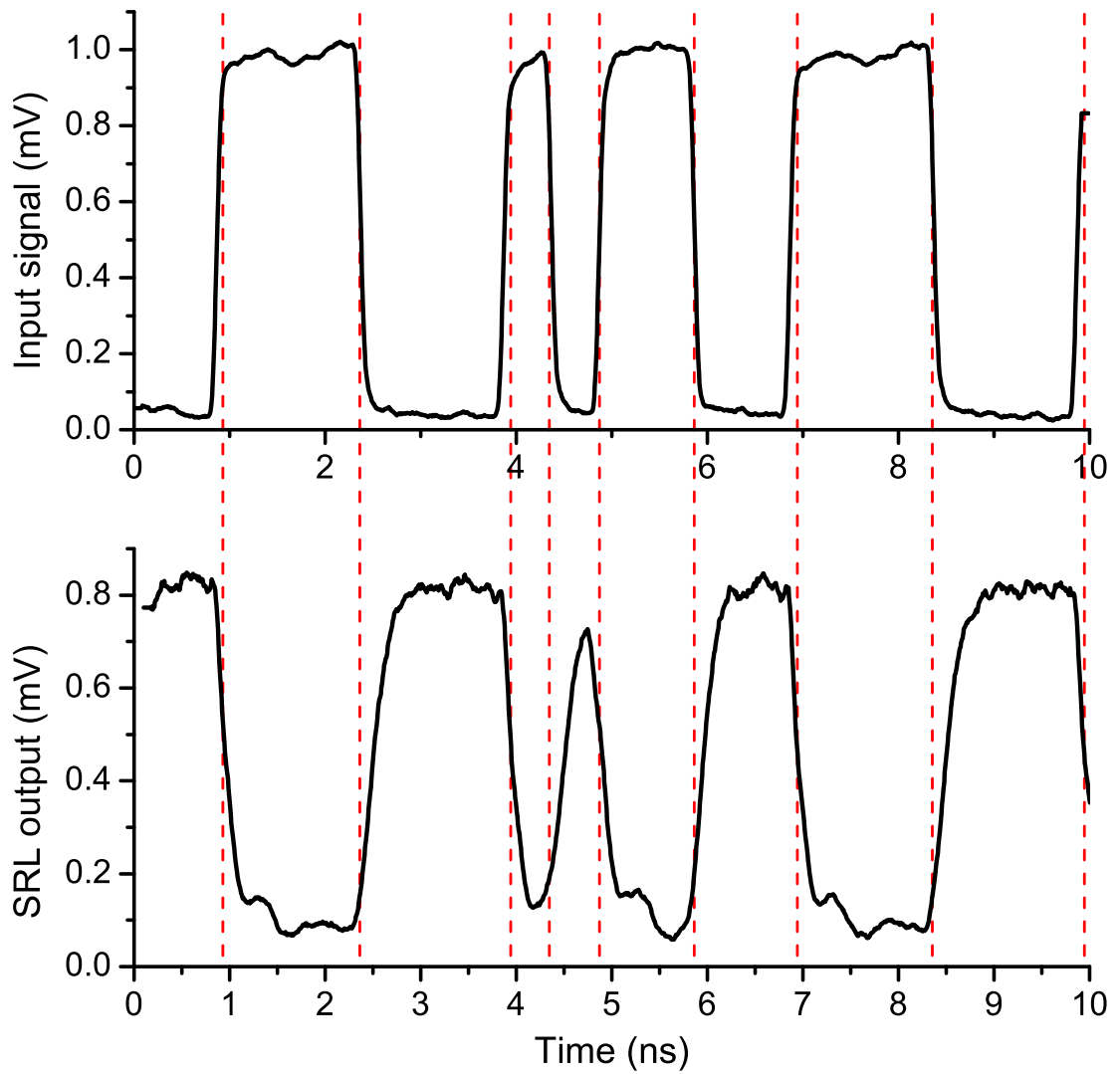


**Figure 6.11:** Measured time traces of the injected 2 Gbit/s 101100111000 bit sequence (top) and the SRL response (bottom).

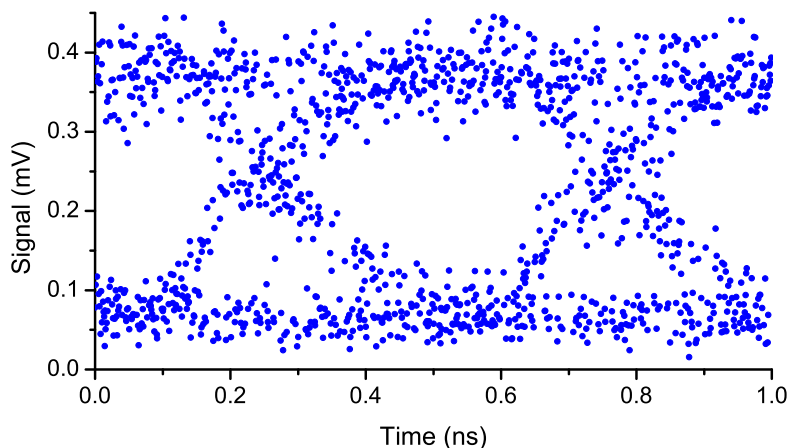


**Figure 6.12:** Measured  $2^7-1$  PRBS eye diagram of the integrated NOT gate for a data rate of 2 Gbit/s.

used. Measurements show reliable SRL switching up to 2-2.5 Gbit/s data rates. Figure 6.11 plots an example of a 2 Gbit/s input bit sequence of 101100111000 (top) and the recorded SRL response (bottom). For the same data rate the eye diagram of a  $2^7-1$  pseudo random bit sequence (PRBS) is plotted in Figure 6.12.

In such a configuration the device acts as an all-optical NOT gate. A slight change in the device geometry with the addition of integrated elements allows the realization of further functions such as the NOR gate (see Chapter 1.1). Inspection of the rising and falling edges show clearly that the limiting factor of this holding beam technique is the slow response time of the SRL. The reason for the slower operation of the holding beam configurations compared to the injection free flip-flop configuration is not clear at this time. Further investigations are required to reveal the physical background effects of the holding beam.

### 6.3 Chapter summary

This chapter presented some experiments on the dynamical behavior of SRL devices when used as FFs or logic gates. Large (1.1 mm - 1.6 mm long) rings were used to characterise the temporal response of SRLs to external optical trigger pulses. All-optical, 10 Gbit/s Set Reset flip-flop operation was demonstrated using 5 ps (1.2 nm FWHM) optical pulses. The best measured switch-on times ( $\sim 60$  ps) were found to be longer than the switch-off times ( $\sim 30$  ps), because of the longer turn-on delay

after the arrival of the triggering pulse. The analysis of the recorded time traces of several different SRL geometries indicates that the coupler strength or the cavity size do not influence the switching speed of the device. This latter observation is supported by the findings of [22], where a  $t_{sw}$  of  $\sim 60$  ps was reported for a  $7.5 \mu\text{m}$  diameter SDLs, and by the measurements on micro size SRLs, where a  $t_{sw}$  of  $\sim 50$ - $60$  ps was measured for a  $30 \mu\text{m}$  radius ( $250 \mu\text{m}$  long) SRL.

A second outcome was that the on-delay time reduces considerably with increasing injected carrier density. The observed dependence of the on-delay time on the injected pulse energy and bias current was found to be the result of the carrier depletion by the triggering pulse that is followed by a resonant carrier relaxation. A simple formula was used to approximate the turn-on  $t_d$  as a function of the injected carrier density, in good agreement with the experimental data. The compatibility of SRLs to telecommunication networks was then demonstrated by switching the device with 50 ps pulses which had a bit period of 100 ps.

In the second part of the chapter, the monostable characteristics of SRLs were discussed. A major drawback is that monostable operation in an SRL requires external injection locking that considerably slows down the device to 0.6-0.7 Gbit/s. An alternative holding beam scheme with an injected wavelength shorter than the main SRL longitudinal lasing mode was proposed to reduce the SRL switching time. 1500 nm and 1550 nm lasing wavelength DFB lasers were integrated on the output waveguide of the SRL to confirm this idea. The recorded P-I curves of the fabricated devices demonstrated directional holding of the SRL for DFB currents above 50-55 mA. The switching speed of the new holding beam geometry was characterised in a NOT gate configuration, which showed reliable SRL switching operation up to 2 Gbit/s data rates. These temporal measurements demonstrate the capability of SRL monostables to be used as all-optical logic gates, although the measured switching speed is still slower than a free running SRL bistable. In order to clarify the reason for the slowing of switching operation, further experiments are required to understand the underlying physical effects.

# Chapter 7

## Conclusions and future work

### 7.1 Conclusions

This thesis dealt with the design, fabrication and characterisation of semiconductor ring lasers (SRLs) that show unidirectional bistable behaviour and are intended for employment in all-optical signal processing. The first objective of the work was to develop a reliable and high-yield SRL design and technological platform for producing devices with robust and repeatable unidirectional bistable operation that can be used for the systematic investigation of SRL temporal dynamics. The second goal was the establishment of the necessary fabrication and design know-how to allow for the down-scaling of the SRL footprint.

One of the most significant technological developments carried out during this work was the optimisation of proximity error correction for e-beam lithography. Since its development, this code has been used by the users of the James Watt Nanofabrication Centre who fabricate InP based opto-electronic devices to correct the clear-out doses of different patterns automatically during the fracturing stage. This improved code also allowed for the development of a single-step etch mask patterning technique using HSQ resist that is capable of producing 100 nm wide gaps between two waveguides with an imaging aspect ratio of 10 and a sidewall roughness of a few nanometers.

The technologically mature, weakly guided shallow etched waveguide geometry proved ideal for the fabrication of large radius SRLs with extremely high yield and repeatability. A  $\text{CH}_4/\text{H}_2/\text{O}_2$  RIE process was optimised for the HSQ hard masks

to fabricate the waveguides. The high selectivity of this chemistry between the InP cladding and the core layers allowed the control of the etching to a depth of  $1.92\ \mu\text{m}$  with a precision of  $\pm 10\ \text{nm}$ . For this depth, the bending losses of the waveguide were found to be minimal down to a radius of  $150\ \mu\text{m}$ . This size limit was pushed down further to  $100\ \mu\text{m}$  with a 35 minutes long over-etch but proved to be impractical as the series resistance of the upper cladding increased considerably due to the acceptor passivating effect of the  $\text{H}_2$ . A second benefit of using a highly selective etch chemistry is that the etch depth in the sub-micron gaps of a directional coupler could be controlled within a few nanometers precision, as a result of which, fabricated couplers have only an average 3% deviation from the designed values. Thanks to the robust etch process and the careful waveguide and coupler design, 98% of the fabricated shallow etched SRLs exhibited continuous wave, room temperature lasing with a current threshold dispersion of 2-3 mA only. The reliability and long lifetime of these devices is confirmed by the fact that SRLs fabricated 3 years ago in the first batch still lase without any signs of performance degradation. Robust unidirectional operation from near current threshold up to  $5-6 \times I_{th}$  with a SMSR and DER of 30-35 dB was achieved on the majority of the SRLs by reducing the reflections of the cleaved output mirrors to  $\sim 10^{-3}$  through the use of  $10^\circ$  tilted and  $12\ \mu\text{m}$  tapered output waveguides. The excellent reliability and robust unidirectional operation of the fabricated shallow etched devices triggered a very extensive research on SRL-based all-optical switching that resulted in over 30 peer reviewed publications and several invited talks. Moreover, the solid design know-how and the robustness of the fabrication technology opened up new prospects for monolithic integration, such as the demonstration of a SRL monostable with an integrated DFB laser holding beam (further integrated geometries be detailed in the next section).

The size reduction of SRL and SDL devices requires the development of deeply etched waveguide geometries to increase the horizontal optical confinement and therefore minimise the bending losses on tight waveguide bends. Simulations and measurements of the propagation losses and bending losses of the Al-quaternary material used in this work indicate that 2-3  $\mu\text{m}$  wide and 3.26  $\mu\text{m}$  deep waveguides (etched 1  $\mu\text{m}$  below the core) suffer from minimal curvature losses down to a radius of 6  $\mu\text{m}$ , and that 4.5  $\mu\text{m}$  deep waveguides suffer from negligible bending losses down to a radius of 3-4  $\mu\text{m}$ . Three ICP RIE chemistries were developed and evaluated

to meet such etch depth requirements with a  $\sim 600$  nm thick HSQ mask. Smooth sidewalls were achieved with the  $\text{CH}_4/\text{H}_2/\text{Cl}_2$  chemistry but the strong mask edge erosion limited the maximum etching depth to  $2.7\text{-}2.8\ \mu\text{m}$ . A second developed chemistry based on  $\text{Cl}_2/\text{Ar}/\text{N}_2$  provided a waveguide etching as deep as  $3.5\ \mu\text{m}$  and produced sidewalls with excellent verticality but considerable roughness. The sidewall smoothness of this process was significantly improved by replacing the  $\text{N}_2$  inhibitor of the chemistry with  $\text{BCl}_3$ , which also had the additional advantage of reducing the hard mask sputtering rate and thus allowed the fabrication of  $4\text{-}5\ \mu\text{m}$  deep waveguides comfortably. A performance analysis of the FP lasers that were fabricated using the two  $\text{Cl}_2/\text{Ar}$  based recipes highlighted that, down to a waveguide width of  $2\text{-}2.5\ \mu\text{m}$ , non-radiative surface recombination causes only a minor degradation of the laser threshold. Further, using experimentally determined material parameters, it was calculated that the radius of a SRL can be reduced down to  $3\text{-}4\ \mu\text{m}$  without considerably increasing the threshold current density. Based on these findings, micro-SRLs with waveguide widths of  $2\text{-}3\ \mu\text{m}$  and etch depths of  $3.26\text{-}4.5\ \mu\text{m}$  were fabricated and assessed. These devices lased *cw*, room temperature down to a radius of  $8\ \mu\text{m}$ . Below this radius the excess bending losses of the shallower etched coupler regions prevented any lasing action. The strong modal mismatch of these RIE-lag regions also explains the observed disappearance of unidirectionality for devices with a radius smaller than  $20\ \mu\text{m}$ . It was found that the high resistance of sub- $5\ \mu\text{m}$  radius devices poses a second limit for footprint reduction, since strong Joule-heating considerably degrades the lasing performance.

The very low output power level (few microwatts) of micro-SRLs with point couplers is inadequate for telecommunication applications; therefore, in order to improve the output power, the design of a racetrack-shape cavity geometry with strong output coupling was investigated. Bi-level directional couplers were selected as the best candidates for high output power ( $\kappa \simeq 4\text{-}10\%$ ), short length ( $10\text{-}20\ \mu\text{m}$ ) and minimal intra cavity back-reflection. In order to preserve robust unidirectional operation of the SRLs the intra cavity back-reflections (i.e. the coupling between the counter-propagating modes) were minimised by developing novel straight to curved transitions with gradually changing radius. These design efforts allowed the fabrication of small footprint ( $\sim 250\text{-}300\ \mu\text{m}^2$ ) and *cw* lasing SRL devices with output power levels in the milliwatt range. Thanks to the careful optimisation of the intra cavity reflections, robust unidirectional bistable operation was observed on

all of the fabricated SRLs with typical DER and SMSR values of 20 dB and 30 dB, respectively. Furthermore, the comparison of DER and SMSR values of various racetrack SRLs with various degrees of sidewall roughness indicates that smooth sidewalls are crucial for robust unidirectional operation.

Reliable, Set-Reset flip-flop operation with switch-on and switch-off times as fast as  $\sim 60$  ps and  $\sim 30$  ps, respectively was demonstrated by injecting 5 ps and 50 ps optical pulses into large size ( $\sim 1.1$ -1.6 mm) SRLs. Rise and fall times were measured to be symmetric, around 1-2 times the cavity round trip time, while the longer turn-on delay of the laser after the arrival of the triggering pulse was identified as the source of the on-off time asymmetry. Delay time measurements and calculations are in a good agreement and show a strong dependence of the turn-on delay on the SRL bias current and on the energy of the injected pulse, which suggests that the on-delay is the result of the carrier depletion induced by the triggering pulse. Based on these measurements, it can be concluded that the carrier lifetime is the main limiting factor of the SRL switching time. It has to be noted that these results contradict the prediction that the SRL switching time is only proportional to the build up time of the lasing field (i.e. it is proportional to the cavity length). In fact, the experiments completed so far indicate that switching only occur in the presence of strong triggering pulses that perturb the carrier population of the laser. Further measurements are currently being performed on micro-SRLs to confirm this conclusion. Finally, a monostable device consisting of a SRL and an integrated DFB laser was presented, which shows potential as a building block for all-optical logic gates. This holding beam geometry exhibited reliable switching operation up to 2 Gbit/s data rates in a NOT gate configuration.

## 7.2 Future Work

The achievements of this work established a solid technological platform for the fabrication of robust shallow and deep etched SRLs. Although both fabrication and device design are well established, there are few more technological developments that would further improve the device performance and robustness:

- Improvement of the sidewall verticality of the  $\text{Cl}_2/\text{Ar}/\text{BCl}_3$  chemistry for the fabrication of sub-micron optical gratings and mirrors with an extremely

smooth surface.

- Implementation of a non-radiative sidewall recombination passivation process for higher efficiency of lasers with deeply etched waveguide geometries.
- Redesign of the material epitaxy for better control of the etching depth through the introduction of a dry etch stop layer above the core of the material.
- Reduction of the carrier lifetime via ion implantation or doping for improving the SRL switching speed.

Apart from the technological developments, several device measurements are also required to improve the understanding on the SRL performance:

- Lifetime assessment of deeply etched lasers. In particular, it would be important to assess the influence of the Al-quaternary core on the lifetime of the devices. Should the presence of aluminium be detrimental on the lifetime, alternative P-quaternary gain media should be considered.
- Characterisation of the switching speed of micro-SRL. These measurements are currently being performed by our colleagues at the University of Pavia and will provide a clear understanding on the dependance of the switching speed on the cavity size.
- Further experiments on the optimum wavelength and energy of the HB are required to improve the operation of the monostable configuration.
- Investigation on the multi wavelength stability in SRLs. In fact, it was predicted that this form of multi-stability occurs with much weaker triggering pulses and should, therefore provide a faster switching.

The high yield of the devices and the design know-how allow future research to focus more on system design and complex integration rather than on the development of new processes and device optimisation. This technology was already used to fabricate novel integrated devices that require a more detailed investigation:

- Wavelength tunable coupled double SRLs; see Figure 7.1.

- Four coupled rings that might find applications in chaos generation and in complex optical networks; see Figure 7.2.
- Odd number of coupled rings to form an SRL ring-oscillator; see Figure 7.2.
- SRL mode-locked devices; see Figure 7.2.

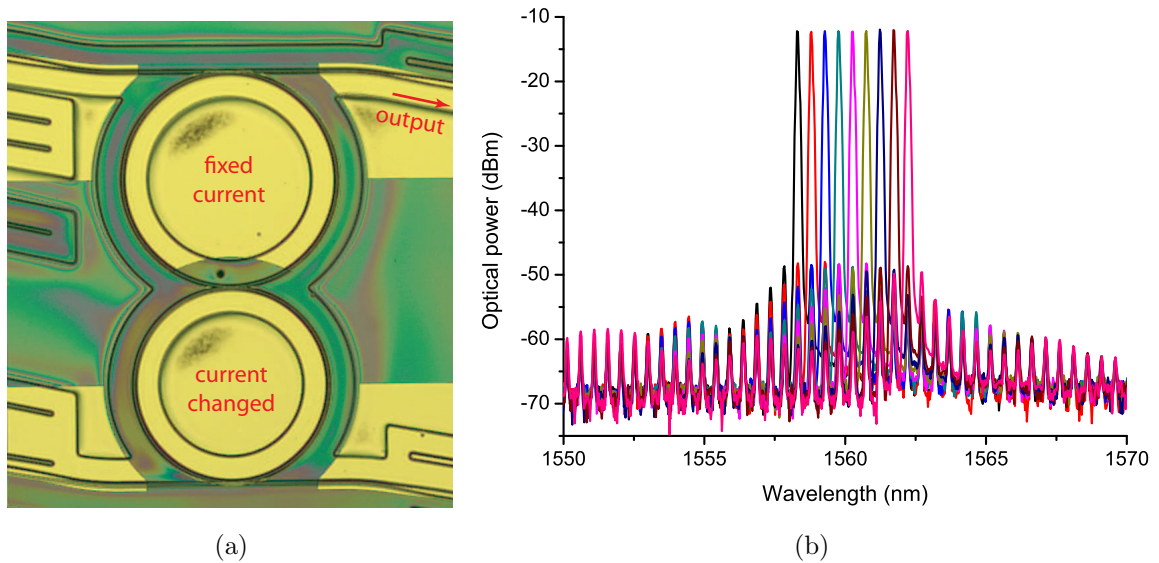


**Figure 7.1:** Wavelength tunable coupled double SRL. (a) Optical micrograph of the device. (b) Example tuning characteristics.

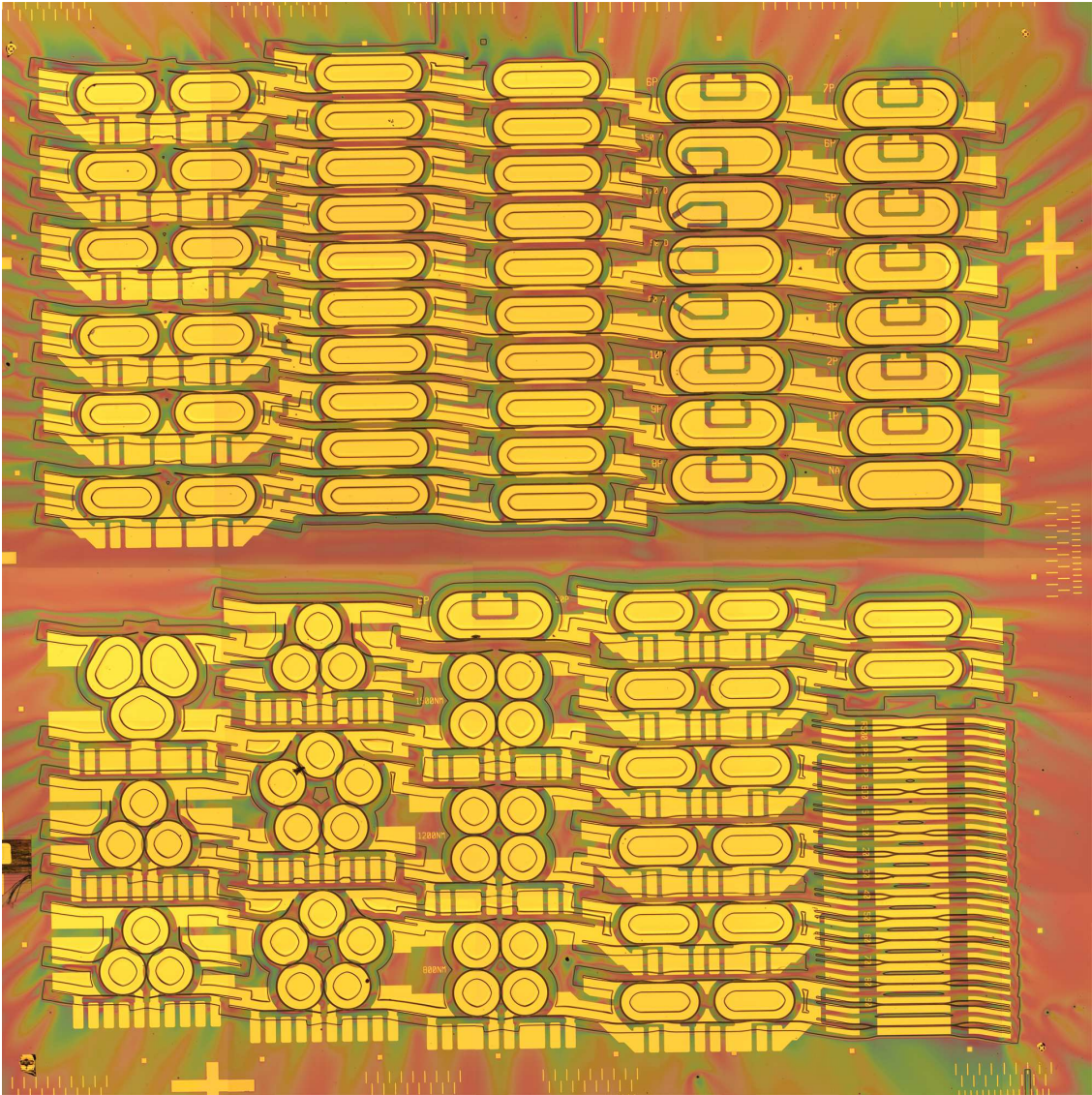


**Figure 7.2:** Optical micrograph of the chip GAM0170 after the p-type metallization lift-off step.

# Bibliography

- [1] S. Nicholes, M. Masanovic, B. Jevremovic, E. Lively, L. Coldren, and D. Blumenthal, “An  $8 \times 8$  InP Monolithic Tunable Optical Router (MOTOR) Packet Forwarding Chip,” *Journal of Lightwave Technology* **28**, pp. 641 – 650, feb 2010.
- [2] R. Nagarajan, M. Kato, J. Pleumeekers, P. Evans, S. Corzine, S. Hurtt, A. Dentai, S. Murthy, M. Missey, R. Muthiah, R. Salvatore, C. Joyner, R. Schneider, M. Ziari, F. Kish, and D. Welch, “InP photonic integrated circuits,” *IEEE Journal on Sel. Top. in Quantum Electronics* **16**(5), pp. 1113 –1125, 2010.
- [3] K. Stubkjaer, “Semiconductor optical amplifier-based all-optical gates for high-speed optical processing,” *Selected Topics in Quantum Electronics, IEEE Journal of* **6**, pp. 1428 –1435, nov/dec 2000.
- [4] Y. Liu, E. Tangdionga, Z. Li, S. Zhang, H. de Waardt, G. Khoe, and H. Dorren, “Error-free all-optical wavelength conversion at 160 gb/s using a semiconductor optical amplifier and an optical bandpass filter,” *Journal of Lightwave Technology* **24**, pp. 230 – 236, jan. 2006.
- [5] H.-Y. Yu, D. Mahgerefteh, P. Cho, and J. Goldhar, “Optimization of the frequency response of a semiconductor optical amplifier wavelength converter using a fiber bragg grating,” *Journal of Lightwave Technology* **17**, pp. 308 – 315, feb 1999.
- [6] E. Tangdionga, Y. Liu, H. de Waardt, G. D. Khoe, A. M. J. Koonen, H. J. S. Dorren, X. Shu, and I. Bennion, “All-optical demultiplexing of 640 to 40

- gbits/s using filtered chirp of a semiconductor optical amplifier,” *Optics Letters* **32**(7), pp. 835–837, 2007.
- [7] H. Mulvad, E. Tangdionga, H. de Waardt, and H. Dorren, “40 ghz clock recovery from 640 gbit/s otdm signal using soa-based phase comparator,” *Electron. Lett.* **44**, pp. 146–147, january 2008.
- [8] Y. Liu, E. Tangdionga, Z. Li, H. de Waardt, A. Koonen, G. Khoe, X. Shu, I. Bennion, and H. Dorren, “Error-free 320-gb/s all-optical wavelength conversion using a single semiconductor optical amplifier,” *Journal of Lightwave Technology* **25**, pp. 103–108, jan. 2007.
- [9] H. Sun, Q. Wang, H. Dong, Z. Chen, N. Dutta, J. Jaques, and A. Piccirilli, “All-optical logic xor gate at 80 gb/s using soa-mzi-di,” *Quantum Electronics, IEEE Journal of* **42**, pp. 747–751, aug. 2006.
- [10] A. Malacarne, J. Wang, Y. Zhang, A. Barman, G. Berrettini, L. Poti, and A. Bogoni, “20 ps transition time all-optical soa-based flip-flop used for photonic 10 gb/s switching operation without any bit loss,” *Selected Topics in Quantum Electronics, IEEE Journal of* **14**, pp. 808–815, may-june 2008.
- [11] M. T. Hill, H. J. S. Dorren, X. J. M. Leijtens, J. H. den Besten, T. de Vries, J. H. C. van Zantvoort, E. Smalbrugge, Y. S. Oei, J. J. M. Binsma, G. D. Khoe, and M. K. Smit, “Coupled mach-zehnder interferometer memory element,” *Opt. Lett.* **30**(13), pp. 1710–1712, 2005.
- [12] P.-L. Li, D.-X. Huang, and X.-L. Zhang, “Soa-based ultrafast multifunctional all-optical logic gates with polsk modulated signals,” *Quantum Electronics, IEEE Journal of* **45**, pp. 1542–1550, dec. 2009.
- [13] H. Kawaguchi, “Bistable laser diodes and their applications: state of the art,” *Selected Topics in Quantum Electronics, IEEE Journal of* **3**, pp. 1254–1270, oct 1997.
- [14] P. Blixt and U. Ohlander, “19 ps switching of a bistable laser diode with 30 fj optical pulses,” *Photonics Technology Letters, IEEE* **2**, pp. 175–177, mar 1990.

- [15] M. Takenaka, K. Takeda, Y. Kanema, M. Raburn, T. Miyahara, H. Uetsuka, and Y. Nakano, “MMI-BLD optical flip-flop for all-optical packet switching,” in *Photonics in Switching, 2007*, pp. 13 –14, 19-22 2007.
- [16] K. Takeda, M. Takenaka, T. Tanemura, and Y. Nakano, “All-optical flip-flop based on mach-zehnder interferometer bistable laser diode,” in *Optical Communication, 2009. ECOC '09. 35th European Conference on*, pp. 1 –2, 20-24 2009.
- [17] T. Mori, Y. Yamayoshi, and H. Kawaguchi, “Low-switching-energy and high-repetition-frequency all-optical flip-flop operations of a polarization bistable vertical-cavity surface-emitting laser,” *Applied Physics Letters* **88**(10), p. 101102, 2006.
- [18] H. Kawaguchi, “All-optical signal processing using polarization bistable VCSELs,” in *Transparent Optical Networks, 2005, Proceedings of 2005 7th International Conference*, **2**, pp. 87 – 90 Vol. 2, 3-7 2005.
- [19] T. Katayama, T. Ooi, and H. Kawaguchi, “4-bit all-optical buffer memory with shift register function using polarization bistable VCSELs,” in *Optical Fiber Communication - includes post deadline papers, 2009. OFC 2009. Conference on*, pp. 1 –3, 22-26 2009.
- [20] M. Sorel, G. Giuliani, A. Scire, R. Miglierina, S. Donati, and P. Laybourn, “Operating regimes of GaAs-AlGaAs semiconductor ring lasers: experiment and model,” *IEEE Journal of Quantum Electronics* **39**, pp. 1187 – 1195, oct. 2003.
- [21] M. T. Hill, H. J. S. Dorren, T. de Vries, X. J. M. Leijtens, J. H. den Besten, B. Smalbrugge, Y.-S. Oei, H. Binsma, G.-D. Khoe, and M. K. Smit, “A fast low-power optical memory based on coupled micro-ring lasers,” *Nature* **432**, pp. 206–209, Nov 2004.
- [22] L. Liu, R. Kumar, K. Huybrechts, T. Spuesens, G. Roelkens, E.-J. Geluk, T. de Vries, P. Regreny, D. Van Thourhout, R. Baets, and G. Morthier, “An ultra-small, low-power, all-optical flip-flop memory on a silicon chip,” *Nature Photonics* **4**, pp. 182–187, Mar 2010.

- [23] D. R. Scifres, R. D. Burnham, and W. Streifer, “Grating-coupled GaAs single heterostructure ring laser,” *Applied Physics Letters* **28**(11), pp. 681–683, 1976.
- [24] N. Matsumoto and K. Kumabe, “AlGaAs-GaAs semiconductor ring laser,” *Japanese Journal of Applied Physics* **16**(8), pp. 1395–1398, 1977.
- [25] T. Krauss, P. J. R. Laybourn, and J. Roberts, “Cw operation of semiconductor ring lasers,” *Electron. Lett.* **26**, pp. 2095–2097, jun 1990.
- [26] J. P. Hohimer and G. A. Vawter, “Unidirectional semiconductor ring lasers with racetrack cavities,” *Applied Physics Letters* **63**(18), pp. 2457–2459, 1993.
- [27] G. Griffel, J. Abeles, R. Menna, A. Braun, J. Connolly, and M. King, “Low-threshold InGaAsP ring lasers fabricated using bi-level dry etching,” *IEEE Photon. Tech. Lett.* **12**, pp. 146–148, feb 2000.
- [28] C. Ji, M. Leary, and J. Ballantyne, “Long-wavelength triangular ring laser,” *IEEE Photon. Tech. Lett.* **9**, pp. 1469–1471, nov. 1997.
- [29] T. Cockerill, D. Forbes, J. Dantzig, and J. Coleman, “Strained-layer InGaAs-GaAs-AlGaAs buried-heterostructure quantum-well lasers by three-step selective-area metalorganic chemical vapor deposition,” *IEEE Journal of Quantum Electronics* **30**, pp. 441–445, feb 1994.
- [30] J. P. Hohimer, D. C. Craft, G. R. Hadley, G. A. Vawter, and M. E. Warren, “Single-frequency continuous-wave operation of ring resonator diode lasers,” *Applied Physics Letters* **59**, pp. 3360–3362, dec 1991.
- [31] J. P. Hohimer, G. A. Vawter, D. C. Craft, and G. R. Hadley, “Interferometric ring diode lasers,” *Applied Physics Letters* **61**(12), pp. 1375–1377, 1992.
- [32] J. P. Hohimer, G. R. Hadley, and G. A. Vawter, “Semiconductor ring lasers with reflection output couplers,” *Applied Physics Letters* **63**(3), pp. 278–280, 1993.
- [33] J. P. Hohimer, G. A. Vawter, D. C. Craft, and G. R. Hadley, “Improving the performance of semiconductor ring lasers by controlled reflection feedback,” *Applied Physics Letters* **61**(9), pp. 1013–1015, 1992.

- [34] J. P. Hohimer and G. A. Vawter, "Passive mode locking of monolithic semiconductor ring lasers at 86 GHz," *Applied Physics Letters* **63**(12), pp. 1598–1600, 1993.
- [35] G. Vawter, A. Mar, V. Hietala, J. Zolper, and J. Hohimer, "All optical millimeter-wave electrical signal generation using an integrated mode-locked semiconductor ring laser and photodiode," *IEEE Photon. Tech. Lett.* **9**, pp. 1634–1636, dec 1997.
- [36] J. J. Liang, S. T. Lau, M. H. Leary, and J. M. Ballantyne, "Unidirectional operation of waveguide diode ring lasers," *Applied Physics Letters* **70**(10), pp. 1192–1194, 1997.
- [37] A. Behfar-Rad, J. M. Ballantyne, and S. S. Wong, "Etched-facet AlGaAs triangular-shaped ring lasers with output coupling," *Applied Physics Letters* **59**(12), pp. 1395–1397, 1991.
- [38] A. Behfar-Rad, J. M. Ballantyne, and S. S. Wong, "AlGaAs/GaAs-based triangular-shaped ring ridge lasers," *Applied Physics Letters* **60**(14), pp. 1658–1660, 1992.
- [39] R. Bussjager, R. Erdmann, V. Kovanis, B. McKeon, S. Johns, A. Morrow, M. Green, N. Stoffel, S. Tan, C. Shick, W. Bacon, and B. Beaman, "Packaged diamond-shaped ring-laser-diode switch," in *Avionics Fiber-Optics and Photonics, 2006. IEEE Conference*, pp. 64–65, 12-14 2006.
- [40] E. Bente, Y. Barbarin, J. den Besten, M. Smit, and J. Binsma, "Wavelength selection in an integrated multiwavelength ring laser," *IEEE Journal of Quantum Electronics* **40**, pp. 1208–1216, sept. 2004.
- [41] J. den Besten, R. Broeke, M. van Geemert, J. Binsma, F. Heinrichsdorff, T. van Dongen, T. de Vries, E. Bente, X. Leijtens, and M. Smit, "A compact digitally tunable seven-channel ring laser," *IEEE Photon. Tech. Lett.* **14**, pp. 753–755, jun 2002.
- [42] Y. Barbarin, E. Bente, M. Heck, J. den Besten, G. Guidi, Y. Oei, J. Binsma, and M. Smit, "Realization and modeling of a 27-GHz integrated passively

- mode-locked ring laser,” *Photonics Technology Letters, IEEE* **17**, pp. 2277 – 2279, nov. 2005.
- [43] M. Heck, M. Tahvili, S. Anantathanasarn, M. Smit, R. Notzel, and E. Bente, “Observation of dynamics in a 5 GHz passively mode-locked InAs/InP (100) quantum dot ring laser at 1.55  $\mu\text{m}$ ,” in *Lasers and Electro-Optics 2009 and the European Quantum Electronics Conference. CLEO Europe - EQEC 2009. European Conference on*, pp. 1 –1, 14-19 2009.
- [44] T. Krauss and P. Laybourn, “Very low threshold current operation of semiconductor ring lasers,” *Optoelectronics, IEE Proceedings J* **139**, pp. 383 –388, dec 1992.
- [45] T. Krauss, P. Laybourn, and R. DeLaRue, “Improved performance of semiconductor ring lasers with multi-mode interference output couplers,” in *Semiconductor Laser Conference, 1994., 14th IEEE International*, pp. 87 –88, 19-23 1994.
- [46] T. Krauss, R. M. DeLaRue, I. Gontijo, P. J. R. Laybourn, and J. S. Roberts, “Strip-loaded semiconductor ring lasers employing multimode interference output couplers,” *Applied Physics Letters* **64**(21), pp. 2788–2790, 1994.
- [47] T. Krauss, R. DeLaRue, P. Laybourn, B. Vogeles, and C. Stanley, “Efficient semiconductor ring lasers made by a simple self-aligned fabrication process,” *IEEE Journal of Quantum Electronics* **1**, pp. 757 –761, jun 1995.
- [48] S. Yu, T. Krauss, and P. Laybourn, “Multiple output semiconductor ring lasers with high external quantum efficiency,” *Optoelectronics, IEE Proceedings -* **144**, pp. 19 –22, feb 1997.
- [49] S. Yu, T. F. Krauss, and P. J. R. Laybourn, “Mode locking in large monolithic semiconductor ring lasers,” *Optical Engineering* **37**(4), pp. 1164–1168, 1998.
- [50] M. Sorel and P. Laybourn, “Control of unidirectional operation in semiconductor ring lasers,” in *Lasers and Electro-Optics Society, 2001. LEOS 2001. The 14th Annual Meeting of the IEEE*, **2**, pp. 513 –514 vol.2, 2001.

- [51] M. Sorel, P. J. R. Laybourn, G. Giuliani, and S. Donati, “Unidirectional bistability in semiconductor waveguide ring lasers,” *Applied Physics Letters* **80**(17), pp. 3051–3053, 2002.
- [52] S. Fürst, *Monolithic Integration of Semiconductor Ring Lasers*. PhD thesis, University of Glasgow, July 2008.
- [53] S. Furst, S. Yu, and M. Sorel, “Fast and digitally wavelength-tunable semiconductor ring laser using a monolithically integrated distributed bragg reflector,” *IEEE Photon. Tech. Lett.* **20**, pp. 1926–1928, dec.1, 2008.
- [54] S. McMaster, *Monolithically Integrated Mode-Locked Ring Lasers and Mach-Zehnder Interferometers in AlGaInAs*. PhD thesis, University of Glasgow, June 2010.
- [55] M. Gnan, S. Thoms, D. Macintyre, R. M. De La Rue, and M. Sorel, “Fabrication of low-loss photonic wires in silicon-on-insulator using hydrogen silsesquioxane electron-beam resist,” *Electron. Lett.* **44**(2), pp. 115–116, January 17 2008.
- [56] T. H. P. Chang, “Proximity effect in electron-beam lithography,” *J. Vac. Sci. Technol. B* **12**(6), pp. 1271–1275, 1975.
- [57] L. I. Aparshina, S. V. Dubonos, S.V.Maksimov, A.A.Svintsov, and S.I.Zaitsev, “Energy dependence of proximity parameters investigated by fitting before measurement tests,” *J. Vac. Sci. Technol. B* **12**(6), pp. 2298–2302, 1997.
- [58] G. T. Edwards, A. Sobiesierski, D. I. Westwood, and P. M. Snowton, “Fabrication of high-aspect-ratio, sub-micron gratings in AlGaInP/GaAs laser structures using a BCl<sub>3</sub>/Cl<sub>2</sub>/Ar inductively coupled plasma,” *Semiconductor Science and Technology* **22**(9), p. 1010, 2007.
- [59] L. Chee-Wei and C. Mee-Koy, “Room-temperature inductively coupled plasma etching of inp using Cl<sub>2</sub>/N<sub>2</sub> and Cl<sub>2</sub>/CH<sub>4</sub>/H<sub>2</sub>,” *Chinese Physics Letters* **23**(4), p. 903, 2006.

- [60] K. Kennedy, K. M. Groom, and R. A. Hogg, "Fabrication of v-groove gratings in InP by inductively coupled plasma etching with SiCl<sub>4</sub>/Ar," *Semiconductor Science and Technology* **21**(1), p. L1, 2006.
- [61] P. Strasser, R. Wuest, F. Robin, K. Rauscher, B. Wild, D. Erni, and H. Jackel, "An ICP-RIE etching process for InP-based photonic crystals using Cl<sub>2</sub>/Ar/N<sub>2</sub> chemistry," pp. 242–245, May 2005.
- [62] R. Grover, J. V. Hryniewicz, O. S. King, and V. Van, "Process development of methane–hydrogen–argon-based deep dry etching of inp for high aspect-ratio structures with vertical facet-quality sidewalls," *J. Vac. Sci. Technol. B* **19**(5), pp. 1694–1698, 2001.
- [63] K. Shinoda, K. Nakahara, and H. Uchiyama, "InGaAlAs/InP ridge-waveguide lasers fabricated by highly selective dry etching in CH<sub>2</sub>/H<sub>2</sub>/O<sub>2</sub> plasma," pp. 550–553, May 2003.
- [64] M. Sternheim, W. van Gelder, and A. W. Hartman, "A laser interferometer system to monitor dry etching of patterned silicon," *Journal of The Electrochemical Society* **130**(3), pp. 655–658, 1983.
- [65] P. Collot, T. Diallo, and J. Canteloup, "Dry-etch monitoring of III–V heterostructures using laser reflectometry and optical emission spectroscopy," *J. Vac. Sci. Technol. B* **9**(5), pp. 2497–2502, 1991.
- [66] R. Dylewitz, R. M. D. L. Rue, R. Wasielewski, P. Mazur, G. Mezósi, and A. C. Bryce, "Fabrication of submicron-sized features in InP/InGaAsP/AlGaInAs quantum well heterostructures by optimized inductively coupled plasma etching with Cl<sub>2</sub>/Ar/N<sub>2</sub> chemistry," *J. Vac. Sci. Technol. B*, 2010. accepted for publication.
- [67] G. Edwards, P. Smowton, and D. Westwood, "Dry etching of anisotropic microstructures for distributed bragg reflectors in AlGaInP/GaAs laser structures," *Selected Topics in Quantum Electronics, IEEE Journal of* **14**, pp. 1098–1103, July-aug. 2008.

- [68] V. Rideout, “A review of the theory and technology for ohmic contacts to group III-V compound semiconductors,” *Solid-State Electronics* **18**(6), pp. 541 – 550, 1975.
- [69] T. Higashi, S. Sweeney, A. Phillips, A. Adams, E. O’Reilly, T. Uchida, and T. Fujii, “Observation of reduced nonradiative current in 1.3  $\mu\text{m}$  AlGaInAs-InP strained MQW lasers,” *IEEE Photon. Tech. Lett.* **11**, pp. 409–411, Apr 1999.
- [70] Y.-K. Kuo, S.-H. Yen, M.-W. Yao, M.-L. Chen, and B.-T. Liou, “Numerical study on gain and optical properties of AlGaInAs, InGaAs, and InGaAsP material systems for 1.3  $\mu\text{m}$  semiconductor lasers,” *Optics Communications* **275**(1), pp. 156 – 164, 2007.
- [71] M. Camargo Silva, J. Sih, T. Chou, J. Kirk, G. Evans, and J. Butler, “1.3  $\mu\text{m}$  strained MQW AlGaInAs and InGaAsP ridge-waveguide lasers—a comparative study,” in *Microwave and Optoelectronics Conference, 1999. SBMO/IEEE MTT-S, APS and LEOS - IMOC '99. International*, **1**, pp. 10–12 vol. 1, 1999.
- [72] L. A. Coldren and S. W. Corzine, *Diode Lasers and Photonic Integrated Circuits*. Wiley-Interscience.
- [73] W. A. McIlroy, P. A. Kurobe, and Y. Uematsu, “Analysis and application of theoretical gain curves to the design of multi-quantum-well lasers,” *IEEE Journal of Quantum Electronics* **21**, pp. 1958 – 1963, Dec 1985.
- [74] A. Kurobe, H. Furuyama, S. Naritsuka, N. Sugiyama, Y. Kokubun, and M. Nakamura, “Effects of well number, cavity length, and facet reflectivity on the reduction of threshold current of GaAs/AlGaAs multi-quantum well lasers,” *IEEE Journal of Quantum Electronics* **24**, pp. 635 – 640, Apr 1988.
- [75] S. Fürst, A. Pérez-Serrano, A. Scirè, M. Sorel, and S. Balle, “Modal structure, directional and wavelength jumps of integrated semiconductor ring lasers: Experiment and theory,” *Applied Physics Letters* **93**(25), p. 251109, 2008.
- [76] “A study of electrically active defects created in p-InP by  $\text{CH}_4/\text{H}_2$  reactive ion etching,” *Journal of Applied Physics* **82**(4), p. 1696, 1997.

- [77] B. E. A. Saleh and M. C. Teich, *Fundamentals of Photonics*. Wiley-Interscience, 2<sup>nd</sup> ed., 2007.
- [78] L. Soldano and E. Pennings, “Optical multi-mode interference devices based on self-imaging: principles and applications,” *Journal of Lightwave Technology* **13**(4), pp. 615 –627, 1995.
- [79] H.-B. Lin, R.-S. Cheng, and W.-S. Wang, “Wide-angle low-loss single-mode symmetric y-junctions,” *IEEE Photon. Tech. Lett.* **6**, pp. 825 –827, jul 1994.
- [80] K. Ogusu, “Transmission characteristics of single-mode asymmetric dielectric waveguide y-junctions,” *Optics Communications* **53**(3), pp. 169 – 172, 1985.
- [81] M. Rajarajan, B. M. A. Rahman, and K. T. V. Grattan, “A rigorous comparison of the performance of directional couplers with multimode interference devices,” *Journal of Lightwave Technology* **17**(2), p. 243, 1999.
- [82] R. Hanfoug, L. Augustin, Y. Barbarin, J. van der Tol, E. Bente, F. Karouta, D. Rogers, S. Cole, Y. Oei, X. Leijtens, and M. Smit, “Reduced reflections from multimode interference couplers,” *Electron. Lett.* **42**, pp. 465 – 466, april 2006.
- [83] J. C. Campbell, F. A. Blum, D. W. Shaw, and K. L. Lawley, “GaAs electro-optic directional-coupler switch,” *Applied Physics Letters* **27**(4), pp. 202–205, 1975.
- [84] D. Marcuse, “Reflection loss of laser mode from tilted end mirror,” *Journal of Lightwave Technology* **7**, pp. 336 –339, feb 1989.
- [85] I. Kaminow, G. Eisenstein, and L. Stulz, “Measurement of the modal reflectivity of an antireflection coating on a superluminescent diode,” *IEEE Journal of Quantum Electronics* **19**, pp. 493 – 495, apr 1983.
- [86] B. Jaskorzynska, J. Nilsson, and L. ThyIén, “Modal reflectivity of uptapered, tilted-facet, and antireflection-coated diode-laser amplifiers,” *J. Opt. Soc. Am. B* **8**(2), pp. 484–493, 1991.
- [87] M. Sargent, “Theory of a multimode quasiequilibrium semiconductor laser,” *Phys. Rev. A* **48**, pp. 717–726, Jul 1993.

- [88] J. Javaloyes and S. Balle, “Emission directionality of semiconductor ring lasers: A traveling-wave description,” *IEEE Journal of Quantum Electronics* **45**, pp. 431–438, may 2009.
- [89] R. Deri and E. Kapon, “Low-loss III-V semiconductor optical waveguides,” *IEEE Journal of Quantum Electronics* **27**, pp. 626–640, mar 1991.
- [90] T. Krauss and P. Laybourn, “Very low threshold current operation of semiconductor ring lasers,” *Optoelectronics, IEE Proceedings J* **139**, pp. 383–388, dec 1992.
- [91] V. N. Bessolov, E. V. Konenkova, and M. V. Lebedev, “A comparison of the effectiveness of GaAs surface passivation with sodium and ammonium sulfide solutions,” *Physics of the Solid State* **39**, pp. 54–57, 1997.
- [92] D. Englund, H. Altug, and J. Vučković, “Low-threshold surface-passivated photonic crystal nanocavity laser,” *Applied Physics Letters* **91**(7), p. 071124, 2007.
- [93] T. K. Oh, C. H. Baek, and B. K. Kang, “Surface treatment for enhancing current gain of AlGaAs/GaAs heterojunction bipolar transistor,” *Solid-State Electronics* **48**(9), pp. 1549–1553, 2004. Non Volatile Memories with discrete storage nodes.
- [94] X. Jinan, H. O. Beom, G. L. Seung, and H. L. El, “1.55  $\mu\text{m}$  InGaAs/InGaAlAs MQW vertical-cavity surface-emitting lasers with InGaAlAs/InP distributed bragg reflectors,” *Optics & Laser Technology* **37**(2), pp. 125–130, 2005.
- [95] S. Adachi, *Physical Properties of III-V Semiconductor Compounds*. Wiley-Interscience, 1992.
- [96] D. Levy, R. Scarmozzino, Y. Li, and J. Osgood, R.M., “A new design for ultracompact multimode interference-based  $2 \times 2$  couplers,” *IEEE Photon. Tech. Lett.* **10**, pp. 96–98, jan 1998.
- [97] D. Levy, K. H. Park, R. Scarmozzino, J. Osgood, R.M., C. Dries, P. Studenkov, and S. Forrest, “Fabrication of ultracompact 3-dB  $2 \times 2$  MMI power splitters,” *IEEE Photon. Tech. Lett.* **11**, pp. 1009–1011, aug 1999.

- [98] S. Y. Lee, S. Darmawan, C.-W. Lee, and M.-K. Chin, “Transformation between directional couplers and multi-mode interferometers based on ridge waveguides,” *Optics Express* **12**(14), pp. 3079–3085, 2004.
- [99] J. Wang, W. Yuan, C. S. Seibert, and D. C. Hall, “Loss characterization of high-index-contrast ridge waveguide oxide-confined InGaAs quantum well racetrack ring-resonator lasers,” *Novel In-Plane Semiconductor Lasers VIII* **7230**(1), p. 72300J, 2009.
- [100] F. Ladouceur and E. Labeye, “A new general approach to optical waveguide path design,” *Journal of Lightwave Technology* **13**, pp. 481–492, mar 1995.
- [101] Y. Berlatzky, I. Shtrichman, R. Narevich, E. Narevicius, G. Rosenblum, and I. Vorobeichik, “Controlling coupling of guided to radiating modes using adiabatic transitions between waveguides of different curvature,” **23**(3), p. 1278, 2005.
- [102] M. Heinbach, M. Schienle, A. Schmid, B. Acklin, and G. Muller, “Low-loss bent connections for optical switches,” **15**, pp. 833–837, may 1997.
- [103] A. Kumar and S. Aditya, “Performance of s-bends for integrated-optic waveguides,” *Microwave and Optical Technology Letters* **19**(4), pp. 289–292, 1998.
- [104] J. Boucart, C. Starck, F. Gaborit, A. Plais, N. Bouche, E. Derouin, J. Remy, J. Bonnet-Gamard, L. Goldstein, C. Fortin, D. Carpentier, P. Salet, F. Brillouet, and J. Jacquet, “Metamorphic DBR and tunnel-junction injection. A CW RT monolithic long-wavelength VCSEL,” *Selected Topics in Quantum Electronics, IEEE Journal of* **5**, pp. 520–529, may/jun 1999.
- [105] J. V. Campenhout, P. R. Romeo, P. Regreny, C. Seassal, D. V. Thourhout, S. Verstuyft, L. D. Cioccio, J.-M. Fedeli, C. Lagahe, and R. Baets, “Electrically pumped InP-based microdisk lasers integrated with a nanophotonic silicon-on-insulator waveguide circuit,” *Optics Express* **15**(11), pp. 6744–6749, 2007.
- [106] K. Petermann, *Laser Diode Modulation and Noise*. Springer, 1991.

- [107] L. Zhang, I. Kang, A. Bhardwaj, N. Sauer, S. Cabot, J. Jaques, and D. Neilson, “Reduced recovery time semiconductor optical amplifier using p-type-doped multiple quantum wells,” **18**, pp. 2323 –2325, nov.15, 2006.
- [108] E. L. Delpon, J. L. Oudar, N. Bouché, R. Raj, A. Shen, N. Stelmakh, and J. M. Lourtioz, “Ultrafast excitonic saturable absorption in ion-implanted InGaAs/InAlAs multiple quantum wells,” *Applied Physics Letters* **72**(7), pp. 759–761, 1998.
- [109] F. Mogensen, H. Olesen, and G. Jacobsen, “Locking conditions and stability properties for a semiconductor laser with external light injection,” *IEEE Journal of Quantum Electronics* **21**, pp. 784 – 793, jul 1985.
- [110] B. Li, M. Memon, G. Mezosi, G. Yuan, Z. Wang, M. Sorel, and S. Yu, “All-optical response of semiconductor ring laser to dual-optical injections,” *IEEE Photon. Tech. Lett.* **20**, pp. 770 –772, may15, 2008.
- [111] B. Li, D. Lu, M. Memon, G. Mezosi, Z. Wang, M. Sorel, and S. Yu, “All-optical digital logic and and xor gates using four-wave-mixing in monolithically integrated semiconductor ring lasers,” *Electron. Lett.* **45**, pp. 698 –700, june 2009.
- [112] B. Li, M. Memon, G. Mezosi, Z. Wang, M. Sorel, and S. Yu, “All-optical digital logic xor gate using bistable semiconductor ring lasers,” in *Lasers and Electro-Optics 2009 and the European Quantum Electronics Conference. CLEO Europe - EQEC 2009. European Conference on*, pp. 1 –1, 14-19 2009.
- [113] B. Li, M. Memon, G. Mezosi, Z. Wang, M. Sorel, and S. Yu, “Characterization of all-optical regeneration potentials of a bistable semiconductor ring laser,” *Journal of Lightwave Technology* **27**, pp. 4233 –4240, oct.1, 2009.
- [114] K. Thakulsukanant, B. Li, I. Memon, G. Mezosi, Z. Wang, M. Sorel, and S. Yu, “All-optical label swapping using bistable semiconductor ring laser in an optical switching node,” *Journal of Lightwave Technology* **27**, pp. 631 –638, march15, 2009.
- [115] R. J. Manning and D. A. O. Davies, “Three-wavelength device for all-optical signal processing,” *Optics Letters* **19**(12), pp. 889–991, 1994.

- [116] M. Dupertuis, J. Pleumeekers, T. Hessler, P. Selbmann, B. Deveaud, B. Dagens, and J. Emery, “Extremely fast high-gain and low-current SOA by optical speed-up at transparency,” *IEEE Photon. Tech. Lett.* **12**, pp. 1453 – 1455, nov 2000.
- [117] S. Furst and M. Sorel, “Cavity-enhanced four-wave mixing in semiconductor ring lasers,” *IEEE Photon. Tech. Lett.* **20**(5), pp. 366 –368, 2008.